

NONLINEAR, PARAMETRIC, AND COUPLED

NANOELECTROMECHANICAL SYSTEMS

Thesis by

Rassul Karabalin

In Partial Fulfillment of the Requirements for the Degree of

Doctor of Philosophy

CALIFORNIA INSTITUTE OF TECHNOLOGY

Pasadena, California

2008

(Defended April 2, 2008)

© 2008

Rassul Karabalin

All Rights Reserved

ACKNOWLEDGEMENTS

To begin with I would like to thank my academic advisor Michael Roukes for the always reliable support I enjoyed throughout long years spent in the lab. I greatly appreciate a good balance of freedom to apply my own creativity and the amount of wise advice that provided a visionary direction.

I am immensely grateful to my esteemed collaborators Philip Feng and Sotiris Masmanidis who spent vast amount of their valuable time training me on various pieces of equipment, teaching me how to stop fearing to be a scientist and educating me how to come up with, plan, perform, and report to the boss very interesting experiments we were doing. I also thank all the present and past members of the Roukes group including Matt Matheny, Jie Xiang, Inna Kozinsky, Sequoyah Aldridge, Edward Myers, Ben Gudlewski, Mo Li, Akshay Naik, Jessica Arlett, Igor Bargatin, Matt LaHaye, Selim Hanay, Wonhee Lee, Junho Suh, James Maloney, Blake Axelrod, and many others. I hugely benefited from everyday interactions with all the members and visitors in the group. I was fortunate to receive great help from Nils Asplund and Steve Stryker whenever I needed something extremely complicated in my experiments.

I would like to extend my sincere appreciation to my thesis committee: Professors Marc Bockrath, Mike Cross, and Ali Hajimiri. My thanks also go to Professors Hideo Mabuchi, from Caltech, and Professor Ron Lifshitz from Tel Aviv University for being on my candidacy committee and offering insightful comments and helpful suggestions. I especially thank Ron and Mike for providing outstanding help with theoretical calculation and giving suggestions about most of my experiments. Many thanks to Iwijn De Vlaminck and Gustaaf Borghs from IMEC for providing a large number of high-quality GaAs heterostructures that spawned the D-NEMS project. I am grateful to Mark Freeman who helped us introduce optical interferometric detection technique in the group.

for Dr. K.

ABSTRACT

Advances in nanoscience and nanotechnology hold enormous promises to benefit humankind in basic research, industry, and everyday life. One particular class of the vast field of nanodevices is resonant *nanoelectromechanical systems* (NEMS), which have recently attracted considerable research interest. While many of obstacles have been overcome in fundamental physics and engineering research of NEMS, intriguing questions and technological challenges remain unmet. This thesis is primarily focused on the studies of parametric, nonlinear, and coupled NEMS resonators.

In this work the first very high-frequency (VHF) nanomechanical degenerate parametric amplifiers have been demonstrated by employing both magnetomotive and piezoelectric parametric pumping. A mechanical gain of 1000 and quality factor enhancement of 75 have been achieved. Such parametric resonators and nanomechanical amplification make it possible to evade the often-dominant transducer and amplifier noise, thus offering possibilities for improving the sensitivity of NEMS sensors, for exploring mechanical-domain signal processing, and for noise squeezing in precision physics measurements.

The thesis also focuses on the rich dynamics and physics of coupled NEMS resonators. First, the major mechanisms of coupling are investigated both experimentally and analytically. The formalism for characterizing a new basis of vibration modes for strongly coupled nanoresonators is developed and experimentally demonstrated for systems with two, three and ten NEMS devices. By employing a pair of coupled resonators for long-term drift compensation, considerable improvement in resonator frequency stability is demonstrated. Simple linear interaction in nonlinear nanomechanical resonators is shown to generate remarkably complex and rich behavior including spontaneous state transition and chaos.

Finally, the complexity of the system is further increased when coupled and parametric effects are combined. A novel nanomechanical amplification mechanism has been discovered, based on the dynamical changes that an input signal induces in the topology of a bifurcation diagram of a system of two weakly coupled parametric resonators. Another interesting phenomenon—nondegenerate parametric NEMS amplification is demonstrated in the case of strong coupling. This is a promising route to low noise mechanical displacement sensing because it not only provides a fundamentally noiseless amplification mechanism, but also it decouples pump and signal frequency.

TABLE OF CONTENTS

Acknowledgements	iii
Abstract	v
Table of Contents	vii
List of Figures	ix
List of Tables	xii
Nomenclature	xiii
Chapter 1: Introduction	1
1.1 Introduction and Motivation	1
1.2 Overview	2
Chapter 2: Parametric Effects Theory	4
2.1 Elastic Beam	4
2.2 Parametric Amplification (Mathieu Equation)	6
2.3 Gain and Q Enhancement	8
2.4 Gain-Dynamic Range Tradeoff	11
2.5 Bistability and Parametric Tongue	13
Summary	15
Chapter 3: Lorentz Force VHF Parametric Amplifier	17
3.1 Lorentz Force Parametric Amplifier Design	17
3.2 Measurements Results	20
3.3 Heating Model	25
Summary	34
Chapter 4: D-NEMS Parametric Amplifier	35
4.1 D-NEMS Piezoelectric Frequency Tuning	35
4.2 Parametric Gain and Q Enhancement	41
4.3 Parametric Amplification and Frequency Stability	45
4.4 Parametric Actuation	47
Summary	50
Chapter 5: Coupling Phenomena in D-NEMS	52
5.1 Variety of Coupling Mechanisms in D-NEMS	52
5.2 Strong Coupling Model	55
5.3 Strong Elastic Coupling Through Supports	58
5.4 Frequency Bridge	64
Summary	67
Chapter 6: Coupling Of Two Duffing Resonators	68
6.1 Theoretical Analysis	68
6.2 Coupling Parameters of the System	72
6.3 Nondemolition Measurements and Linearization	77
6.4 Spectral Responses	84
6.5 Mechanical State Instabilities and Chaos	89
Summary	95

Chapter 7: Bifurcation Topology Amplifier	97
7.1 Parametric Actuation of Two Weakly Coupled Resonators.....	97
7.2 Voltage-Dependent Bifurcation Diagram.....	101
7.4 Bifurcation Topology Amplifier Measurements.....	105
7.5 Bifurcation Topology Amplifier Characterization.....	110
Summary.....	114
Chapter 8: Nondegenerate Parametric Effect	115
8.1 Parametric Actuation of Two Strongly Coupled Resonators.....	115
8.2 Nondegenerate Parametric Resonance Measurements.....	119
8.3 Harmonics in Nondegenerate Parametric Resonance.....	124
8.4 Frequency Shifts and Satellites.....	127
Summary.....	132
Chapter 9: Conclusions And Future Directions	133
9.1 Final Thoughts.....	133
Bibliography.....	135

LIST OF FIGURES

<i>Number</i>	<i>Page</i>
Figure 2.1 Doubly clamped beam	4
Figure 2.2 Regular vs parametric amplifier comparison	12
Figure 3.1 SEM and simulation images of Lorentz force PA	18
Figure 3.2 Mode structure of the Lorentz force PA.....	21
Figure 3.3 DC tuning measurements of Lorentz force PA.....	23
Figure 3.4 The setup for Q enhancement measurements	24
Figure 3.5 Quality factor enhancement measurements results.....	25
Figure 3.6 Heating model schematics	26
Figure 3.7 Frequency and Q dependence on temperature	31
Figure 3.8 Threshold voltages for Lorentz force PA implementations.....	33
Figure 4.1 D-NEMS resonator schematics	36
Figure 4.2 Optical interferometric measurement setup	39
Figure 4.3 DC tuning measurement for D-NEMS beams	40
Figure 4.4 Gain and Q enhancement for high-frequency beam	42
Figure 4.5 Gain and Q enhancement in air	44
Figure 4.6 The setup for frequency stability measurements.....	45
Figure 4.7 Frequency stability measurements results.....	46
Figure 4.8 Parametric actuation	48
Figure 4.9 Instability tongue	50
Figure 5.1 SEM image of the mechanical ledges	53
Figure 5.2 The schematics of electrostatic interaction	54
Figure 5.3 SEM and spectrum of two very strongly coupled resonators ...	58
Figure 5.4 Finite element simulation of strongly coupled resonators	59
Figure 5.5 Modal analysis of three strongly coupled resonators.....	60
Figure 5.6 SEM and measurement for three beams.....	61
Figure 5.7 SEM and modal analysis for ten beams	62

Figure 5.8 Spectrum of ten strongly coupled beams	63
Figure 5.9 The setup for frequency bridge measurements	64
Figure 5.10 Frequency bridge result for two strongly coupled beams	65
Figure 5.11 Frequency bridge result for two weakly coupled beams	66
Figure 6.1 SEM image of two strongly coupled isolated beams	73
Figure 6.2 Spectrum of the system with 0° and 180° connections	75
Figure 6.3 Spectrum of the system with left and right connections	76
Figure 6.4 Frequency tuning due to strong nonlinear coupling	79
Figure 6.5 Theoretical plots for linearization parameters	81
Figure 6.6 Theoretical and experimental result for linearization	83
Figure 6.7 Theoretical and experimental result for complex transitions	85
Figure 6.8 Amplitude sweeps prediction and measurement	87
Figure 6.9 Measurement of both modes monitored	88
Figure 6.10 An example of A_{II} versus A_I phase plot	90
Figure 6.11 Spectrum of the amplitude modulated motion	91
Figure 6.12 The setup for Lissajous figures measurements	92
Figure 6.13 Phase trajectories measurement results	94
Figure 6.14 The evidence of chaotic behavior in NEMS	95
Figure 7.1 The theoretical analysis of the bifurcation diagram	100
Figure 7.2 The measurements of the topology of bifurcation	102
Figure 7.3 Nonlinear resonances for the two beams	103
Figure 7.4 Simulation of weak elastic coupling	104
Figure 7.5 BTA measurement setup	106
Figure 7.6 Spectrum analyzer and oscilloscope measurements of BTA ..	110
Figure 7.7 The experimental characterization of BTA	112
Figure 8.1 DC tuning measurement of nondeg PA	117
Figure 8.2 Spectrum of the nondegenerate parametric resonance	122
Figure 8.3 The parametric tongue of the first mode	123
Figure 8.4 The spectrum of harmonics in nondeg parametric resonator ..	125
Figure 8.5 Amplitude dependence during long parametric sweep	126

Figure 8.6 Amplitude and frequency shift measurements.....	128
Figure 8.7 Frequency shifts for other devices.....	130
Figure 8.8 The spectrum of satellite peaks	131

LIST OF TABLES

<i>Number</i>	<i>Page</i>
Table 3.1 Physical parameters of the modes of the Lorentz force PA	22
Table 4.1 Physical parameters of six D-NEMS beams	43
Table 6.1 The parameters of devices used in measurements.....	77
Table 8.1 The parametric threshold for nondegenerate PA.....	120

NOMENCLATURE

III-V	semiconductors that consist of elements from iii and v columns of periodic table
AC	alternating current
AM	amplitude modulation
BA	bifurcation amplifier
BTA	bifurcation topology amplifier
CMOS	complimentary metal oxide semiconductor
CW	continuous wave
DC	direct current
D-NEMS	depletion-mediated nems
ECR	electron coupled resonance
EOM	equation of motion
FM	frequency modulation
FWHM	full width at half maximum
NEMS	nanoelectromechanical systems
RF	radio frequency
PA	parametric amplifier
PLL	phase locked loop
SAW	surface acoustic wave
SEM	scanning electron microscope
VHF	very high frequency

Chapter 1

INTRODUCTION

1.1 INTRODUCTION AND MOTIVATION

Recent developments in the area of nanotechnology hold enormous promise to benefit humankind in basic research, industry and everyday life. In his visionary speech [1] made 50 years ago, Richard Feynman made a suggestion that there is no particular reason why we can't make computers very small. "I don't know how to do this on a small scale in a practical way, but I do know that computing machines are very large; they fill rooms. Why can't we make them very small, make them of little wires, little elements—and by little, I mean little. For instance, the wires should be 10 or 100 atoms in diameter, and the circuits should be a few thousand angstroms across." Indeed today everyone has a laptop, which is capable of performing enormous amount of operations in no time and has the smallest wires just a few hundred atoms wide. This is just a small example of how rapid progress in a field of nanotechnology has made great social and economic impact. Currently the pace of the progress is not slowing down; to the contrary, in many segments it is even accelerating.

One particular class within the vast field of nanodevices called resonant *nanoelectromechanical systems* (NEMS) is just starting to acquire global attention [2]. Their precursors, microelectromechanical systems, have been studied for decades with an increasing interest due to successful growth commercial applications. Nearly all modern projectors use arrays of microscale mechanical mirrors to display the image, inkjet printers use microfluidic chips for printing, and rapid development of optical crossbar switches has caused an explosion in the communication industry. Although reliable commercial NEMS applications are not on the market yet, the interest

of researchers is growing. A remarkable combination of such properties as small mass, high operating frequencies, easily accessible nonlinearity, large quality factor as well as standard semiconductor fabrication techniques hold great promise for providing superior mass [3], force [4] or charge [5] sensors, realizing quantum fock state detection in mechanical systems [6], and integrating mechanical switches with CMOS transistors [7].

A number of obstacles have to be overcome in order to achieve the goal of large-scale utilization of nanoelectromechanical systems. Among the principal challenges are accurate motion transduction, efficient actuation, limiting the dissipation in ambient environments, as well as scalability for integration. This thesis provides possible solutions to all the problems above. When the size of the devices decreases it becomes increasingly difficult to read out the resonator's mechanical motion because existing electromechanical coupling techniques do not provide large enough signal to overcome the noise in electric readout circuits. One possible solution discussed in this thesis is amplification of the signal in the mechanical domain using the idea of parametric oscillations before applying an electrical transducer. A subsequent part of the thesis presents a first step toward large-scale integration by carefully investigating a large variety of physical phenomena in arrays of interacting nanomechanical resonators. The last chapters present a theoretical and experimental study of a number of applications that arise from combining parametric, coupled and nonlinear properties of nanoelectromechanical systems.

1.2 OVERVIEW

The parametric resonance system is an interesting subject of research in many areas ranging from quantum optics [8], to superconducting circuits [9], to plasma physics [10]. A mechanical parametric resonant system was first demonstrated by Rugar and Grutter [11] and since then has

attracted significant attention [12, 13, 14, 15]. The simplest parametric amplification is obtained by periodic modulation of a dynamical parameter of the resonant system, namely the spring constant, at twice its fundamental resonance frequency. For the right phase relationship between the drive and parametric pump, a significant increase in amplitude and effective quality factor can be achieved. The nature of spring constant modulation has usually been capacitive [12, 13], although other methods such as intrinsic residual stress [15] or an external feedback loop [16] have been demonstrated. This thesis presents two interesting alternative schemes, based upon tuning the tensile stress of a nanoresonator using magnetic Lorentz force in chapter 3 and piezoelectric electromechanical coupling in chapter 4.

In addition to enabling practical applications parametric effects introduce an entirely new type of dynamical system. Chapters 5 and 6 discuss the first steps in integrating simple nonlinear resonators and studying their interactions. And chapters 7 and 8 of this thesis present several important effects that are demonstrated using a system of many coupled parametric resonators. These topics will prove crucial for the large-scale integration of nanomechanical resonators.

Chapter 2

PARAMETRIC THEORY

This chapter begins with a basic theoretical background needed to understand the dynamics of nanoelectromechanical resonators. Then a new type of dynamical behavior is introduced by analyzing the simple harmonic resonator with a periodically modulated physical parameter. The parametric resonance that arises is described by special class of partial differential equations called Mathieu equations. Essential concepts and interesting phenomena are then illustrated.

2.1 ELASTIC BEAM

Consider a small rectangular mechanical bar with rigid supports on both sides as shown in figure 2.1. The structure is characterized by its normal modes of vibration. The lowest frequency mode is called the *fundamental mode*. For the particular device shown in figure 2.1 the fundamental resonant mode corresponds to out-of-plane flexural vibration at a frequency of 35 MHz.

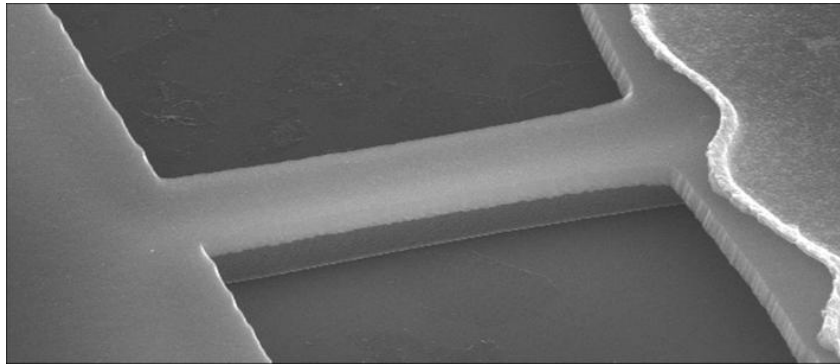


Figure 2.1. Small rectangular structure supported at both ends is designated a doubly clamped beam nanomechanical resonator. The dimensions of this GaAs beam are $4\ \mu\text{m} \times 500\ \text{nm} \times 200\ \text{nm}$ ($L \times w \times t$).

The most convenient way to describe the dynamics of a resonator is to model the behavior of its central point as a one-dimensional simple harmonic oscillator with fundamental frequency ω_0 and quality factor Q corresponding to those of the beam for a particular vibrational mode. Then the simplest equation of motion is given by:

$$m\ddot{x} + \frac{m\omega_0}{Q}\dot{x} + kx = F(t). \quad (2.1)$$

The choice of mass m and stiffness constant k is constrained by the fact that their ratio $k/m=\omega_0^2$ is determined by the measured resonance frequency. Another constraint is a result of the choice of center of the beam as a point of one-dimensional vibration, then elastic constant is given by $k=F_0/x_0$, where F_0 is the total force exerted on the beam by the employed actuation mechanism, and x_0 is a corresponding static displacement of the central point. The mass m is then given by $m=0.735\rho Lwt_h$ [17] for the beam of length L , width w and thickness t_h made out of structural material of Young's modulus Y and density ρ . It is easy to show [18] that the expression for fundamental frequency is given by:

$$\omega_0 = 1.03 \frac{2\pi t_h}{L^2} \sqrt{\frac{Y}{\rho}}, \quad (2.2)$$

where t_h is a geometrical dimension in the direction of vibration. When a sinusoidal drive is applied to the resonator at angular frequency ω the mechanical response assumes a Lorentzian form:

$$x = \frac{F_0 Q}{m\omega_0^2} \frac{\omega_0^2}{Q(\omega_0^2 - \omega^2) + i\omega_0\omega}. \quad (2.3)$$

The first important correction to the simple model just described is the effect caused by the longitudinal tensile stress in the beam. When the amplitude of the beams' motion calculated to the

lowest order rises, the tension in the beams becomes high enough to cause deviations from linearity in the elastic force [19]. The resonator's dynamics can then be approximated by the following equation of motion:

$$m\ddot{x} + \frac{m\omega_0}{Q}\dot{x} + kx + \alpha_D x^3 = F(t), \quad (2.4)$$

where $\alpha_D = 63.6 \frac{Ywt}{L^3}$ is a coefficient of cubic nonlinearity (also known as the *Duffing nonlinearity*). Another important effect is caused by initial tension experienced by the beams arising either from fabrication or applied externally. When the beam is stretched or compressed the resonance frequency shifts up or down respectively [18, 20]:

$$\omega_0 = 1.03 \frac{2\pi t_h}{L^2} \sqrt{\frac{Y}{\rho}} \sqrt{1 + \frac{\sigma L^2}{3.4Yt_h^2}}, \quad (2.5)$$

for tensile stress σ .

2.2 PARAMETRIC AMPLIFICATION (MATHIEU EQUATION)

In order to understand a parametric resonant system, consider a regular elastic beam, whose tensile stress is periodically modulated. The beam is approximated as a one-dimensional resonator, whose spring constant is modulated. The simplest parametric effects are realized when the modulation frequency ω_p is close to twice the fundamental resonance frequency. Then the system dynamics is described by the following equation:

$$m\ddot{x} + \frac{m\omega_0}{Q}\dot{x} + (k + k_p \cos \omega_p t)x + \alpha_D x^3 = F_0 \sin(\omega t + \varphi_D). \quad (2.6)$$

Here $k_p = 0.3k_1 L^2 \sigma / (Yt_h^2)$ is the amplitude of the spring constant modulation for a given stress σ .

In order to solve this equation we will employ secular perturbation theory [14]. We define the following parameters:

$$\gamma = \frac{\omega_0}{Q}, \quad g_D = \frac{F_0}{2m}, \quad h_p = \frac{k_p}{2m} = \frac{k_p \omega_0^2}{2k}. \quad (2.7)$$

We now rewrite the equation of motion (2.5) in a simplified form, that, at first pass, ignores the Duffing nonlinearity. Later in this chapter we will describe in greater detail the consequences of having nonlinear terms. The rescaled equation becomes:

$$\ddot{x} + \gamma \dot{x} + (\omega_0^2 + 2h_p \cos \omega_p t)x = 2g_D \sin(\omega t + \varphi_D). \quad (2.8)$$

This expression is known as the Mathieu equation [21]. We solve (2.8) employing secular perturbation theory [14]. After introducing a small dimensionless parameter $\varepsilon \ll 1$ we rewrite the previously defined parameters in the above equation by considering their different scales:

$$h_p = \varepsilon h, \quad g_D = \varepsilon^{3/2} g, \quad \gamma = \varepsilon \Gamma, \quad \omega_p = 2\omega_0 + \varepsilon \Omega_p, \quad \omega = \omega_0 + \varepsilon \Omega, \quad (2.9)$$

where h , g , Γ , Ω_p and Ω are not necessarily small dimensional parameters. Introduction of slower time scale $T = \varepsilon t$ allows us search for the solution to the above Mathieu equation (2.8) in the form:

$$x(t) = \varepsilon^{1/2} (A(T)e^{i\omega_0 t} + c.c.) + \varepsilon^{3/2} x^{(1)}(t) + \dots \quad (2.10)$$

where the vibration at the resonance frequency is modulated by the function $A(T)$, that evolves on a slower timescale. The correction to the solution $x^{(1)}$ is introduced with a higher power of small parameter ε . Complex conjugate terms are abbreviated as “c.c.”

Time derivatives are given as follows,

$$\begin{aligned} \dot{x}(t) &= \varepsilon^{1/2} (\varepsilon A'(T) + i\omega_0 A'(T) + c.c.)e^{i\omega_0 t} + \varepsilon^{3/2} \dot{x}^{(1)}(t) + \dots, \\ \ddot{x}(t) &= \varepsilon^{1/2} (-\omega_0^2 A(T) + 2i\omega_0 \varepsilon A'(T) + \varepsilon^2 A''(T) + c.c.)e^{i\omega_0 t} + \varepsilon^{3/2} \ddot{x}^{(1)}(t) + \dots, \end{aligned} \quad (2.11)$$

where A' and A'' are the slower timescale derivatives. After substituting this expression into equation of motion (2.7) we obtain:

$$\begin{aligned} & \frac{1}{\varepsilon^2} (-\omega_0^2 A(T) + 2i\omega_0 \varepsilon A'(T) + \varepsilon^2 A''(T)) e^{i\omega_0 t} + \frac{3}{\varepsilon^2} \Gamma (\varepsilon A'(T) + i\omega_0 A'(T)) e^{i\omega_0 t} \\ & + \frac{3}{\varepsilon^2} \ddot{x}^{(1)}(t) + c.c. + \dots + (\omega_0^2 + 2\varepsilon h \cos(\omega_p t)) (\frac{1}{\varepsilon^2} A(T) e^{i\omega_0 t} + \frac{3}{\varepsilon^2} x^{(1)}(t) + c.c. + \dots) \quad (2.12) \\ & = 2\varepsilon^{\frac{3}{2}} g \sin(\omega_D t + \phi_D), \end{aligned}$$

In this equation the $O(\varepsilon^{1/2})$ terms cancel as they are the linear mode terms. Therefore by keeping $O(\varepsilon^{3/2})$ terms we extract equation for the correction $x^{(1)}(t)$.

$$\ddot{x}^{(1)}(t) + \omega_0^2 x^{(1)}(t) = (-2i\omega_0 A' - i\Gamma \omega_0 A - hA^* e^{i\Omega_p T} - ig e^{i\Omega_D T}) e^{i\omega_0 t} + (\dots) e^{3i\omega_0 t} + c.c. + \dots, \quad (2.13)$$

On the left-hand side there is a resonator equation with zero damping, thus the term in brackets on the right-hand side should vanish so that the solution for $x^{(1)}(t)$ is finite.

$$2i\omega_0 A' + i\Gamma \omega_0 A + hA^* e^{i\Omega_p T} = -ig e^{i\Omega_D T}, \quad (2.14)$$

2.3 GAIN AND Q ENHANCEMENT

The parametric modulation of a spring constant of a nanoresonator described above can provide significant amplification of mechanical vibration. The parametric gain is defined as the ratio of mechanical amplitude when the beam is pumped to the amplitude when the pump is turned off.

In order to calculate the parametric gain on resonance we assume $\omega = \omega_0$ and $\omega_p = 2\omega_0$. We write down the equation for steady-state time-invariant A and its complex conjugate A^* based on equation (2.14).

$$\begin{aligned} \omega_0 \Gamma A - ihA^* &= -g, \\ ihA + \omega_0 \Gamma A^* &= -g^*. \end{aligned} \quad (2.15)$$

The solution to this regular linear equation is:

$$A = -|g| e^{-i\frac{\pi}{4}} \left[\frac{\cos(\varphi_D + \pi/4)}{\omega_0\Gamma + h} + i \frac{\sin(\varphi_D + \pi/4)}{\omega_0\Gamma - h} \right]. \quad (2.16)$$

When the pump is turned off the equation describes a simple driven resonator with known amplitude on resonance:

$$A_{pump\ off} = \frac{-|g| e^{-i\phi_D}}{i\omega_0\Gamma}. \quad (2.17)$$

Therefore the mechanical amplitude gain due to parametric modulation is given by:

$$G = \frac{A_{pump\ on}}{A_{pump\ off}} = e^{-i(\frac{\pi}{4} - \phi_E)} \left[\frac{\cos(\varphi_D + \pi/4)}{1 + h/\omega_0\Gamma} + i \frac{\sin(\varphi_D + \pi/4)}{1 - h/\omega_0\Gamma} \right] \quad (2.18)$$

The second term in the brackets diverges when the pumping approaches a threshold value $h \rightarrow \omega_0\Gamma$, which physically means that the mechanical signal is amplified due to parametric pumping. Above this threshold the beam breaks into spontaneous oscillations. The greatest enhancement is obtained when there is $\pi/4$ difference in phase between the drive and the pump, while at $-\pi/4$ the amplitude is attenuated.

Rescaling these results to experimental physical quantities we define the stiffness constant at threshold as $k_t = 2k/Q$. The rewritten equation (2.18) for the parametric gain then assumes the form:

$$G = \frac{A_{pump\ on}}{A_{pump\ off}} = \left[\frac{\cos^2(\varphi_D + \pi/4)}{(1 + k_p/k_t)^2} + \frac{\sin^2(\varphi_D + \pi/4)}{(1 - k_p/k_t)^2} \right]^{\frac{1}{2}}. \quad (2.19)$$

When a nanoresonator undergoes vibration, internal damping causes energy dissipation. The parametric modulation of a spring constant effectively pumps in energy that partially compensates for the loss, and this in turn leads to significant quality factor enhancement. This enhancement is observable experimentally as a narrowing and amplification of the resonance peak as described in

chapters 3 and 4. We calculate the spectral response while the pump is fixed at twice the resonance frequency $\Omega_p=0$, while Ω_D varies. As in the previous calculation we write down the equations for $A(T)$ analogous to equation (2.14)

$$\begin{aligned} 2\omega_0 A' + \omega_0 \Gamma A - ihA^* &= -g e^{i\Omega_D T}, \\ 2\omega_0 A'^* + ihA + \omega_0 \Gamma A^* &= -g^* e^{-i\Omega_D T}. \end{aligned} \quad (2.20)$$

After substituting the expression for A^* from the first of the above equations into the second one we obtain a differential equation for the amplitude A .

$$4\omega_0^2 A'' + 4\omega_0^2 \Gamma A' + (\omega_0^2 \Gamma^2 - h^2)A = -ihg e^{i\Omega_D T} - \omega_0 g (\Gamma + 2i\Omega_D) e^{-i\Omega_D T}. \quad (2.21)$$

Two terms on the right-hand side imply that the solution to this equation includes two sidebands vibrating at ω and $\omega_p - \omega$. Hence the total solution assumes the form:

$$A = a e^{i\Omega_D T} + b e^{-i\Omega_D T}. \quad (2.22)$$

After substitution we obtain the solution for spectral responses:

$$\begin{aligned} a &= \frac{\omega_0 g (\Gamma + 2i\Omega_D)}{4\omega_0^2 \Omega_D^2 - (\omega_0^2 \Gamma^2 - h^2) - 4i\omega_0^2 \Gamma \Omega_D}, \\ b &= \frac{ihg^*}{4\omega_0^2 \Omega_D^2 - (\omega_0^2 \Gamma^2 - h^2) + 4i\omega_0^2 \Gamma \Omega_D}. \end{aligned} \quad (2.23)$$

The equation for the parametrically amplified resonance curve for the main side band in terms of original physical quantities has the form:

$$A = \frac{F_0 Q}{m\omega_0^2} \frac{2Q\omega_0(\omega - \omega_0) - i\omega_0^2}{-4Q^2(\omega - \omega_0)^2 + 4iQ\omega_0(\omega - \omega_0) + \omega_0^2(1 - k_p^2/k_t^2)}. \quad (2.24)$$

This resonance curve is substantially higher and narrower than the regular Lorentz peak without application of a pump. Thus we define the effective quality factor enhancement by using the ratio of the peak frequency to the full width at half maximum (FWHM). In the region much narrower

than the Lorentz peak where $\omega - \omega_0 \ll \omega_0/Q$ the parametric resonator's frequency response is described by the equation:

$$A = \frac{F_0}{m\omega_0} \frac{1}{\sqrt{16(\omega - \omega_0)^2 + \frac{\omega_0^2(1 - k_p^2/k_t^2)^2}{Q^2}}}. \quad (2.25)$$

This is a regular resonance curve with Q then enhanced by $4/(1 - k_p^2/k_t^2)$ and the driving force decreased by factor of 4.

In a simpler case when the parametric pumping is locked to twice the drive frequency $\omega_p = 2\omega$ at the maximum amplification phase, the drive frequency sweep yields the following spectral response:

$$A = \frac{F_0 Q}{m\omega_0^2} \frac{2Q\omega_0(\omega - \omega_0) + i\omega_0^2(1 + k_p/k_t)}{4Q^2(\omega - \omega_0)^2 + \omega_0^2(1 - k_p^2/k_t^2)}. \quad (2.26)$$

This configuration is more convenient to utilize the device in measurement applications such as frequency shift-based sensing.

2.4 GAIN-DYNAMIC RANGE TRADE OFF

We will describe the important differences between parametric amplification and regular linear amplification, focusing specifically upon nanoelectromechanical systems. Regular linear amplification is characterized by gain and linear dynamic range. Dynamic range is the ratio of the largest possible linear output signal to the smallest one, and is usually expressed in dB. The signal ceiling is usually defined by the onset of nonlinearities, while the lowest detectable signal is determined by the amplifier's output noise floor.

The performance of a mechanical device can be characterized by its mechanical noise floor [22] and the onset of nonlinearity. For mechanical systems of submicron sizes, it is extremely

challenging to devise an efficient method of displacement transduction, therefore in most of our experiments the noise in the measurements is dominated by electronic amplifier noise. In the case of signal ceilings, nonlinearity in nanomechanical systems starts at rather low excitation levels, lower than that of electronic amplifiers. As a result the available dynamic range is determined by the mechanical device's signal ceiling and amplifier's output noise floor (see figure 2.2(a)).

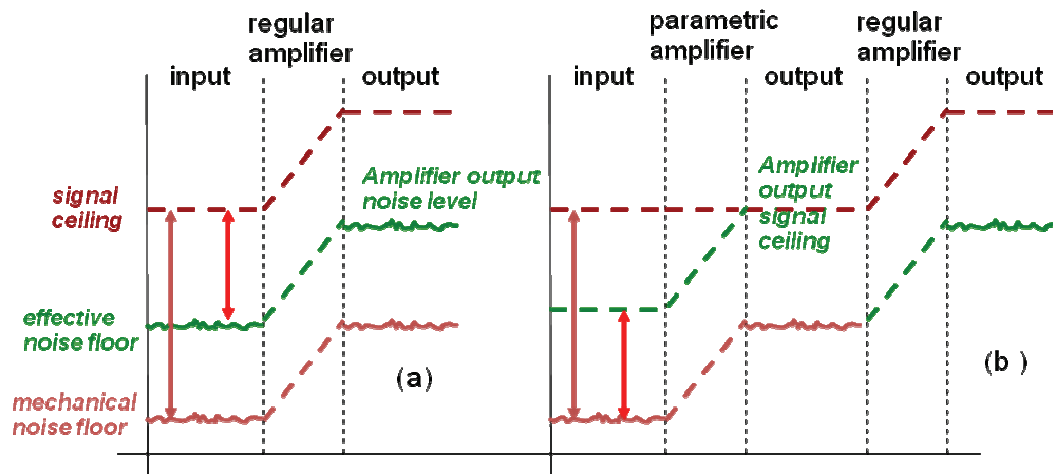


Figure 2.2 (a) Regular linear amplifier operation basics. Dynamic range is determined by mechanical signal ceiling and amplifier's noise floor. (b) Parametric amplifier does not have a noise floor but it has low signal ceiling.

The operation of a parametric amplifier is different than that of a linear amplifier, as described above. To begin with it is phase dependent, but we assume the pump is synchronized, so that it is always at phase difference for maximum amplification. An important feature of the parametric amplifier is that it does not have its own characteristic noise floor, but amplifies the mechanical internal noise the same way it amplifies signal. Therefore use of a parametric amplifier in physical measurements certainly increases the signal resolution, because it can be used in the mechanical

domain in order to match intrinsic NEMS resonator noise to the electric amplifier characteristic noise (see figure 2.2(b)).

To determine the dynamic range we need to consider the largest possible output signal. In the above derivation of parametric amplifier's gain, equation (2.18) implies that the gain diverges when the pump amplitude approaches the threshold value. Experimentally such divergence does not occur because at large amplitudes the small signal equation (2.7) is no longer valid. Instead, in this regime the nonlinearities have to be taken into account. If the Duffing nonlinearity is considered, one finds that the output signal ceiling occurs approximately at the regular onset of nonlinearity in a mechanical resonator [23]. As a result, in the presence of parametric gain the signal ceiling referred to input is smaller than the NEMS device's own onset of nonlinearity, and therefore dynamic range is not increased.

As a conclusion the employment of a parametric amplifier will be advantageous in terms of improving signal resolution by matching intrinsic mechanical noise to the readout amplifier's noise (figure 2.2(b)), but it is not advantageous for increasing the dynamic range.

2.5 BISTABILITY AND PARAMETRIC TONGUE

When the pump amplitude approaches and exceeds threshold, the amplitude diverges according to equation (2.18). Hence Duffing nonlinear terms have to be considered in the equation of motion (2.7) in order to correctly describe the behavior of the NEMS parametric amplifier above threshold [14]. The derivation is similar to the procedure described in sections 2.1 and 2.2 up to equation (2.13). The vanishing term in brackets on the right-hand side of the equation (2.13) now includes additional terms arising from the Duffing nonlinearity:

$$-2i\omega_o A' - i\Gamma\omega_o A - hA * e^{i\Omega_p T} - 3\alpha|A|^2 A - ig e^{i\Omega_D T} = 0. \quad (2.27)$$

Here $\alpha = \frac{\alpha_D}{m} = \frac{Y}{18\rho} \left(\frac{2\pi}{L} \right)^4$ is the reduced (or specific) cubic nonlinearity coefficient with no scaling.

When system is parametrically driven with pump amplitude above threshold $h > \omega_0 \Gamma$ and with no resonance frequency drive applied $g=0$, then the mechanical nanoresonator vibrates at half the parametric frequency. Hence we search for a solution of the form:

$$A = ae^{i\frac{\Omega_p}{2}T} + c.c. \quad A' = i\frac{\Omega_p}{2}ae^{i\frac{\Omega_p}{2}T} + c.c. \quad (2.28)$$

After substituting these expressions into (2.27), the equation for a assumes the form:

$$3\alpha|a|^2 a - \omega_o \Omega_p a + i\Gamma \omega_o a = ha^* . \quad (2.29)$$

Upon first observation, one finds that the trivial solution of this equation, $a=0$ is a valid one for all Ω_p . In order to calculate other possible solutions we solve this algebraic equation for the intensity $|a|^2$.

$$[(3\alpha|a|^2 - \omega_o \Omega_p)^2 + \Gamma^2 \omega_o^2] |a|^2 = h^2 |a|^2 . \quad (2.30)$$

The nontrivial solution is:

$$|a|^2 = \frac{1}{3\alpha} (\omega_o \Omega_p \pm \sqrt{h^2 - \Gamma^2 \omega_o^2}) . \quad (2.31)$$

A detailed analysis of this solution is given in [14, 24]. As was mentioned earlier, the nontrivial solution is valid only above threshold $h > \omega_0 \Gamma$. One of the most notable features of the behavior of this solution is that there is a region in the plane of Ω_p and h where the trivial solution becomes unstable. The instability region can easily be calculated by requiring $|a|=0$ in the expression (2.31). The threshold is situated at

$$\Omega_p = \pm \sqrt{h^2 - \Gamma^2 \omega_0^2} \quad (2.32)$$

It has a shape of a tongue (discussed in [14]), hence it is commonly referred to as an instability tongue or parametric tongue. Its lowest point is $\Omega_p=0$ and $h= \Gamma\omega_0$, which is exactly at the parametric threshold introduced in equation (2.18).

If the parametric drive is above threshold and the frequency is swept upward, then outside the instability region the resonator is at rest. At the left edge of the tongue the trivial solution loses stability and the resonator undergoes a supercritical bifurcation, which is characterized by motion at half the parametric frequency. As the frequency is swept further the amplitude of motion rises with a square root dependence on frequency according to equation (2.31). Subsequently after crossing the right edge of the tongue, the solution becomes bistable, causing the oscillations to continue to rise until other factors, particularly nonlinear viscous damping causes the vibration to drop to the trivial solution (see [14]). On the other hand when the frequency is swept downward, the motion does not start until the edge of the instability region is crossed because the trivial solution is also stable to the right of the parametric tongue. When the frequency reaches the right edge of the tongue, a subcritical bifurcation occurs and the amplitude jumps to a high value and then decreases to zero at the left edge of the tongue. Thus downward sweeps can be used to map the instability region.

SUMMARY

This chapter is crucial for grasping the theoretical background needed to understand the physics of the studied system and thus be comfortable reading subsequent chapters. The mechanical nanoresonator is a standard topic covered in many textbooks. Here we outlined the most important

parts that will be used later. The rich behavior of the parametrically excited nanomechanical resonator is studied and exploited in a variety of ways in chapters 4, 7, and 8.

Chapter 3

LORENTZ FORCE VHF PARAMETRIC AMPLIFIER

The first realization of high frequency NEMS parametric amplifier was demonstrated by Darrell Harrington and Michael Roukes [25]. In their experiment parametric pumping is achieved using a scheme where the tensile stress of nanomechanical resonator is modulated by magnetic Lorentz force. This chapter presents the next generation of similarly designed parametric resonators scaled up to a very high resonance frequency 130 MHz. The results of the experiments and limitations of this design are discussed in the latter part of this chapter.

3.1 LORENTZ FORCE PARAMETRIC AMPLIFIER DESIGN

The first implementation of nanomechanical parametric amplifier employs the magnetic Lorentz force as a method of spring constant modulation [26]. This mechanism is used in order to obtain broad dimensional and frequency scalability because it proved to be scalable up to microwave NEMS applications [27]. Our parametric resonator design is based on the coupled beam structure shown in figure 3.1. The “H”-shaped structure consists of a signal beam with length L_1 , width w_1 , and thickness t_1 supported by two pump beams with corresponding dimensions L_2 , w_2 and t_2 . By applying a periodic force to the external sides of the pump beams we are effectively changing the signal beam's tension, thus modifying its spring constant.

The device was fabricated by newly developed 2-step process out of 100 nm epitaxially grown structural layer of silicon carbide on silicon. The first electron beam lithography step patterned pump beams followed by evaporation of 70 nm silicon oxide in order to serve as isolation between metal electrodes as well as dry plasma etching mask, thus avoiding undesirable wet etching steps.

The second step included electron beam lithography of the pump and signal electrodes followed by 5 nm titanium on top of 40 nm aluminum layer

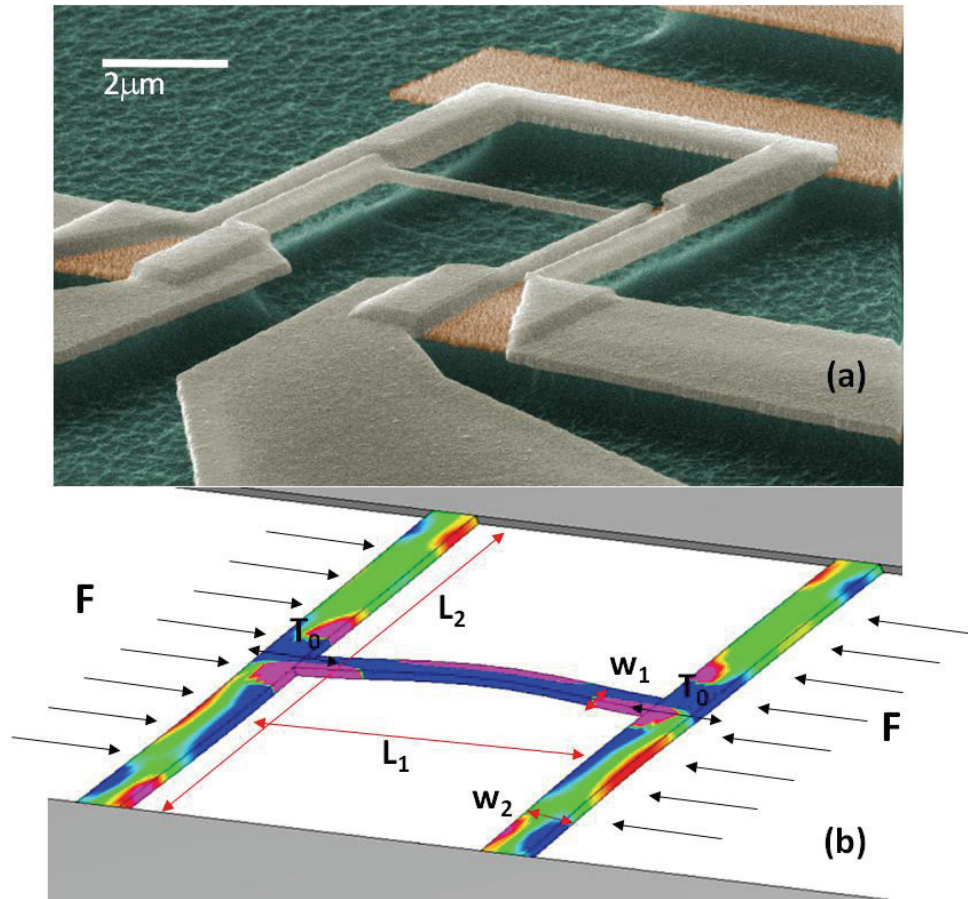


Figure 3.1 (a) SEM image of the Lorentz force NEMS parametric amplifier. The device dimensions are: $L_1=3.1\mu\text{m}$, $L_2=5.1\mu\text{m}$, $w_1=150\text{nm}$, $w_2=630\text{nm}$, $t_f=100\text{nm}$. (b) Finite element modeling of the parametric amplifier's stress profile distribution.

deposition. This step is especially challenging because it included smallest features of 100 nm pitch and required 20 nm alignment precision. In addition to their function as electrical conduction purposes the metal layers served as a mask for dry plasma etching. An electron coupled resonance plasma (ECR) etching system with nitrogen trifluoride was used for anisotropic silicon carbide

etch as well as subsequent isotropic silicon suspension etch, thus avoiding undesirable wet etch steps.

According to equation (2.5) from the previous chapter, the resonance frequency shifts when the longitudinal tensile stress is applied to the beam. The corresponding spring constant change is then given by:

$$k_p = \frac{0.3kL_1^2\sigma}{Yw_1^2}. \quad (3.1)$$

When a DC current I_{DC} is passed through the pump beam electrode in magnetic field B the tension force is given by:

$$T_L = \sigma w_1 t_1 = -2BI_{DC}L_2\zeta = -\frac{2BL_2\zeta}{R_{pump}}V_{DC}, \quad (3.2)$$

where $\zeta=0.23$ is a geometrical factor that accounts for finite stiffness of supporting beams. R_{pump} is the ohmic resistance of the pump beam electrode (typically 50-100 Ω) and V_{DC} is a voltage drop across it. Numerical finite element simulations were performed to determine the parameter ζ and to optimize the resonator's geometry (Figure 3.1(b)). As a result, the fractional frequency shift due to the force is given by:

$$\frac{df}{f} = \frac{k_p}{2k} = -\frac{0.3BL_1^2L_2\zeta}{Yw_1^3t_1R_{pump}}V = -\xi V, \quad (3.3)$$

where coefficient ξ depends only on magnetic field, intrinsic properties of the material and geometry of the device. The subscript ‘‘DC’’ is intentionally removed because the equation is valid for both DC and RF voltages. Since the expression for threshold stiffness constant modulation amplitude is $k_t = 2k/Q$, the threshold voltage is given by:

$$V_{th} = \frac{1}{\xi Q}. \quad (3.4)$$

This equation is crucial for the analysis of limitations of current design performed later in this chapter.

3.2 MEASUREMENTS RESULTS

All the measurements of Lorentz force parametric amplifier were performed at low temperature under high vacuum conditions.

After fabrication the sample was wirebonded to a specially designed sample stage that included a CERNOX resistive temperature sensor along with a resistor for heating purposes. The sample stage was then mounted to a holder that was fixed inside a “dipper” cryostat. After pumping its interior to less than 10^{-6} torr, the dipper was precooled in liquid nitrogen before being immersed in liquid helium. The dewar for these experiments was equipped with a superconducting coil capable of producing magnetic fields up to 8 Tesla. The magnet was used for magnetomotive actuation and detection of the beam's motion [28]. The first measurements performed after a given device is cooled to its lowest equilibrium temperature around 10K is the resonance search. All the candidate peaks have to be carefully examined by performing magnetic field magnitude sweeps in order to determine their authenticity.

Overall three samples were carefully measured during the course of these experiments. Most of the data presented were taken with the last of these devices, although the first device was the only one with which the mechanical spectral response was investigated in detail. In order to facilitate the search for resonant peaks the first device was first rotated 90° so that out-of-plane modes of vibration were detectable. In this condition the device in Fig 3.1 produces two resonance peaks at 28.7 and 44.7 MHz. Their magnetic field sweeps are shown in figure 3.2(a),(b). During these sweeps the background level was constant but the amplitude of the mechanical motion increased with the magnitude of magnetic field, as expected. The sample stage was subsequently rotated back to 0° degree orientation and two more out-of-

plane resonances were found at frequencies 78.3 and 110.8 MHz (see figure 3.2 (c),(d)). The nature of all of the detected peaks was verified by finite element modal analysis, in which all the geometrical parameters including various thickness layers and material properties were taken into account. The mode shapes are shown in the insets in figure 3.2.

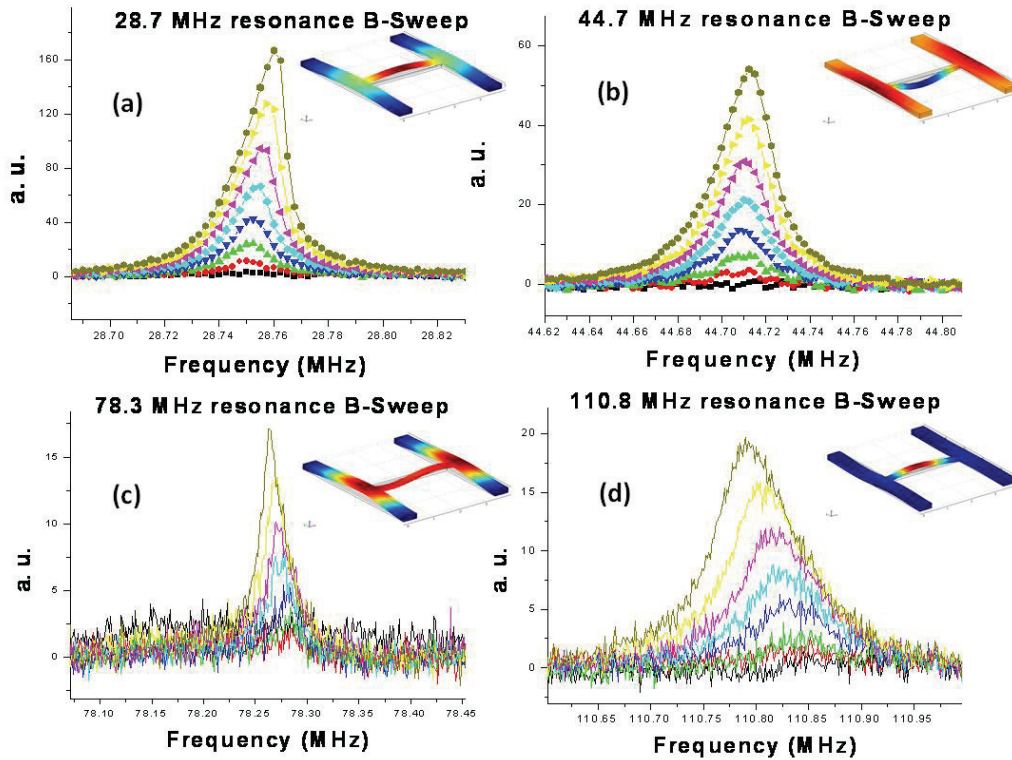


Figure 3.2 The spectral response of the Lorentz force parametric amplifier “H” structure.

The mode frequencies determined in finite element analysis are quite close to the ones measured, as shown in table 3.1. The principal mode we operate with is the fourth in these studies, with a resonance frequency of 110.8 MHz.

Mode Number	1	2	3	4
Measured Frequency MHz	28.7	44.7	78.3	110.8
Calculated Frequency MHz	33.8	60.8	91.4	109.4
Quality Factor	2900	3300	5000	2200

Table 3.1 The physical parameters of measured vibration modes of H-structure

After we confirmed the observation of signal beam fundamental in-plane mode we characterized the Lorentz force tuning capability of the signal beam by sending a DC current through the pump beams. As shown in figure 3.3(a) the signal beam resonant frequency is tuned downward whenever DC bias current is passed through the pump beams, regardless of the bias current polarization. However, this downward frequency tuning is not symmetric with respect to the applied bias voltage. Careful and repeatable measurements indicate that this is a result of superposition of the linear tuning due to Lorentz force tension and symmetric downward tuning due to Joule heating of the device caused by DC current bias. As we go to higher frequencies by shrinking the device size, Joule heating crucially influences the tunability of parametric resonators with this design.

Examination of the change in quality factor with respect to the applied DC bias, as shown in the inset on figure 3.3(a) confirms that the symmetric downward tuning arises from heating. Using known experimental parameters for this device the effect was quantitatively modeled and subtracted, yielding the linear tuning due to tension introduced by Lorentz force only (equation (3.3)). The result is shown in figure 3.3(b); the blue straight line is a theoretical prediction using the geometrical parameters of the fabricated device.

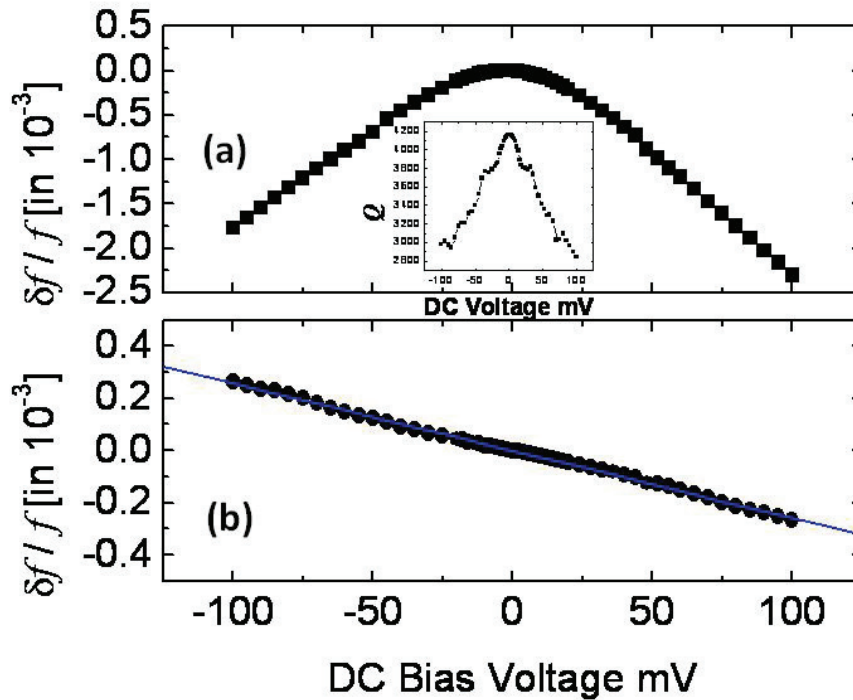


Figure 3.3 (a) Total tuning due to DC bias voltage, the parabolic shape is due to heating. (b) The pump beam Lorentz force tuning obtained after symmetrization of the parabolic curve, the straight line is the theoretical prediction for frequency tuning due to Lorentz force equation (3.3). Inset in (a) shows the quality factor drops as DC bias voltage is increased

While sending RF power into the pumping beam the signal beam's resonance frequency and quality factor shift downward due to the parasitic effect of Joule heating. However, we performed regular reflection measurements of the resonance peak of the signal beam after fixing the pump at twice the new resonance frequency using the setup shown in figure 3.4. Peak narrowing as well as an increase in peak height was observed (see figure 3.5) due to the linear part of the frequency tuning.

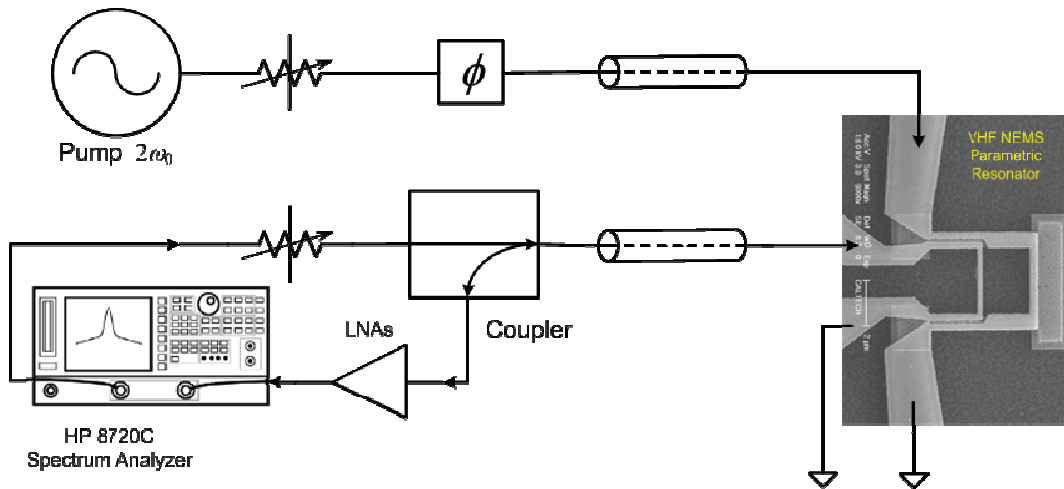


Figure 3.4 The setup for Q enhancement measurements. The bottom part is a regular reflection measurement scheme, which was always used to characterize resonances during the course of an experiment.

The shapes of the curves closely match those predicted theoretically from equation (2.23). The obtained quality factor enhancement is limited because the original quality factor drops as pumping voltage goes up (inset in figure 3.3(a)). The threshold voltage increases as well according to equation (3.4). With no pump Q of the beam is around 4000, but when enough pump power is applied to obtain measurable resonance peak change, Q drops to 2500 at $V_{rms}=100$ mV, and further drops to 1700 at $V_{rms}=280$ mV. Thus the maximum quality factor enhancement observed is 3.0 at pump voltage of $V_{rms}=240$ mV. Quality factor increases from 2200 to approximately 7000 in this case. Hence Joule heating model is extremely critical for understanding the frequency scalability and practical performance available from the Lorentz force mechanical parametric amplifier.

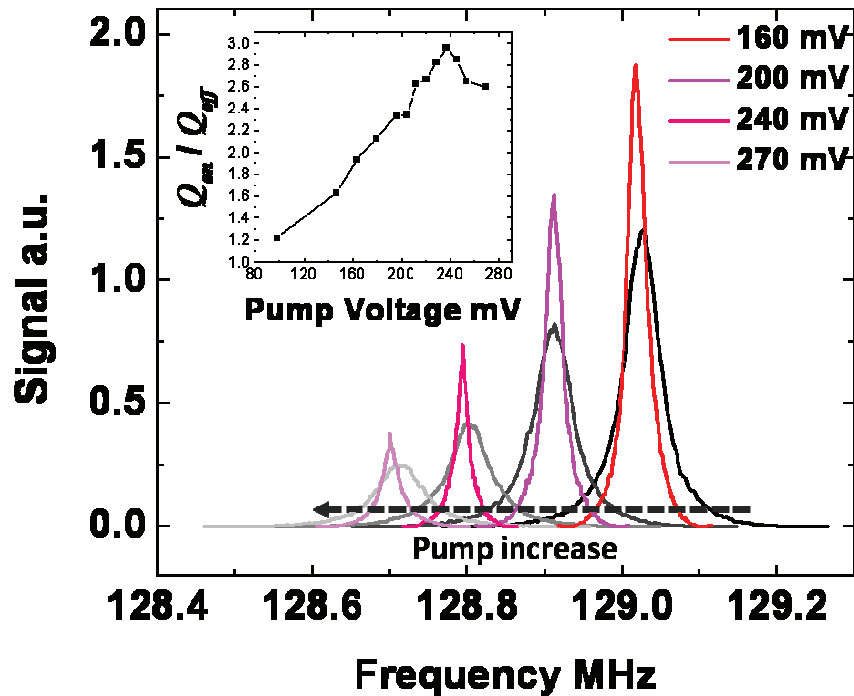


Figure 3.5 The observed direct evidence of quality factor enhancement as pump is increased. The frequency and Q with no pump both drop down due to heating. The inset shows relative quality factor enhancement

3.3 HEATING MODEL

In order to quantitatively assess the problem of practical limits of the Lorentz force parametric amplifier we devise a heat transfer model where we calculate transfer rates between all the important stages of the heat flow. A schematic of the model is shown in figure 3.6; we initially assume uniform Joule heating in the metal electrodes of pump beams changes their electron temperature. Hot electrons in turn heat phonons in metal layer due to electron-phonon interaction with associated thermal conductance G_{ep} . Metallic phonons subsequently transfer heat to a dielectric SiO_2 layer through the Kapitza thermal boundary conductance G_K and further to the layer SiC through its much larger conductance G_{KS} [29, 30] which thus can be neglected. Finally the

incoming power and lateral dissipation rate into the substrate determine temperature profile of the pump beam elastic material.

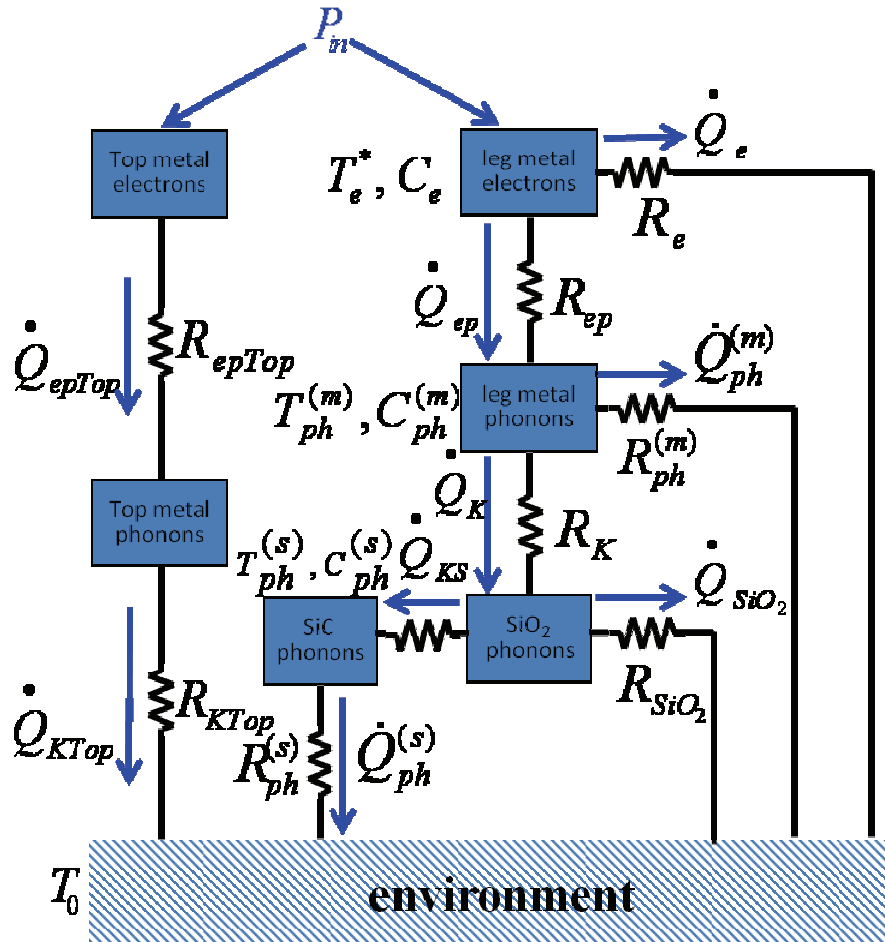


Figure 3.6 A schematic model of low temperature Joule heating for the H-structure mechanical parametric amplifier. Thermal resistances are shown as R . In the text we mostly characterize these as conductances, designated as G with appropriate indices. (In this chapter T is absolute temperature (not the slow time)).

In addition, associated with each intermediate thermal pathway there is a parallel pathway directly into substrate. All of them are taken into account in the model calculation. We find that the

top part of pump beam metal electrode has negligibly small temperature difference from that of the substrate due to relatively large values of G_K as pointed out in later calculation.

The electron thermal conductivity for the heat flow from metal electrode directly into the substrate can be estimated from Wiedemann-Franz law in Sommerfield model [31]:

$$\kappa_e = \frac{\pi^2}{3} \left(\frac{k_b}{e} \right)^2 \sigma_{el} T. \quad (3.5)$$

Therefore in the present case the thermal conductance associated with metal electrons is given by:

$$G_e = \frac{\pi^2}{3} \left(\frac{k_B}{e} \right)^2 \sigma_{el} \frac{A_{pump}}{L_{pump}} T, \quad (3.6)$$

where k_B and e are the Boltzman constant and electron charge respectively (T is absolute temperature in this chapter). Electrical conductivity $\sigma_{el} = L_{pump}/A_{pump}R_{pump}$ is estimated geometrically for particular operation conditions, while A_{pump} and L_{pump} are the crossectional area and length. The latter two parameters are evaluated by properly modeling nonuniform distribution of metal layer on the legs. The heat flux is calculated using the expression:

$$\dot{Q}_e = \int_{T_0}^{T_g} G_e dT. \quad (3.7)$$

Thermal conductance associated with heat transfer between electrons and phonons in metal is given by:

$$G_{ep} = C_e(T) \Gamma_{ep}(T) V_{eff}, \quad (3.8)$$

where $C_e(T) = \frac{\pi^2}{2} \frac{nk_b^2}{\varepsilon_F} T$ is the electron heat capacity per unit volume calculated using the

Sommerfield model[31], and n and ε_F are the number density and Fermi energy of the metal

electrons respectively. Here V_{eff} is the effective volume and Γ_{ep} is the relevant electron-phonon scattering rate, which is given by [32]:

$$\Gamma_{ep} = \frac{4\zeta(3)}{3\pi} \frac{k_b^3 \varepsilon_F^2}{\hbar^4 v_s^4 v_F \rho} T^3. \quad (3.9)$$

Here v_s is the velocity of sound and ζ is a Riemann function, $\zeta(3)=1.202$.

Special care has to be taking care when evaluating the thermal phonons heat flux that escapes the resonator through the ends of the support beams. This calculation is valid for both the metal aluminum and structural silicon carbide layers, if appropriate parameters are utilized for each layer. We assume that the power is uniformly distributed in the metal layer, and then solve the thermal transfer differential equation:

$$\kappa \frac{d^2 T}{dy^2} = \frac{\dot{Q}_{li}}{L_2 w_{2eff} t_{metal}}. \quad (3.10)$$

We apply the boundary conditions $T=T_0$ at $y=0$ and $y=L_2$, because G_K is relatively large as we have mentioned earlier. A similar equation is solved for the phonons in SiC structural layer of the resonator. The thermal conductivity is estimated assuming a simple diffusive model $\kappa \approx c_v v_s l_{mfp} / 3 = \alpha_p T^3$. Here c_v is the heat capacity per unit volume, it is calculated using Debye model

$c_v = \frac{12}{5} \pi^4 k_b n \left(\frac{T}{T_D} \right)^3$. We assume a boundary scattering limited value for the effective phonon

mean free path $l_{mfp} \approx 1.12 \sqrt{A}$, where A is the smallest crosssection of the beam, based on previous studies of thermal transport in nanoscale beams [33]. The formulae we deduce here are valid below 40-50 K, which is suitable for our case since we operate at ambient temperature $T_0 \approx 10$ K. If the resulting temperature rises beyond this range then the expected heating is expected to be even larger than the model's predictions, because thermal conductances in this regime begin to saturate

and stop increasing with temperature. In that case, the estimated temperature is certainly lower than experimental.

From the thermal diffusion equation (3.10) we obtain the steady-state spatial temperature profile,

$$T(y) = \sqrt{T_0^2 - 2\beta \frac{y^2}{L_2} + 2\beta \frac{y}{L_2}}, \quad (3.11)$$

where $\beta = \sqrt{T_0^4 + \dot{Q}_{it} L_2 / \alpha_p w_{2eff} t_{metal}}$. Equation (3.11) implies that uniformly distributed Joule heating in aluminum wire, whose ends are held at constant temperature, results in parabolic-shaped temperature distribution of the electrons in the metal. Hot metal electrons subsequently heat metal phonons according to our model (Equations (3.8) and (3.9)), therefore in the first approximation we assume the power transferred to the phonons is also uniform along the length of the beam, it is numerically calculated average temperature from Equation (3.11). Similar procedure is performed for subsequent thermal pathways in figure 3.6. Finally when we reach the phonons of the structural layer we note similar peak shaped temperature profile with a maximum at the center is developed in pump beams, hence the signal beam has maximum temperature value at its ends, and there is no additional power distributed in it. As a result the signal beams are thermalized to exactly the maximum temperature from Equation (3.11). The expression for structural layer phonon thermal conductance is then given by:

$$G_{ph} = 8 \frac{\alpha_p w_2 t_2}{L_2} T (2T^2 - T_0^2). \quad (3.12)$$

Let us now consider heat conductance between phonons in the metal and semiconductor layers. The thermal transport between two solid materials at low temperatures has been studied in past

decades both experimentally and theoretically. Two theoretical models, such as the acoustic mismatch model and diffuse mismatch model [29], adequately explain solid-solid thermal boundary resistance. The Kapitza conductance is given by:

$$G_K = 4\sigma_K A_{metal} T^3 \quad (3.13)$$

where $\sigma_K=900 \text{ W/m}^2\text{K}^4$ (for SiO₂–Al boundary) is a constant parameter, which depends only on contacting materials, the value we employ here is for SiO₂–Al boundary [29]. For all the temperatures above 10K this value is at least 10 times larger than $G_{ph}^{(R)}$ associated with structural layer phonon thermal conductance. Previous studies of Kapitza conductance coefficient for SiO₂–Si boundary [30] yield the value $\sigma_K=9000\text{W/m}^2\text{K}^4$, which is an order of magnitude higher, and therefore silicon oxide and silicon carbide can be treated as a single layer.

Given the previous discussion we now have five equations of the type (3.7) for thermal paths of figure 3.5 with their corresponding relations:

$$\begin{aligned} \dot{Q}_{ep} &= \dot{Q}_{ph}^{(m)} + \dot{Q}_K, \\ \dot{Q}_K &= \dot{Q}_{ph}^{(s)}, \\ P_{leg} &= \dot{Q}_e + \dot{Q}_{ep}. \end{aligned} \quad (3.14)$$

Solving these equations numerically yields the temperature of the resonator which depends on pump power. We use this to evaluate the degradation of the parametric threshold. In order to validate the model, an experiment was performed where the resonance frequency dependence on sample stage temperature was measured. When pump power is applied to the pump beams the resonance frequency of a signal beam serves as an effective thermometer. The green curve in figure 3.7(a) is the frequency shift observed when the sample stage is heated up while temperature is measured by an external sensor mounted to the stage. The other two curves in figure 3.7(a) show

relative resonance frequency shift for DC and AC voltages applied versus temperature, which is evaluated using the model described above. The agreement confirms that the model reliably predicts the temperature of the device.

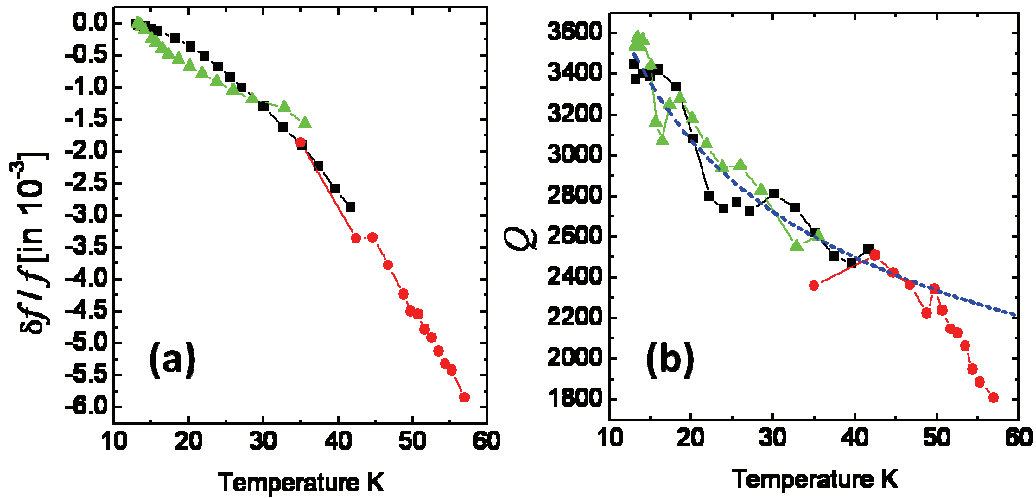


Figure 3.7 Comparison of frequency (a) and Q (b) dependence on device temperature, where the latter is either measured directly via a temperature sensor on the sample stage or calculated from applied DC or AC voltage using the model developed.

We now perform an analysis to evaluate the practical scalability of this design for VHF mechanical parametric amplifier implementation. Equation (3.4) indicates that the threshold voltage of the parametric amplifier is inversely proportional to its quality factor. Based on previous experimental studies of the temperature dependent dissipation in nanoscale mechanical systems [34, 35], we assume the Q decreases as $T^{-0.3}$ for SiC NEMS. Combined with our Joule heating model we build a link from a given applied voltage to the quality factor degeneration. Figure 3.7(b) shows the predicted quality factor values in comparison with what we measure experimentally when the device is heated via DC or AC applied voltages or by direct heating the sample stage.

The dashed line shown here is the $Q \sim T^{-0.3}$ relation for comparison. Therefore the model correctly predicts quality factor values up to 40-50 K (corresponding voltage is around 200 mV) and then dissipations grow even faster.

Taking into account the above heating model and semiempirical law of quality factor temperature dependence, we estimate the threshold voltage of parametric amplifier at given Joule heating power input. Figure 3.8 shows the experimental and theoretically expected relation of threshold and applied voltage. The applied voltage is the straight 45° line (red), the intersection point signifies accessible threshold voltage in this plot.

The threshold voltage for self-oscillation is calculated by fitting measured Q -enhanced responses to calculated curve (2.24). The result is shown in figure 3.8. The plot explains the Q enhancement data we have obtained. Initially, as we approach the threshold, the closest we get is $k_p/k_t \approx 0.7$ for $V_{rms} = 240$ mV. Q increases from 2200 to approximately 7000 in this case. At higher voltages threshold increases faster due to faster drop in quality factor. The experimental data fairly well agree with calculated model for temperatures below 40-50K.

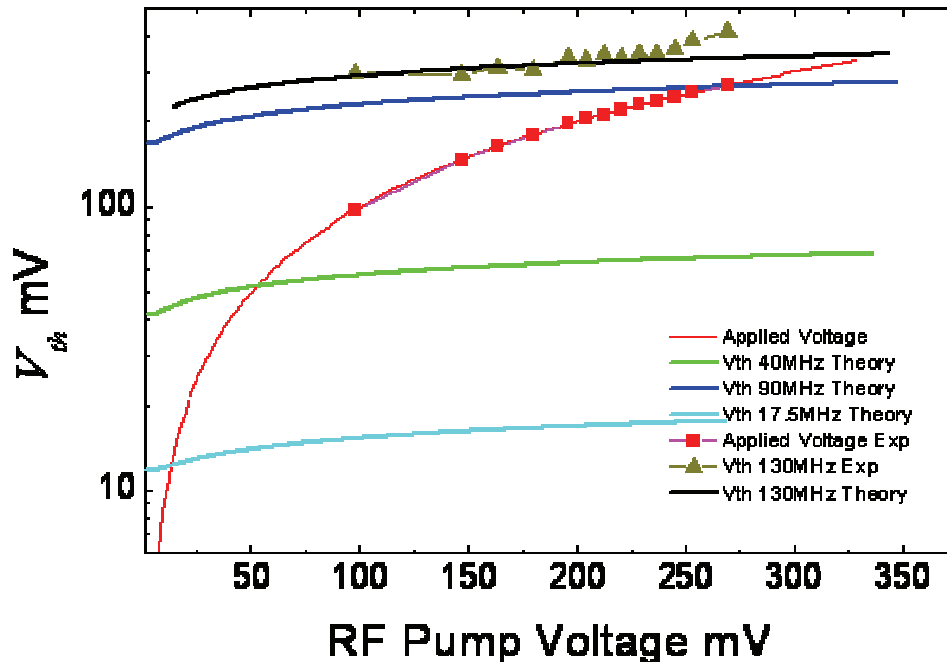


Figure 3.8 The threshold voltage dependence on applied voltage using the heating model. The applied RF voltage is a straight 45° line. The intersection means achievable parametric threshold voltage. Theoretical predictions are for 17.5, 40, 90, and 130 MHz devices. Voltages are given as amplitudes.

The result we obtain here shows that achieving the threshold voltage for the fabricated 130MHz device is accompanied by significant heating of the beam. By varying the geometrical parameters, we performed several more studies of theoretically expected threshold voltages for lower frequency devices (17.5, 40, and 90 MHz).

We conclude that in order to achieve significant gain for a 130MHz “H”-geometry Lorentz force parametric amplifier the beam will heat up by at least 50K, causing the parametric threshold to become unachievable.

SUMMARY

Magnetomotive actuation and detection has a long history of being successfully utilized in NEMS research at our group. Therefore it was natural to devise first implementation of very high frequency NEMS parametric amplifier, so that it employs magnetic Lorentz force frequency tuning. After careful investigation it turned out that the presence of large current for parametric pump has undesirable side effect of immense Joule heating that degrade device quality factor and hence parametric amplifier performance.

To overcome this fundamental obstacle with this design we develop an alternative scheme for parametric modulation of a tensile stress of a nanomechanical doubly clamped beam. The new mode of operation, which is based on piezoelectric electromechanical coupling, does not require a presence of electrical current, hence does not suffer from this limitation

Chapter 4

D-NEMS PARAMETRIC AMPLIFIER

This chapter gives a brief introduction into the properties of multilayered piezoelectric nanoelectromechanical devices. The most important characteristics such as efficient actuation and frequency tuning are discussed in detail. Parametric amplification achieved by piezoelectric mechanical coupling is presented. Large gain, substantial Q enhancement, and frequency stability improvement are demonstrated. Finally the region of parametric instability is explored.

3.1 D-NEMS PIEZOELECTRIC FREQUENCY TUNING

One of the most intuitive and straightforward ways to achieve a wide range of frequency tuning in nanomechanical resonators is to use piezoelectric electromechanical coupling. Indeed piezoelectricity is a well-known phenomenon that directly converts electric field into mechanical strain. In order to achieve the highest possible efficiency for actuation and frequency control, we design multilayered piezoelectric structures. As the thickness of the active material becomes smaller it can get increasingly more difficult to retain piezoelectric properties and to apply significant electric field without voltage breakdown. Binary noncentrosymmetric materials, such as III-V semiconductors, grown by molecular beam epitaxially, retain single-crystal structure and therefore their intrinsic piezoelectricity down to very small thicknesses.

To demonstrate D-NEMS parametric amplifier we fabricate the devices from 200 nm thick GaAs pin diodes. These consist of a stack of three layers: 100nm highly n-doped, 50nm insulating and another 50nm layer of highly p-doped gallium arsenide (see figure 4.1). In previous work [36] we have shown that these devices possess a unique combination of properties including efficient actuation and a wide frequency tuning range. The detailed characterization of D-NEMS actuation

is prevented elsewhere [37]; in this section the frequency tuning model and most important experimental results are described.

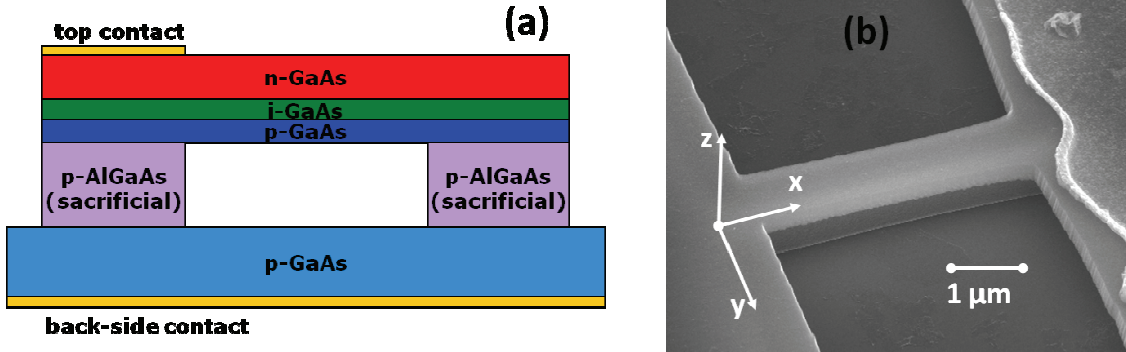


Figure 4.1 (a) Schematic of a multilayered piezoelectric doubly clamped beam made of MBE-grown 200 nm thick GaAs pin diodes. These consist of a stack of three layers: 100nm highly n-doped, 50nm insulating, and a 50nm layer of highly p-doped gallium arsenide. (b) SEM image of a 4 μ m long device.

We base our derivations on the canonical constitutive piezoelectric equations that express the relation between the stress σ , strain s , electric field \mathbf{E} , and electric displacement field \mathbf{D} . These are written in either a stress-charge or strain-charge form. For these derivations we employ the latter:

$$\begin{aligned} s &= c_E \sigma + d^T \mathbf{E}, \\ \mathbf{D} &= d \sigma + \varepsilon_T \mathbf{E}, \end{aligned} \quad (4.1)$$

where s and σ are six component while \mathbf{E} and \mathbf{D} are three component vectors. Here c_E is the 6 by 6 compliance matrix, d^T is 6 by 3 inverse piezoelectric matrix, d is 3 by 6 matrix of piezoelectric constants, and ε_T is the dielectric constant matrix.

The GaAs heterostructures were grown in (001) orientation, thus when voltage is applied across the top and bottom electrode an electric field is developed in the z-axis direction (figure 4.1(b)).

Therefore equations for the components that describe our system, where the beam is oriented along x-axis, are:

$$\begin{aligned} s_{xx} &= c_{E_{xx},xx} \sigma_{xx} + d_{31} E_z, \\ D_z &= d_{31} \sigma_{xx} + \varepsilon_{GaAs} E_z. \end{aligned} \quad (4.2)$$

Previously in chapter 2 we modeled frequency tuning under longitudinal tensile stress σ_{xx} and arrived at an expression (2.5). In the present case the stress is developed only in a narrow middle layer of a thickness t_m . Hence, the expression for the absolute frequency shift assumes the form:

$$\delta f = \frac{0.276 t_m \sigma_{xx}}{t_h^2 \sqrt{Y\rho}}. \quad (4.3)$$

Tensile stress σ_{xx} is the parameter we shall determine from the set of equations (4.2). In order to do this, we first solve the equations with doubly clamped beam boundary conditions, which require longitudinal strain to vanish everywhere $s_{xx}=0$. Then the first equation in (4.2) yields:

$$c_{E_{xx},xx} \sigma_{xx} = -d_{31} E_z = d_{31} \frac{V}{t_m}, \quad (4.4)$$

where in the simplest approximation V is a voltage across the thickness of the resonator, and $c_{E_{xx},xx}$ is the inverse Young's modulus. Hence the stress is given by:

$$\sigma_{xx} = Y d_{13} \frac{V}{t_m}. \quad (4.5)$$

Substituting this expression into equation (4.3) yields the formula for the absolute frequency tuning:

$$\delta f = \frac{0.276 d_{13}}{t_h^2} \sqrt{\frac{Y}{\rho}} V. \quad (4.6)$$

One of the first important conclusions we draw from this equation is that the absolute frequency shift is independent of length. In order to experimentally test these predictions we fabricate six

doubly clamped beams all on the same chip and sharing the same electrodes with lengths ranging from 3 to 8 microns.

Fabrication consists of the following four steps:

(1) Large wirebond pads are defined photolithographically followed by deposition of Ti/Au/Ti layer. The first 5 nm of titanium serve as an adhesion layer between the gold and gallium arsenide. The next 50nm of gold is the wirebond metallization, which is not removed by wet HF suspension etch. The top 50 nm titanium layer serves as a mask for the subsequent argon ion beam milling etch.

(2) Electron beam lithography is used to define the nanomechanical resonators structure, followed by deposition of 50 nm of titanium and liftoff, to serve as a dry etch mask.

(3) Argon ion beam milling is used to provide dry anisotropic etch of GaAs. The acceleration voltage employed is 200V in order to prevent the damage to the layers. The typical etching rate is 12nm/min and is very consistent. This critical property allowed electric isolation of the devices, while preserving shared mechanical ledge.

(4) After 200 nm of GaAs is etched away the chip is dipped into 5% hydrofluoric acid for no more than 5 seconds to remove sacrificial AlGaAs layer. After this etch the chip usually appears to be dirty with residues; these we later remove by a 1 second dip into 1% NaOH solution.

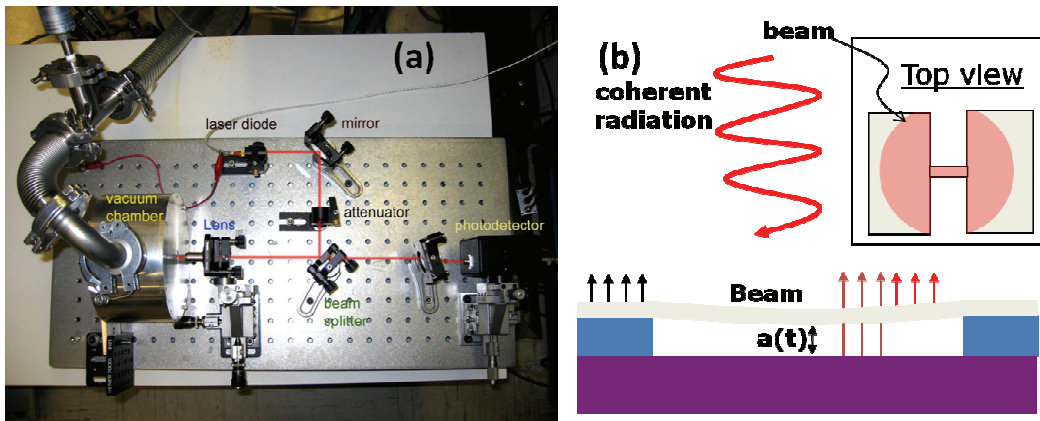


Figure 4.2 (a) Our simple interferometric optical displacement measurement setup. (b) The mechanism of operation is via interfering laser beams reflected from the top of the mechanical beam and the substrate.

After fabrication the chip with resonators is ready to be mounted on a chip holder, wirebonded, and placed into the vacuum chamber ($P=1-10$ mTorr) for experimental measurements. Optical interferometry [38] at room temperature is employed to obtain precision displacement detection, with a setup as shown in figure 4.2. The vacuum chamber is fitted with a transparent sapphire optical window. In order to minimize the impact of light on device performance (e.g., via spurious effects such as heating, photocarrier generation) a 2 mW, 904 nm infrared laser diode is used with a neutral density filter with 10-fold attenuation factor. The beam is focused to a spot of $\sim 10-20$ μm in diameter. A low-noise, high-bandwidth photoreceiver is used for detection. This particular readout mechanism is chosen because it is very easy to implement and troubleshoot, and it provides high mechanical responsivity for out-of-plane displacement, negligible RF background, as well as reliable means for characterization of multiple devices.

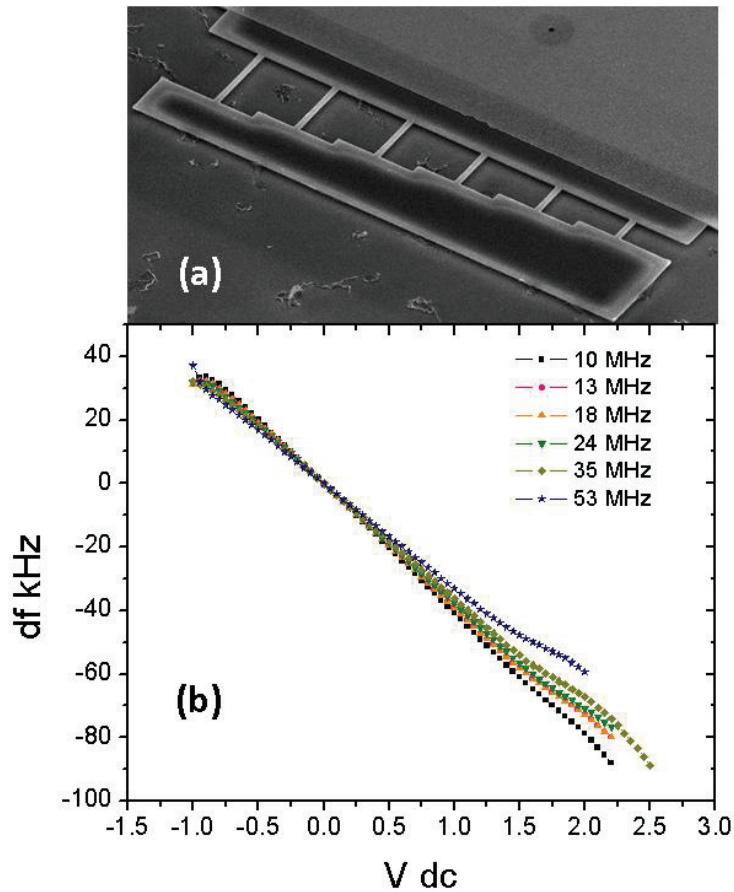


Figure 4.3 (a) SEM image of a set of doubly clamped D-NEMS beams. The geometrical parameters of the beams are $3\mu\text{m} < L < 8\mu\text{m}$, $w \approx 500\text{nm}$, $t_h = 200\text{nm}$. (b) Piezoelectric frequency tuning of the resonators obtained by DC biasing the beams.

Equation (4.6) is experimentally verified by precise measurements of the resonance peak shift with application of DC bias voltage between top and bottom layers of the beam. An SEM image of the set of six different doubly clamped beams with lengths ranging from $3\mu\text{m}$ to $8\mu\text{m}$ and width 500nm is shown in figure 4.3(a). The results from DC tuning measurements are shown in figure 4.3(b).

Note that all the tunability slopes are approximately the same 40 kHz/V, regardless of length and initial fundamental resonance frequency. This is exactly the analytically predicted dependence. A slight 10% degradation of the slope for shorter beams is visible on the plot, which is attributed to the defects during growth or fabrication; the precise nature of the mechanism and its quantitative impact are not understood. The tensile stress tuning via piezoelectricity coupling is characterized by wide range, exceptional linearity, and the absence of associated Joule heating.

4.2 PARAMETRIC GAIN AND Q ENHANCEMENT

Due to remarkable efficiency of D-NEMS stress tuning mechanism parametric resonators become scalable up to very high frequency. The fundamental frequencies of the six resonators shown in figure 4.3(a) vary from 11 to 53 MHz. Their quality factors change from 3300, for the longer, down to 1980, for the shorter beam (a summary is shown in table 4.1). The threshold for parametric oscillation is easily achievable for all these devices.

The parametric amplification gain and effective quality factor enhancement are measured for the shortest beam shown in figure 4.4(a) with parametric pump is set at twice the resonance frequency. A set of parametrically modified resonance peaks is shown in figure 4.4(b). The drive amplitude is kept the same for the four curves displayed. The peak's height boost as well as its width reduction is readily visible as parametric pump is increased. A remarkable quality factor increase of up to 120000 is observed at pump values near the threshold.

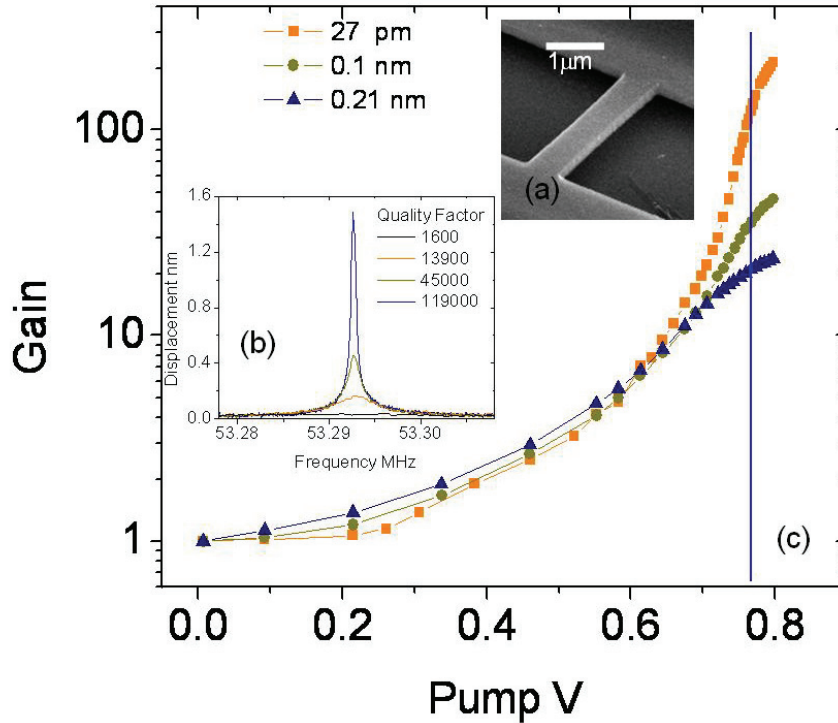


Figure 4.4 (a) SEM image of the shortest, 53.3 MHz doubly clamped beam ($L=3\mu\text{m}$, $w=500\text{nm}$, $t_h=200\text{nm}$). (b) The effective quality factors of the parametrically enhanced resonance peaks are 1600 with no pump, 13900, 45000 with intermediate pump and 120000 close to threshold. (c) The dependence of gain on the pumping amplitude for the three different initial drives. The small-signal gain of 200 was obtained in these experiments.

The results of amplitude gain measurements at maximum phase are shown in figure 4.4(c). The three curves are taken at three different initial drive amplitudes. A small-signal gain of 200 is observed for the 53.3 MHz nanomechanical parametric amplifier. The influence of Joule heating is negligible in this parametric pumping scheme, hence we conclude the scheme to be effortlessly scalable to microwave frequencies. Parametric measurements were done at the slightly lower initial quality factor 1600, because the data were taken few months later. The quality of nanoresonators undergoes slight degradation over long periods of time. The nature of the causes is not understood,

although it is known that III-V material slowly oxidizes when exposed to air, in addition to the fact that it may absorb contaminants that degrade surface quality.

Parametric amplification is especially promising for nanoresonators operating in ambient environment. This is shown by similar parametric amplification experiments performed at atmospheric pressure. The high efficiency of the piezoelectric actuation mechanism allows high excitation mechanical response even at 1 atm. The characteristics for the devices in vacuum and in atmosphere are shown in Table 4.1.

Beam length μm	8	7	6	5	4	3
Frequency MHz	10.9	13.9	18.2	24.8	35.3	53.3
Q in vacuum	3200	3300	3100	3200	2600	2000
Q in atmosphere	130	150	200	250	320	390

Table 4.1 Resonant frequencies and quality factors in vacuum and in air for six beams, of different lengths, fabricated on the same chip.

One interesting observation is that as the beams get smaller the effect of air damping becomes weaker. This effect is consistent with our group's previous measurements of nanomechanical resonators in ambient environments [39]. The physics behind this phenomenon is that when the dimensions of mechanical device approach characteristic mean free path of air at atmospheric pressure the interaction with air is dramatically decreased.

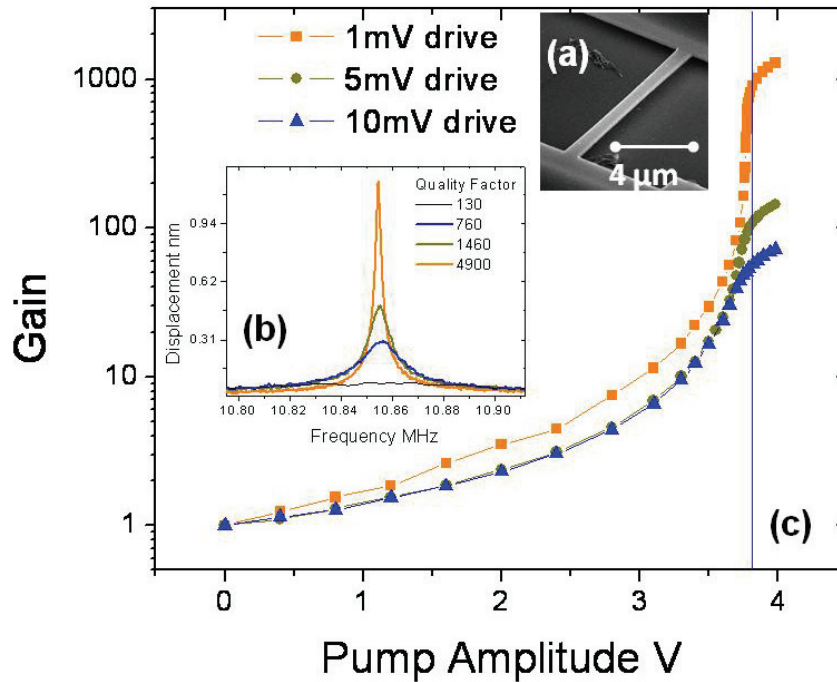


Figure 4.5(a) SEM image of the longest 10.9 MHz doubly clamped beam ($L=8\mu\text{m}$, $w=500\text{nm}$, $t_h=200\text{nm}$). (b) The effective quality factors of the parametrically enhanced resonance peaks are 130 with no pump, 760, 1460 with intermediate pump and 4900 close to threshold. (c) The dependence of gain on pumping amplitude for different initial drives. A small-signal gain of 1000 was obtained in these experiments.

Parametric amplification is measured for the 8 micron long beam shown in figure 4.5(a). Starting from the damped quality factor 130 the enhanced Q of 4900 is plotted in figure 4.5(b). Direct gain measurements in degenerate mode yielded a factor of 1000 amplitude increase due to parametric amplification (see figure 4.5(c)).

Parametric amplification is especially useful when the noise floor is dominated by the readout mechanism. The advantages were discussed previously in section 2.4. Our first trial utilization of parametric amplification is described in the next section.

4.4 PARAMETRIC AMPLIFICATION AND FREQUENCY STABILITY

This section describes a first attempt to measure the improvement of frequency stability for regular sensing applications from parametric amplification. For these measurements we devise a measurement setup where the pump is kept at constant level and is always locked to twice the drive frequency with constant, controllable phase difference. The schematic of the setup is shown in figure 4.6.

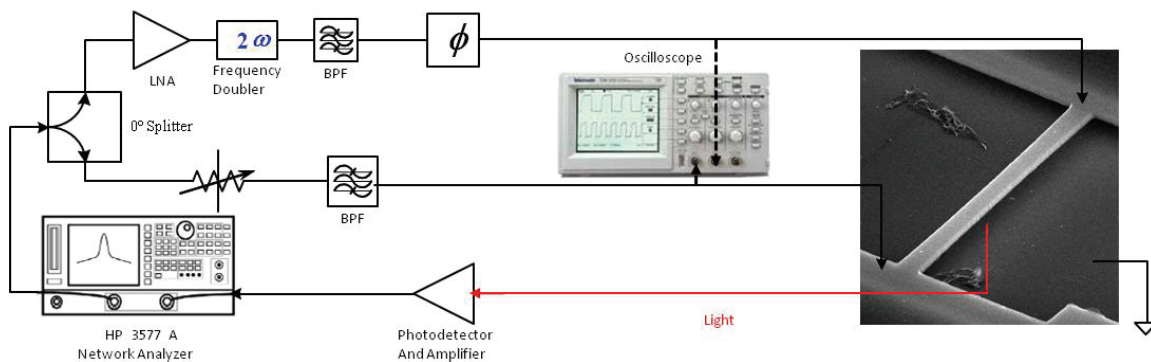


Figure 4.6 The setup for tracking resonance frequency when the mechanical signal is parametrically amplified

An HP3577A network analyzer is used as both the source and detector; it is operated in continuous wave (CW) regime and controlled by an external computer to provide phase locked loop (PLL) operation. The RF output from this network analyzer is split into two paths, the first one is sent through an attenuator and band-pass filter to actuate the resonator. The second is amplified then frequency doubled to serve as parametric pump. The subsequent signal is filtered and its phase carefully adjusted to provide maximum amplification. Filtering is essential because the frequency doubler, amplifier, and network analyzer generate spurious, undesirable harmonics at various frequencies. The settings of the low noise amplifier in pump path and attenuator in drive path are carefully adjusted to provide maximum amplification.

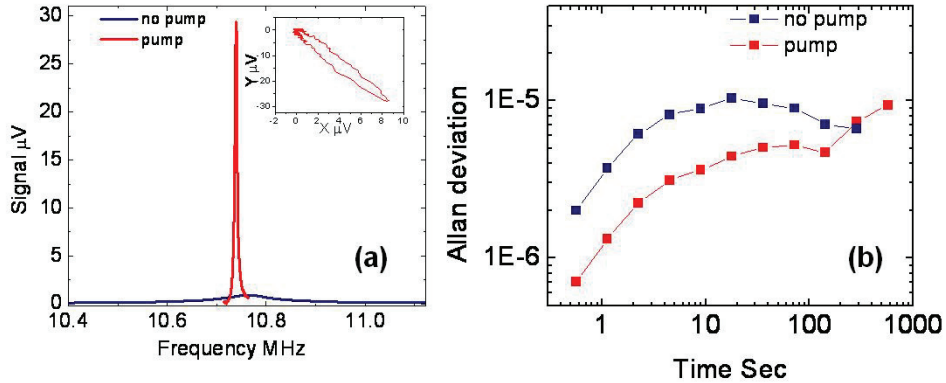


Figure 4.7 (a) Comparison of pumped and unpumped signal under ambient conditions (atmospheric pressure and room temperature) with Q enhancement from 130 (blue) to 2500 (red). The inset shows x and y of the amplified signal, the amplification in one phase is clearly visible. (b) Frequency noise improvement, characterized by Allan deviation as a result of parametric amplification.

The longest beam from the set mentioned in previous section (figure 4.5(a)) with resonance frequency of around 11 MHz is used for this experiment. The resonator is placed into ambient environment where its quality factor drops down to 130. After the parametric pump is locked to twice the resonance frequency, its phase and magnitude are adjusted so that the frequency sweep yields Q enhancement of 2500. Resonance peaks with pump and without pump are shown in figure 4.7(a). The modified curve shape matches the theoretical prediction given by Equation (2.25) very well. Since the gain is high only for one phase direction, the resulting resonance frequency sweep curve, when shown in phase space plot, assumes the form of an ellipse, rather than circle, as shown in the inset in figure 4.7(a).

A computer controlled PLL is used to perform long scans for the frequency noise measurements. The result is shown in figure 4.7(b) where the frequency stabilities of the

parametrically pumped resonance peak and regular Lorentz peak of the same magnitude are compared. The Allan deviation [40] is shown in the plots as a measure of frequency stability.

The result of these first trial measurements shows very promising improvement of the Allan deviation, especially for short averaging times where the noise in frequency detection is dominant. On the other hand, the parametric pump does not improve long-term drift, nor does parametric amplification improve thermal-noise-limited detection sensitivity [41], because parametric amplification only improves signal-to-noise ratio for the case where front-end electronics limit the noise.

The ultimate resolution of mass or charge detection based on resonant nanomechanical sensors is directly proportional to Allan deviation. Therefore these preliminary results demonstrate that there may be significant advantages for employing parametric amplification in such applications.

4.4 PARAMETRIC ACTUATION

Earlier in section 2.5, we discussed the interesting dynamics of parametrically actuated resonator. When the pump is above threshold, the amount of energy pumped into the system is larger than the amount lost due to dissipation; as a result the resonator executes spontaneous oscillations. The mechanical vibration of the resonator occurs at half the pump frequency. The most important characteristics of this intriguing dynamical system, such as its family of instability tongues and the intrinsic bistability of the valid solutions, were discussed in section 2.5.

All of the devices from the set shown in figure 4.3(a) have thresholds that are easily achievable in experimental settings. Most of the preliminary characterizations are performed with 4 μm long 35 MHz beam, shown in the inset in figure 4.8(a). The measurements are carried out with a very simple setup, in which direct drive source is removed while a separate function generator serves as

the parametric pump source. The photodetector output is connected to spectrum analyzer for signal readout.

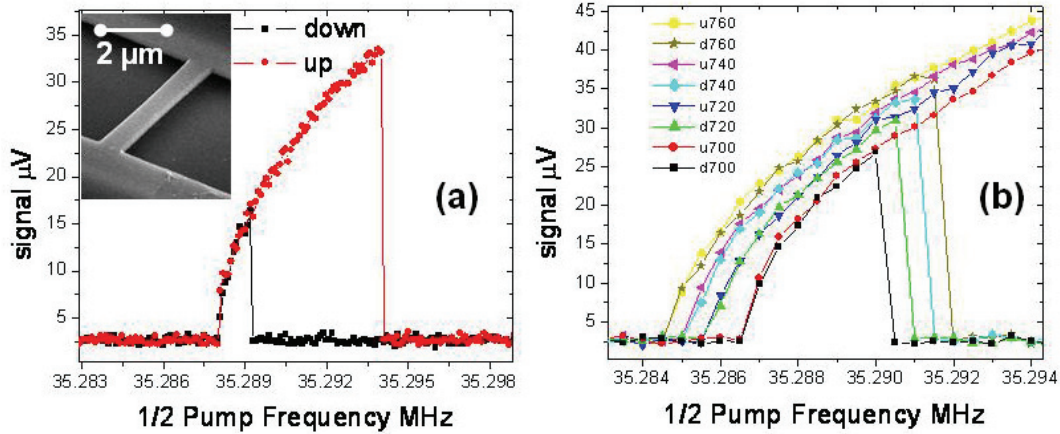


Figure 4.8(a) An example of upward and downward parametric frequency sweeps. The onset of instability and regions of bistability are clearly visible. An electron micrograph of the nanoresonator is shown in the inset. (b) A set of sweeps at steadily increasing parametric pump amplitude.

The results of these measurements are in agreement with theoretical predictions. The plot in figure 4.8(a) shows an example of upward and downward parametric frequency sweeps. A nontrivial solution becomes the only stable one at the left edge of the instability region (around 35.288MHz), as a result the beam starts oscillating. With increasing pump frequency the amplitude of mechanical motion increases with a square-root dependence, in agreement with theoretical prediction expressed in Equation (2.31). When the pump frequency reaches the right edge of the instability tongue, the mechanical motion does not cease since, at these settings, both trivial and nontrivial solutions are stable. Hence the amplitude continues to increase until other factors such as nonlinear viscous damping [14], causes the motion to stop. On the other hand, during the

downward sweep, the mechanical motion jumps to high amplitude at the right edge of the instability tongue (35.289MHz). Later it decreases to zero along the same curve as followed on the upward sweep. All this behavior is clearly evident in figure 4.8(a).

Figure 4.8(b) shows the set of upward and downward frequency sweeps with steadily increased parametric pump amplitude. According to equation (2.32) the instability region should widen as the pump increases. The experimental measurements confirm this prediction. This collection of downward sweeps with steadily increased pump provides a mapping of the parametric instability region of the resonator. Figure 4.9 shows a color plot of a set of parametric downward sweeps; the x-axis is a half pump frequency, the y-axis is pump amplitude in mV_{pp} and the amplitude of mechanical motion signal is represented by color scale. The simplest expression for the shape of the tongue is given by equation (2.32), although variety of factors can influence the ultimate shape in the experiment [12].

The predicted parametric threshold from the quality factor measurement (Table 4.1) and the tunability curve shown in figure 4.3(b) is $678 mV_{pp}$, which perfectly matches what is measured in experiment.

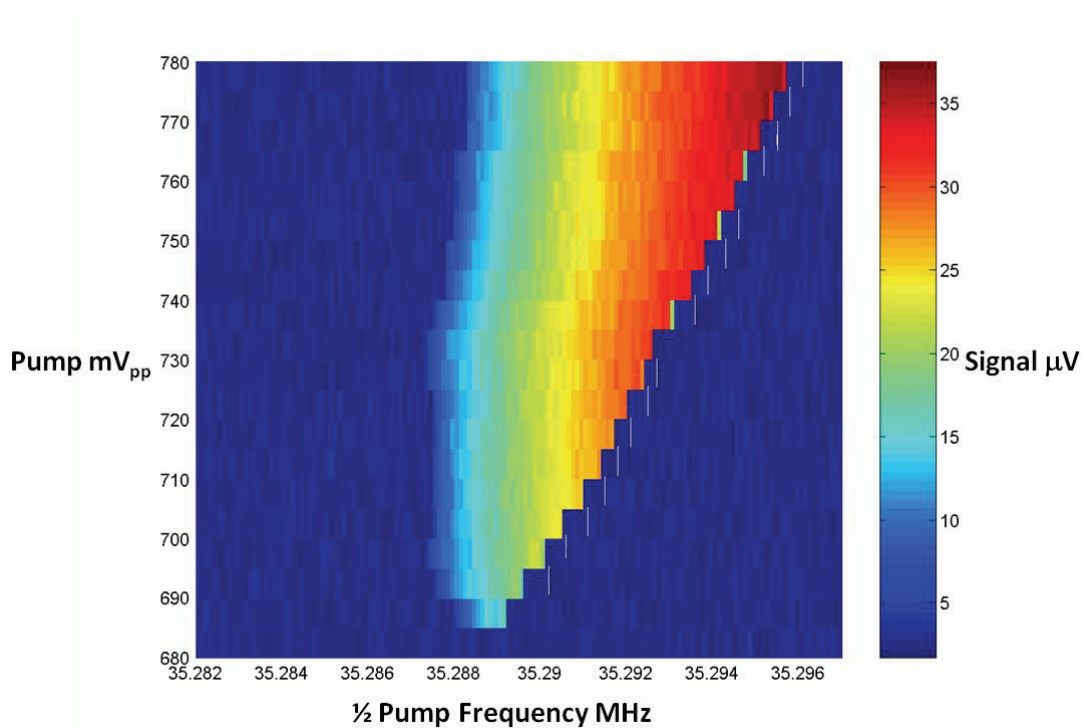


Figure 4.9 Plot of the set of downward sweeps for the parametrically actuated resonator. The amplitude of mechanical motion is color coded.

SUMMARY

Mechanical parametric amplification is a desirable physical phenomenon that can benefit a large variety of nanoelectromechanical systems applications. We demonstrated a novel room temperature scheme of efficient parametric frequency tuning for high-frequency NEMS. The 1000-fold amplitude gain as well as 75-fold Q enhancement is experimentally measured in mechanical system using Lorentz force technique. If used as a preliminary amplification mechanism in mechanical domain before applying conventional linear amplifier, the demonstrated effect is a promising solution for low noise transduction of the motion to an electrical signal. Its advantage for improving frequency stability has been experimentally

measured. Another interesting physical phenomenon parametric actuation is introduced in last section. Chapters 7 and 8 will explore these phenomena in much more complex experiments.

Chapter 5

COUPLING PHENOMENA IN D-NEMS

This chapter studies the interaction between two or more nanomechanical resonators. The nature of the coupling mechanisms is discussed and analyzed. The formalism for characterizing a new basis of vibration modes for strongly coupled nanoresonators is developed and experimentally investigated for two, three and ten devices. Finally a practical implementation of employing a pair of coupled resonators for long-term thermal drift compensation is successfully implemented, resulting in significant improvement of frequency stability.

5.1 VARIETY OF COUPLING MECHANISMS IN D-NEMS

The remarkable level of control of nanoelectromechanical systems displayed by piezoelectric D-NEMS nanoresonators provides a convenient platform for increasing the complexity of the mechanical devices' architecture. The integrated actuation mechanism, wide range frequency tunability and efficient detection scheme provide a straightforward opportunity to investigate the behavior of several interacting nanomechanical resonators. There are a number of physical mechanisms responsible for coupling between the D-NEMS resonators. The most important ones are mechanical and electrostatic. These mechanisms are studied in most detail in this chapter.

Mechanical coupling is the interaction phenomenon that takes place when resonators are fabricated on the same chip and are connected to one another via elastic mechanical structure. The nature of the coupling and its strength strongly depends on the architecture of the nanomechanical resonator. There are several qualitatively varying degrees of mechanical interaction that can be engineered between D-NEMS resonators. To begin with the fabrication of the devices was discussed in previous chapter include wet suspension etch. The etch selectively removes the

sacrificial AlGaAs layer leaving the structural GaAs layers intact. Therefore each beam or cantilever has a short undercut or ledge of a GaAs layer before the substrate. The length of the ledge varies from 600nm to 1.2 μm . Figure 5.1 shows a closer look at the rather long ledges on a typical D-NEMS chip. The ledge is noticeable by a clearly defined border. A few dimension measurements are shown as well. The ledge is also visible on all the SEM pictures presented before.

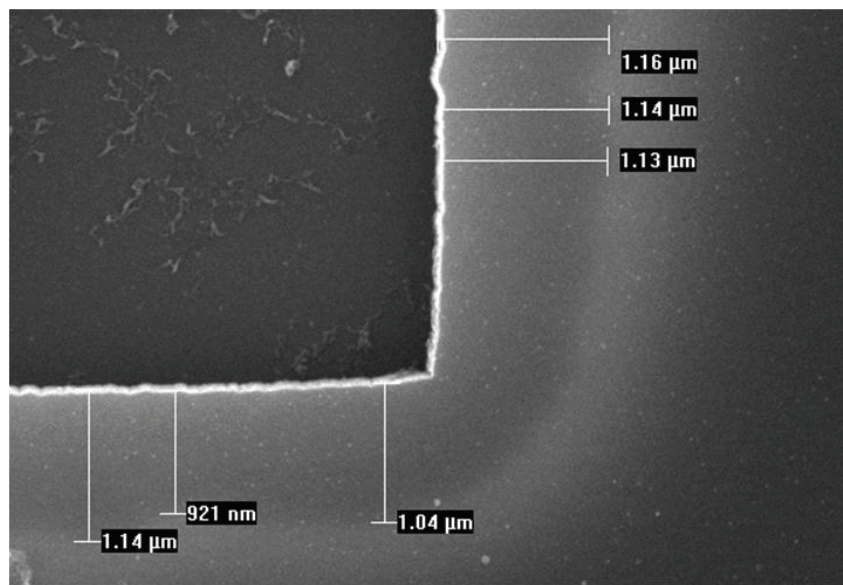


Figure 5.1 A closer look at the ledge which results from the suspension wet etch process. This overhanging undercut is responsible for a strong mechanical coupling in many cases.

The fabrication procedure can be controlled to an amazing degree, thus we can study several architectures with varying degrees of coupling strength through a ledge. Strong coupling cases are studied in the next section. Weaker coupling with isolated top electrodes is discussed in detail later in this chapter and chapter 7. Mechanical interaction through the elastic material is almost always

present, even in the absence of a ledge connecting the two resonators, although the coupling is extremely weak in that case. More detailed investigation of this case is presented in chapter 7.

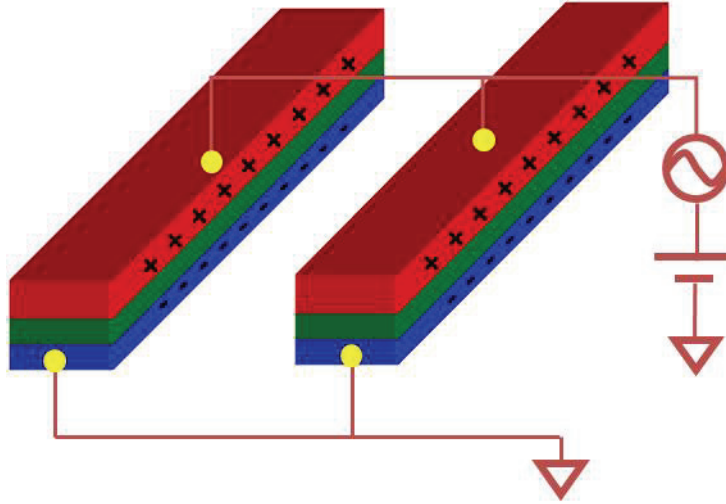


Figure 5.2 Schematic of the dipole-dipole electrostatic interaction between two D-NEMS doubly clamped beams.

The electrostatic coupling is caused by the interaction of electric charges in the layers of D-NEMS devices. When the adjacent beams are polarized by an externally applied voltage their top and bottom layers are charged (see previous chapter). As a result dipole moments are formed in each resonator. In the case of a common top electrode as schematically shown in figure 5.2, the dipole moments are identical, and thus experience a repulsive electrostatic force, which is given by:

$$F_{dipoles} = -\frac{9}{4\pi\epsilon_0} \frac{(\epsilon_0 \epsilon A_{beam})^2}{d^5} \left(V_{bias} + \psi_0 \frac{t_m}{t_i} \right)^2 (z_1 - z_2), \quad (5.1)$$

where d is a distance between beams, A_{beam} is a beam area Lxw , z_1 and z_2 are the out of plane central point displacements, $\psi_0 \approx 1.2V$ is a diode built-in potential, $t_i = 50nm$ is a thickness of an insulating layer and $t_m \approx 78nm$ is the depletion width of the *pin* diode [36].

The electrostatic interaction plays a crucial role in the phenomenon described in chapter 7. The coupling can be described as a simple linear one with a negative coefficient, which can be understood as a spring with negative stiffness constant is attached between the beams providing a repulsive force directly proportional to the difference in displacements. For the geometry of the devices used in the experiment in chapter 7 ($d=400$ nm, $A_{beam}=Lxw=6$ $\mu\text{m} \times 0.5$ μm and $V_{offset} \approx 1.1$ V and 1 nm difference in displacements) the force is ~ 1 pN.

Another coupling mechanism is piezobackaction due to direct piezoelectric effect. When a resonator is in motion, the strain causes a voltage to develop across the depletion region of the resonator, and this voltage in turn affects the other resonator. The inverse piezoelectric effect is used for actuation, while the electric field causes the strain. Historically it was described after the direct effect when the voltage was measured between the electrodes on opposite edges of squeezed quartz crystal [42].

Preliminary calculations show that in most cases the piezobackaction has a negligible effect due to either the large capacitance of the wirebond electrode or the intentional isolation of the resonator's top electrodes.

5.2 STRONG COUPLING MODEL

If two resonators are strongly coupled by an elastic spring between them then the equations of motion include a simple linear term of the form $\zeta(x_1-x_2)$, where ζ is stiffness constant of the spring; x_1 and x_2 are the displacements of the resonator. This term represents the interaction force between the beams. The equation of motion for two resonators, whose resonance frequencies are ω_1 and ω_2 , assuming their masses are the same, is given by:

$$\begin{aligned}\ddot{x}_1 + \frac{\omega_1}{Q_1} \dot{x}_1 + (\omega_1^2 + D)x_1 - Dx_2 &= 0, \\ \ddot{x}_2 + \frac{\omega_2}{Q_2} \dot{x}_2 + (\omega_2^2 + D)x_2 - Dx_1 &= 0.\end{aligned}\tag{5.2}$$

Here $D=\xi/m$ is a reduced coupling coefficient which has units of radians per seconds squared. We assume that the resonators have equal masses. Equation (5.2) is obtained by dividing the regular resonators EOM (2.1) by the mass m . The detailed formalism on how to develop and solve coupled oscillators models is given in most classical mechanics text books (for example in [43]).

In the first approximation the equation of motion for two beams is then expressed in matrix form:

$$M\ddot{\vec{x}} + \Gamma\dot{\vec{x}} + V\vec{x} = F, \tag{5.3}$$

where $\vec{x}=(x_1, x_2)$ is a displacement vector, $F=(F_1(t), F_2(t))$ is a vector of forces exerted on the individual resonators and M, Γ, V are the mass, damping and potential matrices respectively. They are given by:

$$M = \begin{pmatrix} m & 0 \\ 0 & m \end{pmatrix}, \quad \Gamma = \begin{pmatrix} \frac{m\omega_1}{Q_1} & 0 \\ 0 & \frac{m\omega_2}{Q_2} \end{pmatrix}, \quad V = \begin{pmatrix} m\omega_1^2 + \xi & -\xi \\ -\xi & m\omega_2^2 + \xi \end{pmatrix}.\tag{5.4}$$

Duffing nonlinearity and parametric terms are omitted for now. They will be reintroduced later when coupled nonlinear and coupled parametric effects are discussed in detail.

The equation (5.4) is a typical eigenvalue problem. The eigenvectors give the mode shapes and the eigenvalues are the modes' angular frequencies. The solution is conveniently expressed in terms of squared average and squared difference frequencies:

$$\omega_m^2 = \frac{\omega_1^2 + \omega_2^2}{2}, \quad \delta = \frac{\omega_2^2 - \omega_1^2}{2}.\tag{5.5}$$

Then eigenvalues are given by:

$$\begin{aligned}\omega_I^2 &= \omega_m^2 + D - \sqrt{D^2 + \delta^2}, \\ \omega_{II}^2 &= \omega_m^2 + D + \sqrt{D^2 + \delta^2}.\end{aligned}\quad (5.6)$$

The orthogonal and normalized eigenvectors are:

$$\mathbf{e}_I = \frac{1}{N_I} \begin{pmatrix} \delta + \sqrt{\delta^2 + D^2} \\ D \\ 1 \end{pmatrix}, \quad \mathbf{e}_{II} = \frac{1}{N_{II}} \begin{pmatrix} \delta - \sqrt{\delta^2 + D^2} \\ D \\ 1 \end{pmatrix}.\quad (5.7)$$

Expressions (5.6) and (5.7) imply that the two coupled resonators lead to two independent modes. If the resonators are identical $\delta=0$ then the first mode is completely symmetric with both beams vibrating in phase with the same amplitude at the angular frequency $\omega_I=\omega_m$, and the second one is antisymmetric when the resonators motion is out of phase and its frequency is higher $\omega_{II}^2=\omega_m^2+2D$. On the other hand when the beams slightly differ in frequencies the modes are no longer fully symmetric or antisymmetric. In this case the first mode the resonators vibrate roughly in phase although the first beam (lower frequency) has large amplitude, whereas the second mode is mainly an out of phase motion while the second beam has higher amplitude in this case.

The system of equations for modes as two independent resonators in a form similar to (5.3) is obtained via dedagonalization procedure (explained in detail in [43]). The conversion for the matrices in equation (5.4) is given by:

$$x' = \tilde{T}x, \quad M' = \tilde{T}MT, \quad \Gamma' = \tilde{T}\Gamma T, \quad V' = \tilde{T}VT, \quad F' = \tilde{T}F, \quad (5.8)$$

where $T=(\mathbf{e}_I \ \mathbf{e}_{II})$ is a conversion matrix composed of two eigenvectors from (5.7) as a columns, and $\tilde{T}=T^{-1}$ is the reciprocal matrix, which in the case of orthonormal eigenvectors is equal to transposed matrix. The force F and displacement x are vectors, hence the conversion procedure is simpler. Since the eigenvalue problem is supposed to diagonalize potential energy, V' is diagonal.

It turns out that mass matrix M' is also diagonal due to its proportionality to a unity matrix. The damping matrix Γ' has small off-diagonal terms although they are a factor of 60 smaller than the diagonal ones and can thus be ignored.

5.3 STRONG ELASTIC COUPLING THROUGH SUPPORTS

The strongest interaction engineered between doubly clamped beams is a configuration where the resonators share ledges on both sides. The SEM image of two strongly coupled $6\mu\text{m} \times 600\text{nm}$ resonators is shown in figure 5.3(a).

This architecture requires D-NEMS resonators to share both top and bottom electrodes; therefore the second asymmetric mode is heavily suppressed by both actuation and detection mechanisms. Since the laser beam used for the transduction covers both beams, therefore only one resonance peak shown in figure 5.3(b) is observed during the measurements.

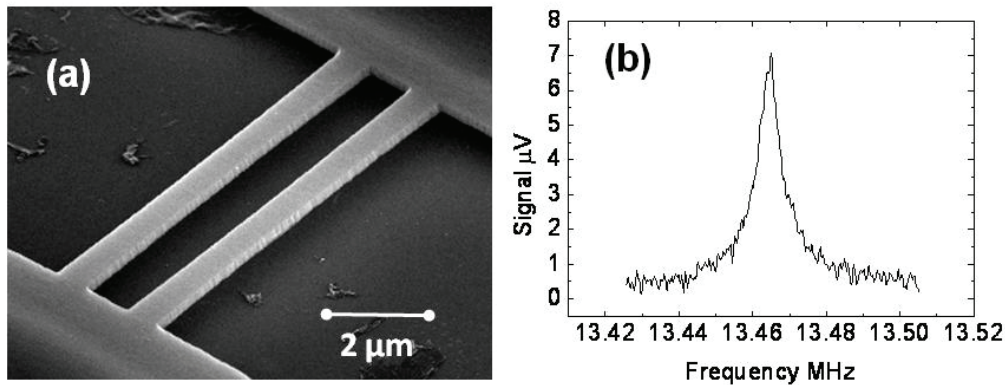


Figure 5.3 (a) SEM image of two strongly coupled nanoresonators. (b) Only one mode is visible, because the second mode turns out to be suppressed by both detection and actuation mechanisms.

In order to better understand the nature of elastic support interaction we performed finite element simulations. The realistic experimental geometry with the two $6\mu\text{m} \times 600\text{nm} \times 200\text{nm}$

beams $0.9\mu\text{m}$ apart is defined. The resonators are chosen to be identical because this is a strong coupling case when $D \gg \delta$. The ledge length is chosen to be $1\mu\text{m}$. A static analysis is used to estimate the strength of the elastic coupling. A large uniform force is applied to the first beam causing it to move by x_1 . As a result the stress propagates through the ledge so that the second beam is affected by the interaction force $\zeta(x_2-x_1)$ and displaces by x_2 . The displacement color map is shown in figure 5.4.

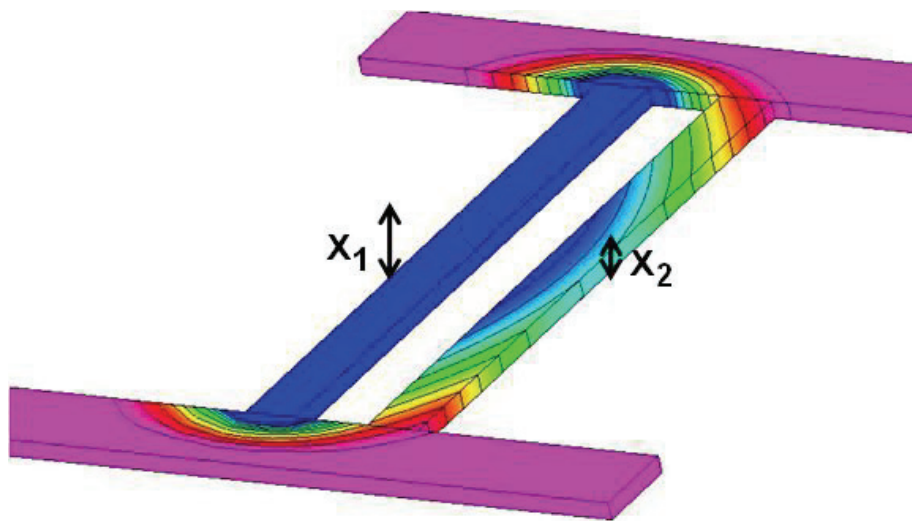


Figure 5.4 Finite element simulations of coupling through ledge. The force applied to one of the beams exerts the interaction force on the other one. Calculated displacements are used to estimate the coupling constant.

The estimated interaction spring constant using this method is $\zeta=1.40\text{ N/m}$, (regular beam stiffness constant is $k=28\text{ N/m}$). In addition, a modal analysis is performed using the same finite element analysis package. Symmetric and antisymmetric modes were found with resonance frequencies of 13.8 and 14.5 MHz respectively. Using equation (5.6) we estimate the coupling constant using this method $\zeta=1.38\text{ N/m}$. The results indicate good agreement, which means finite

element analysis is a proper method to investigate elastic coupling phenomena in mechanical devices.

Modal analysis for three strongly coupled resonators reveals three modes; their shapes are shown in figure 5.5. The first mode is symmetric, and therefore it is expected to be easily detectable in the experiment. On the other hand the second asymmetric mode, with two beams vibrating out of phase while the middle beam rests, is heavily suppressed by both actuation and detection, similar to the simpler two-resonator case. Therefore it is not likely to be detectable in the measurements. The third mode is not fully asymmetric, and therefore we may be able to detect a small resonance peak associated with this mode.

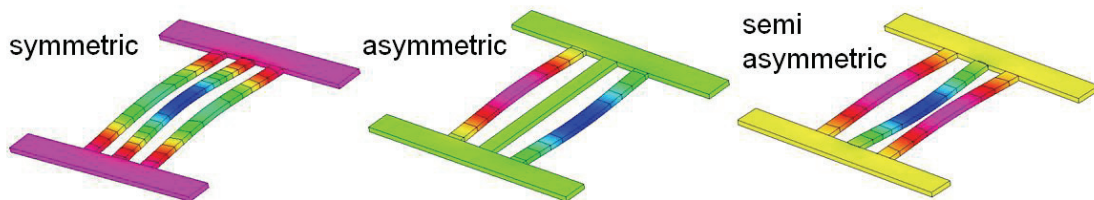


Figure 5.5 Mode shapes of a system of three strongly coupled resonators, calculated by finite element analysis.

Three strongly coupled 6-micron-long beams were fabricated and measured. As was predicted, only two modes are visible, and the first mode is much more evident than the other. Figure 5.6 shows the SEM image of the 3-beam system and its spectral response. The first symmetric mode has to be driven well above the onset of nonlinearity in order to make the third asymmetric mode barely visible.

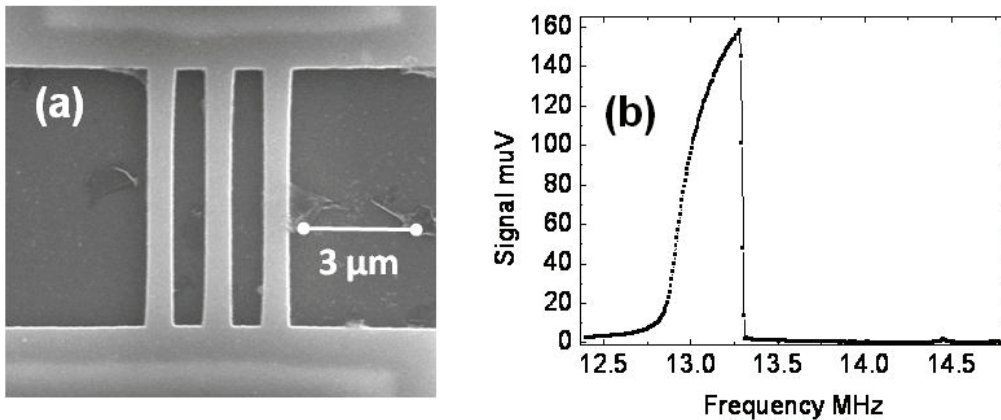


Figure 5.6(a) SEM image of three strongly coupled D-NEMS resonators (b) the spectral response with two modes visible

Piezoelectric actuation and optical detection turn out to be a remarkably powerful method for characterizing the coupled modes of arrays of nanoresonators. A great demonstration of the coupled mode phenomena is the observation of a variety of modes in an even larger number of resonators. To show this we fabricated and analyzed an array of ten nanomechanical resonators. Finite element analysis was employed to calculate the shapes of the ten coupled modes. SEM image and calculated mode shapes are shown in figure 5.7. The result of modal analysis shows a set of ten modes that represent an analog the standing wave patterns with progressively decreasing wavelength.

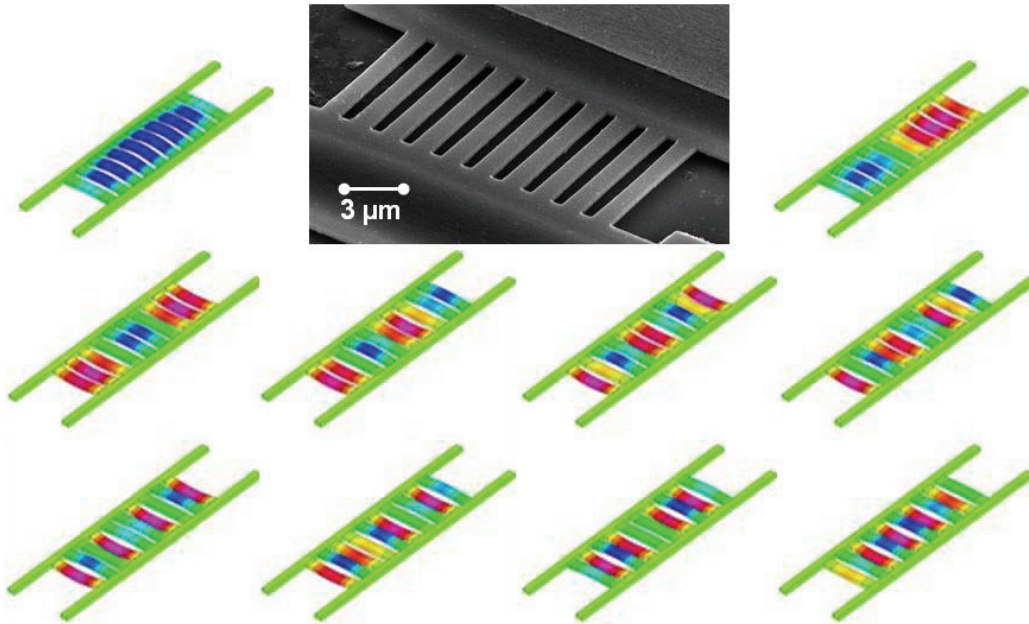


Figure 5.7 An SEM image of ten $5\mu\text{m}$ long resonators and its coupled mode shapes calculated via finite element analysis.

In the measurement setup the laser beam spot size was deliberately increased so that all the resonators are in its area of illumination. The first mode with resonance frequency of around 22 MHz is very easily detectable, but the second mode is suppressed when the first one is optimized. Therefore the laser spot was shifted so that the second mode is at its maximum optical detection efficiency.

After all the optical adjustments, the resonance scan over a wide frequency range was performed. As a result nine out of ten modes in figure 5.7 were observed, the missing mode possibly due to its extreme actuation and detection suppression. The amplitude of the drive was set to a high level so that all the modes are visible as small peaks. Hence the first three peaks are excited to very high amplitude, above the onset of nonlinearity. A wide spectral response is shown in figure 5.8. Each mode's resonance peak was carefully examined and its frequency and quality

factor was measured reducing the drive for over-driven modes in the figure. The result is plotted in the inset in figure 5.8. The resonance frequency predictably steadily increases with the mode number while the quality factor starts at 1530 for the first two modes, then rises as high as 3040 for mode number 7, and then slightly drops for modes eight and nine. This observation is unusual in comparison with previous observations [44], in which the quality factor typically decreases as the mode number is increased

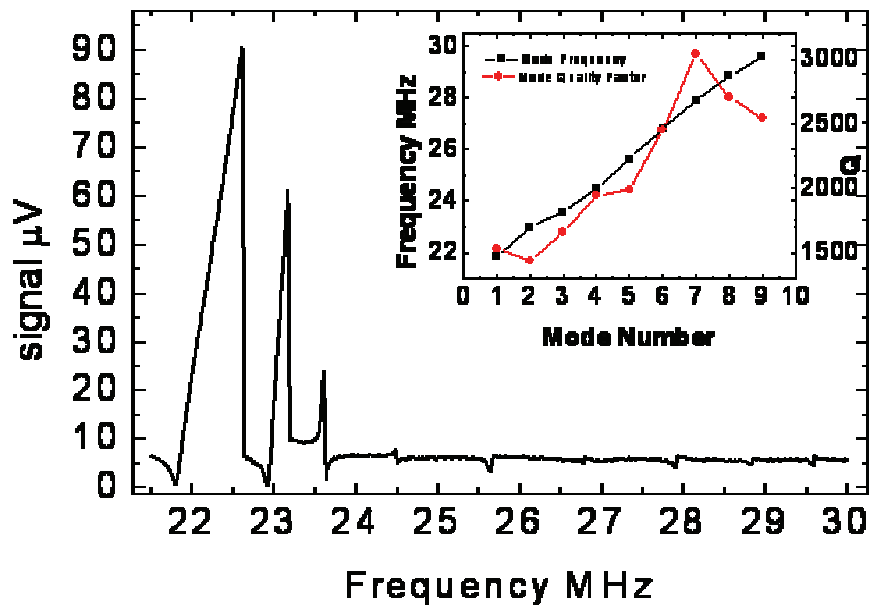


Figure 5.8 The spectral response of the system of ten strongly coupled D-NEMS resonators. Nine out of ten peaks were observed. The inset shows the dependence of resonance peak's frequency and quality factor on mode number.

The observed phenomenon is an excellent demonstration of a well-known tuning-fork effect. In an asymmetric mode, two adjacent beams vibrate out of phase, and therefore the net motion of the

support between them is heavily suppressed, causing only a limited amount of energy to be dissipated as elastic waves into the bulk substrate. As a result the quality factors of asymmetric modes are larger than those for symmetric ones even though their frequencies are also higher. This phenomenon is promising for designing the architecture for arrays of large number of resonators.

5.4 FREQUENCY BRIDGE

This section illustrates an example where a system of coupled nanomechanical resonators is a promising approach to significantly improve frequency resolution, thus providing a path to more reliable sensors with even greater precision.

The mechanical system includes two adjacent resonators with isolated actuation electrodes. This condition allows each beam to be embedded in its own independent phase locked loop for precise frequency measurement. A simple setup shown schematically in figure 5.9 includes two independent phase locked loops where computer controlled identical network analyzers are used as source and phase locked measurement instruments.

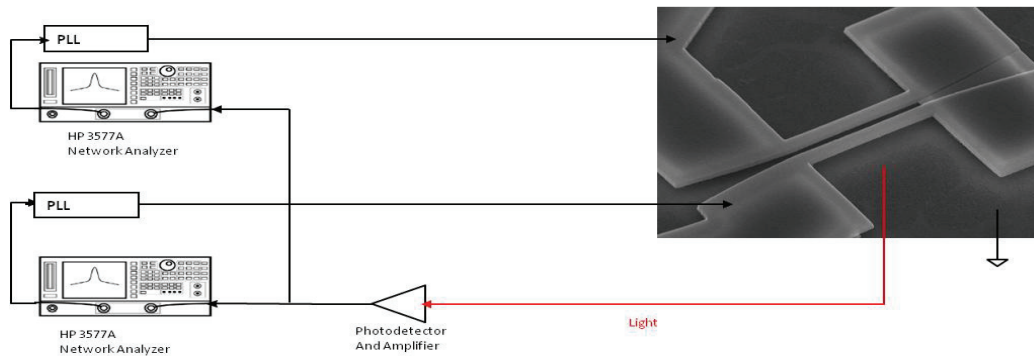


Figure 5.9 The measurement setup for the independent frequency tracking of the two modes of the system of two coupled nanoresonators.

The experiment was performed using two different doubly clamped beam architectures. In the first case the two beams were strongly coupled, with the modes of vibration given by equations (5.6) and (5.7). Nevertheless each mode is more efficiently excited via its corresponding actuation electrode. Although the other mode is weakly excited its frequency is off resonance, and so its effect is negligible. In the second case, the beams did not share the ledge and therefore were only weakly coupled via electrostatic interaction and the common elastic support. The effect of these two coupling mechanisms is opposite in our system, and hence the conditions were chosen to be such that the interaction force between beams vanishes. The physical characteristics of the system are described in detail in the chapter 7.

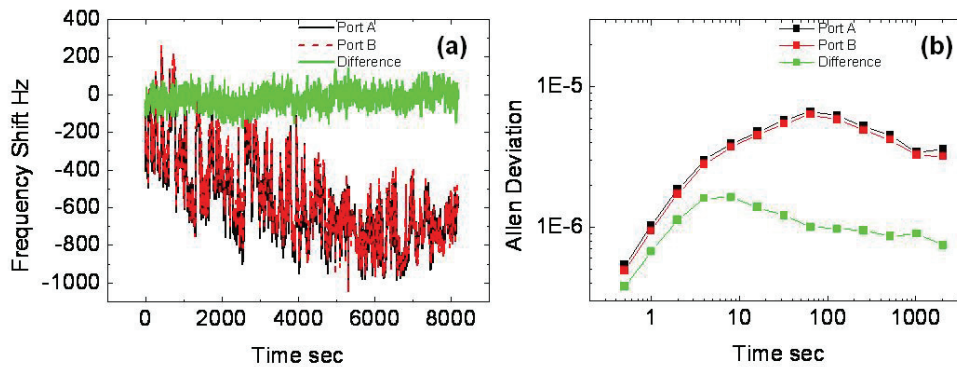


Figure 5.10 (a) Resonance frequency shift traces and their difference is plotted for two coupled nanoresonators. (b) Allan deviation comparison for the frequency traces of the modes and the difference.

The resonance frequency was monitored for more than two hours. For the strongly coupled case the traces from two modes are shown in figure 5.10(a) as red and black curves. Although significant long term frequency drift is observed over this period of time, the frequency shift traces are highly correlated. When the initial resonance frequency is subtracted, the frequency shift plots

tend to follow one another, echoing each other's drift pattern. As a result a remarkable reduction in long term frequency noise is obtained by monitoring the difference between the frequency shifts, shown as a green curve on the plot. The difference plot turns out to be very stable and less noisy. The Allan deviation plots, which are quantitative indicators of frequency stability, for given traces are shown in figure 5.10(b) with the same coloring. A remarkably low value of 5×10^{-7} is demonstrated for long term averaging times of hundreds and thousands of second. This phenomenon is utilized in low noise surface acoustic wave (SAW) sensors [45].

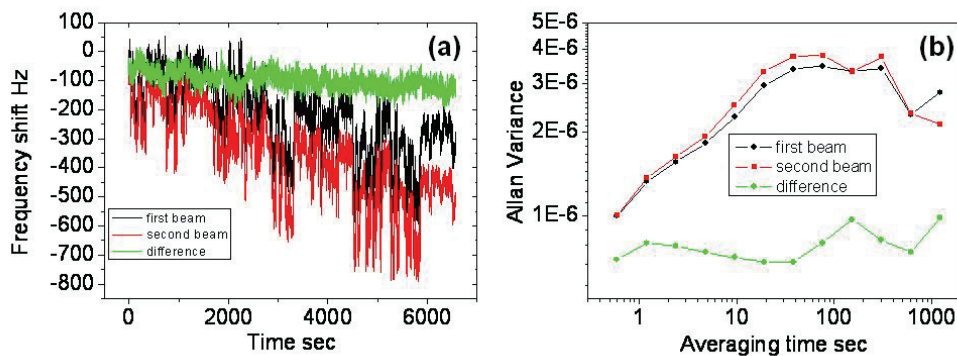


Figure 5.11 (a) Resonance frequency shift traces and their difference is plotted for two uncoupled nanoresonators.(b) Allan deviation comparison for the frequency traces of the modes and the difference

Similar measurements for weakly coupled system are plotted in figure 5.11. The correlation of the long term drift for two independent beams is clearly visible in the plot (a), although the drift of the second beam (red) is evidently larger by a constant factor. This effect is a direct consequence of different temperature susceptibility of two independent beams. Taking this into account, we determine the Allan deviation for the difference signal calculated using different scaling factors for the second beam. As a result we conclude that the optimal scaling factor, which is the ratio of

temperature susceptibilities, is 1.15. The green difference plot and Allan deviation is calculated for these scaled frequency shift values.

The conclusion is that the main causes for long term frequency drift are external. They affect the resonators located on the same chip in similar way. The most important factor, which influences a mechanical resonator operated in vacuum, is ambient temperature. The temperature is a subject to fluctuations as well as drift over a typical time of hours due to variety of factors. Many of the effects are unavoidable in reliable sensor operation, hence employing pairs of devices or using one test device will significantly improve the long term resonance frequency stability. The demonstrated phenomenon is very promising for a wide variety of nanoelectromechanical system applications.

SUMMARY

Systems of coupled resonators are extremely abundant both in artificial mechanisms and in nature. Nevertheless the detailed formalism for straightforward understanding of the underlying physical phenomena does not exist. Partly it is because the system is very complex for simple classification and characterization; partly it is due to different languages various communities use to describe their systems. This chapter provides a crucial step towards understanding the physics of interacting nanomechanical resonators. It starts with a discussion about possible coupling mechanisms present in piezoelectric D-NEMS nanoresonators. Then the vibration mode analysis is performed for strongly coupled beams. The model is experimentally tested with systems of two, three, and ten resonators. Finally a system of frequency bridge is introduced and implemented for both strongly and weakly interacting mechanical devices. The results suggest enormous potential for applications in frequency shift-based sensing.

Chapter 6

COUPLING OF TWO DUFFING RESONATORS

This chapter studies the physical phenomena in the system of two strongly coupled nonlinear resonators. Simple linear interaction results in complex nonlinear terms in the equations of motion of the system. Complicated behavior of the system is studied both theoretically and experimentally. An extraordinary agreement between analytical predictions and measured results is observed even for such complex phenomena as spontaneous state transitions and chaos.

6.1 THEORETICAL ANALYSIS

In section 5.2 in previous chapter the model for two strongly coupled resonators was developed. As a result a recipe for dedagonalization of equation (5.3) was outlined. This procedure results in an analogous equation for the orthogonal modes of resonators, whose shape is given by eigenvectors (5.7), where the potential energy matrix does not have off-diagonal terms. Therefore the system of equations for the modes of vibration is treated as a system of two independent resonators. The damping matrix Γ gains negligibly small off-diagonal terms because the initial terms have very small difference. Duffing nonlinear terms were intentionally omitted from the discussion earlier, because they require special consideration.

The theoretical investigation of a Duffing nonlinear system is typically done using secular perturbation theory technique similar to the one used in chapter 2 to study parametric effects [19]. Hence in order to understand the behavior of two strongly coupled resonators the same method is employed. We start with a system of coupled equations of motion:

$$\begin{aligned} \ddot{x}_1 + \gamma_1 \dot{x}_1 + \omega_1^2 x_1 + \alpha_1 x_1^3 + D(x_1 - x_2) &= g_{D1}(t), \\ \ddot{x}_2 + \gamma_2 \dot{x}_2 + \omega_2^2 x_2 + \alpha_2 x_2^3 + D(x_2 - x_1) &= g_{D2}(t). \end{aligned} \tag{6.1}$$

This is an extended version of the linear equation of motion (2.8), where parametric terms are omitted; the simpler version was given in the previous chapter (equation (5.3)). After introducing the small dimensionless parameter ε we rewrite some parameters in the equation, adding a slower time T

$$T = \varepsilon t, \quad g_{Di} = \varepsilon^{3/2} g_i, \quad \gamma_i = \varepsilon \Gamma_i, \quad i = 1, 2. \quad (6.2)$$

The solution is expressed in the motion of modes given by eigenvectors (5.7). Therefore the expression for the displacement of the beams is de-diagonalized and expanded in ε analogous to equation (2.10):

$$\mathbf{x} = \frac{\varepsilon^{\frac{1}{2}}}{2} (A_I(T) e^{i\omega_I t} \mathbf{e}_I + A_{II}(T) e^{i\omega_{II} t} \mathbf{e}_{II} + c.c.) + \varepsilon^{\frac{3}{2}} \mathbf{x}^{(I)}(t) + \dots; \quad (6.3)$$

bold font indicates two-dimensional vectors here, the components of \mathbf{x} are the displacements of the central point of the beam, \mathbf{e}_I and \mathbf{e}_{II} are the eigenvectors given by (5.7) and $\mathbf{x}^{(I)}$ is a vector of next order corrections. The amplitudes A_I and A_{II} are the scaled equivalent displacements of the modes of vibration. The factor of $\frac{1}{2}$ is introduced because only the real component is a physical displacement. For future simplicity we define the notations for the components of eigenvectors as $\mathbf{e}_I = (e_{I,1}; e_{I,2})$ and $\mathbf{e}_{II} = (e_{II,1}; e_{II,2})$.

The time derivatives of the displacements above have a form similar to equation (2.11), while the cubic terms are more complicated. In the expansion we only keep the terms resonant with either of the modes.

$$\begin{aligned} x_i^3 = & \frac{\varepsilon^{\frac{3}{2}}}{8} \left\{ e^{i\omega_I t} \left[3(e_{I,i})^3 |A_I|^2 A_I + 6e_{I,i} (e_{II,i})^2 |A_{II}|^2 A_I \right] \right. \\ & \left. + e^{i\omega_{II} t} \left[3(e_{II,i})^3 |A_{II}|^2 A_{II} + 6(e_{I,i})^2 e_{II,i} |A_I|^2 A_{II} \right] + c.c. + nonresonant terms \right\} + \dots \end{aligned} \quad (6.4)$$

The forces g_{Di} in equation (6.1) are exerted upon individual beams; experimentally we can apply these forces in a variety of ways. Considering general the case when each beam can be actuated with both resonance frequencies simultaneously, the scaled forces are given by:

$$\begin{aligned} g_1(t) &= \frac{1}{2} [g_{1,I}(T)e^{i\omega_I t} + g_{1,II}(T)e^{i\omega_{II} t} + c.c.], \\ g_2(t) &= \frac{1}{2} [g_{2,I}(T)e^{i\omega_I t} + g_{2,II}(T)e^{i\omega_{II} t} + c.c.], \end{aligned} \quad (6.5)$$

where $g_{i,I}(T)$ indicates that it is a part of the force exerted upon the i 's beam near the resonance frequency of mode I (first mode) at frequency $\omega_I + \varepsilon\Omega_I$. It then it has the form $g_{i,I}(T) = |g_{i,I}(T)|e^{i\Omega_I T}$.

After substitution of the last three expressions into equation (6.1) $O(\varepsilon^{1/2})$ terms cancel, because they are linear resonator terms. Hence keeping only $O(\varepsilon^{3/2})$ terms, the equation of motion assumes the form:

$$\begin{aligned} \begin{bmatrix} -\frac{d^2}{dt^2} - \omega_1^2 - D & D \\ D & -\frac{d^2}{dt^2} - \omega_2^2 - D \end{bmatrix} \mathbf{x}^{(1)} &= e^{i\omega_I t} \left\{ i\omega_I A_I' \begin{pmatrix} e_{I,1} \\ e_{I,2} \end{pmatrix} + \frac{i\omega_I}{2} A_I \begin{pmatrix} \Gamma_1 e_{I,1} \\ \Gamma_2 e_{I,2} \end{pmatrix} \right. \\ &+ \frac{3}{8} |A_I|^2 A_I \begin{pmatrix} \alpha_1 (e_{I,1})^3 \\ \alpha_2 (e_{I,2})^3 \end{pmatrix} + \frac{3}{4} |A_{II}|^2 A_I \begin{pmatrix} \alpha_1 e_{I,1} (e_{II,1})^2 \\ \alpha_2 e_{I,1} (e_{II,2})^2 \end{pmatrix} - \frac{1}{2} \begin{pmatrix} g_{1,I} \\ g_{2,I} \end{pmatrix} + c.c. \left. \right\} \\ &+ e^{i\omega_{II} t} \{ \dots \} + \text{nonresonant terms}. \end{aligned} \quad (6.6)$$

The $e^{i\omega_{II} t}$ terms are obtained via obvious interchange of indices.

On the left-hand side of equation (6.6) there is a system of two independent resonators with zero internal damping, therefore on the right-hand side terms varying at ω_I and ω_{II} have to be orthogonal to eigenvectors \mathbf{e}_I , and \mathbf{e}_{II} respectively. This requirement gives equations of motion for the amplitudes of the modes A_I and A_{II} :

$$\begin{aligned}
i\omega_I A_I' + \frac{i\omega_I}{2} [\Gamma_1 (e_{I,1})^2 + \Gamma_2 (e_{I,2})^2] A_I + \frac{3}{8} [\alpha_1 (e_{I,1})^4 + \alpha_2 (e_{I,2})^4] |A_I|^2 A_I \\
+ \frac{3}{4} [\alpha_1 (e_{I,1})^2 (e_{II,1})^2 + \alpha_2 (e_{I,2})^2 (e_{II,2})^2] |A_{II}|^2 A_I = \frac{1}{2} [g_{1,I} e_{I,1} + g_{2,I} e_{I,2}].
\end{aligned} \tag{6.7}$$

And for the second mode,

$$\begin{aligned}
i\omega_{II} A_{II}' + \frac{i\omega_{II}}{2} [\Gamma_1 (e_{II,1})^2 + \Gamma_2 (e_{II,2})^2] A_{II} + \frac{3}{8} [\alpha_1 (e_{II,1})^4 + \alpha_2 (e_{II,2})^4] |A_{II}|^2 A_{II} \\
+ \frac{3}{4} [\alpha_1 (e_{I,1})^2 (e_{II,1})^2 + \alpha_2 (e_{I,2})^2 (e_{II,2})^2] |A_I|^2 A_{II} = \frac{1}{2} [g_{1,II} e_{II,1} + g_{2,II} e_{II,2}].
\end{aligned} \tag{6.8}$$

These equations are of the form:

$$\begin{aligned}
i\omega_I \frac{dA_I}{dT} + i\omega_I \Gamma_I A_I + \alpha_I |A_I|^2 A_I + \beta_I |A_{II}|^2 A_I = G_I(T), \\
i\omega_{II} \frac{dA_{II}}{dT} + i\omega_{II} \Gamma_{II} A_{II} + \alpha_{II} |A_{II}|^2 A_{II} + \beta_{II} |A_I|^2 A_{II} = G_{II}(T).
\end{aligned} \tag{6.9}$$

Where

$$\begin{aligned}
\Gamma_{[I]} &= \frac{1}{2} [\Gamma_1 (e_{[I],1})^2 + \Gamma_2 (e_{[I],2})^2], \\
\alpha_{[I]} &= \frac{3}{8} [\alpha_1 (e_{[I],1})^4 + \alpha_2 (e_{[I],2})^4], \\
\beta_{[I]} &= \frac{3}{4} [\alpha_1 (e_{I,1})^2 (e_{II,1})^2 + \alpha_2 (e_{I,2})^2 (e_{II,2})^2], \\
G_{[I]} &= \frac{1}{2} [g_{1,[I]} e_{[I],1} + g_{2,[I]} e_{[I],2}],
\end{aligned} \tag{6.10}$$

where indices enclosed in square brackets $\{[I]=I, II\}$ indicate that the equation is valid for both the first I and the second II mode of vibration.

When the modes are driven near their corresponding resonances with frequency shifts $\Omega_{[I]}$, so that $G_{[I]}(T) = |G_{[I]}| e^{i\Omega_{[I]}T}$, the solution for the two equations are:

$$\begin{aligned}
|A_I|^2 &= \frac{|G_I|^2}{\left(\Omega_I - \alpha_I |A_I|^2 - \beta_I |A_{II}|^2\right)^2 + \Gamma_I^2}, \\
|A_{II}|^2 &= \frac{|G_{II}|^2}{\left(\Omega_{II} - \alpha_{II} |A_{II}|^2 - \beta_{II} |A_I|^2\right)^2 + \Gamma_{II}^2}.
\end{aligned} \tag{6.11}$$

This formalism describes a wide variety of physical phenomena observed in strongly coupled Duffing resonators. The numerical solutions of the system of equations (6.9) were obtained by a computer program written in Mathematica. The predictions of the will be compared to the experimental observations.

6.2 COUPLING PARAMETERS OF THE SYSTEM

As an example consider two strongly coupled nanomechanical resonators that share a mechanical ledge and are accessible individually. In order to achieve these characteristics the shared elastic support is partially etched down to the insulating layer. An argon ion milling etching recipe provided remarkable control and uniformity, so that it is easy to achieve good insulation and strong coupling simultaneously. The system of two nanoresonators is shown in figure 6.1. The beams dimensions are $L \times w = 6\mu\text{m} \times 700\text{nm}$, the distance between the beams is 400nm and ledge width is 700nm.

Since the optical interferometric transduction setup has a laser beam spot size that covers both doubly clamped beams, the measurements yield two resonance peaks, and there is not enough information to distinguish the motion of the resonators separately. Therefore the model described is extremely helpful for reliable differentiation of the motion of the two individual beams.

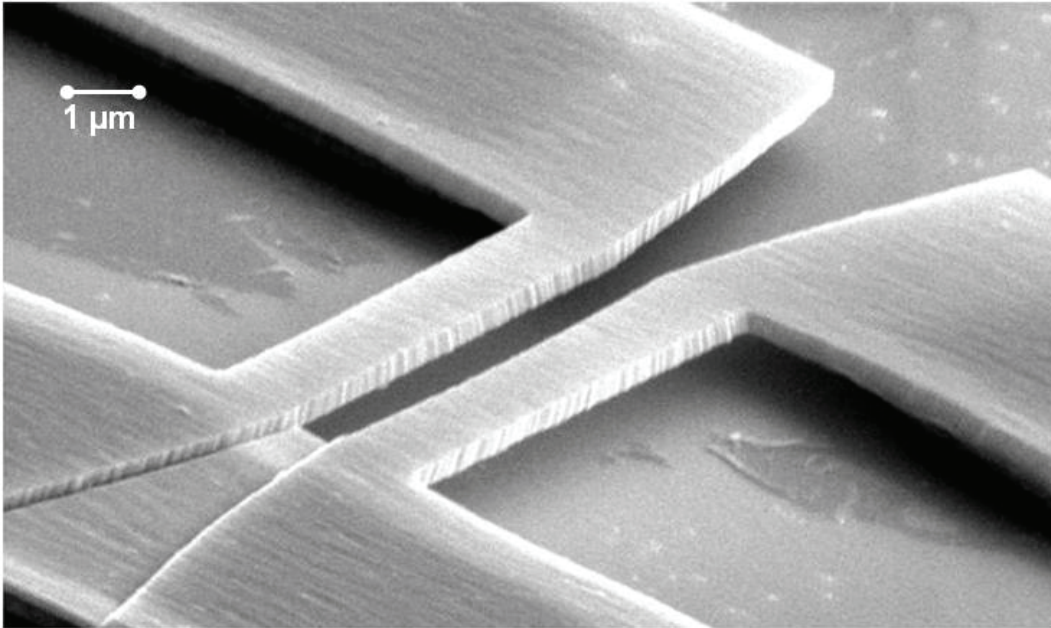


Figure 6.1 Two strongly coupled D-NEMS doubly clamped beams, that share the ledge etched to an insulating layer to provide individual electrical connections.

The excitation voltage, applied between top and bottom electrodes of the D-NEMS nanoresonators exerts forces upon the individual beams. However the behavior of the system is equivalent to the behavior of two independent resonators, which are the vibration modes calculated in the section 5.2 of the previous chapter. Therefore the vector of forces from expression (5.4) has to be converted into effective generalized forces for the modes: the transformation is given on the right-hand sides of equations (6.7) and (6.8) (with the help of equation (6.5)).

Consider a simple case when both beams are driven with the same frequency $F=(F_1\cos(\omega_D t), F_2\cos(\omega_D t))$. Using the expression for the eigenvectors (5.7) we rewrite equations (6.5) for the generalized effective forces exerted upon the modes:

$$\begin{aligned}
F_I &= e_{I,1}F_1 + e_{I,2}F_2, \\
F_{II} &= e_{II,1}F_1 + e_{II,2}F_2.
\end{aligned} \tag{6.12}$$

Here the mode forces are calculated in terms of beam forces. On the other hand the beams motion is expressed in terms of modes motion according to equation (6.3). Therefore according to Hooke's law the amplitudes of beams motion are given by:

$$\begin{aligned}
x_1 &= e_{I,1}x_I + e_{II,1}x_{II} = e_{I,1} \frac{F_I \cos(\omega_D t)}{m\omega_I^2} \Lambda(\omega_D) \Big|_{\omega_D=\omega_I} + e_{II,1} \frac{F_{II} \cos(\omega_D t)}{m\omega_{II}^2} \Lambda(\omega_D) \Big|_{\omega_D=\omega_{II}}, \\
x_2 &= e_{I,2}x_I + e_{II,2}x_{II} = e_{I,2} \frac{F_I \cos(\omega_D t)}{m\omega_I^2} \Lambda(\omega_D) \Big|_{\omega_D=\omega_I} + e_{II,2} \frac{F_{II} \cos(\omega_D t)}{m\omega_{II}^2} \Lambda(\omega_D) \Big|_{\omega_D=\omega_{II}},
\end{aligned} \tag{6.13}$$

where the first mode is driven near its resonance frequency at ω_I and the second one at ω_{II} . and $\Lambda(\omega_D)$ is the Lorentz-type spectral-response function abbreviated for convenience (it is similar for all the peaks). As a result the first terms proportional to F_I in each equation contribute to the first mode while the terms proportional to F_{II} contribute to the second.

The voltages can be applied in a variety of ways. The ratios of the amplitudes of the modes when the beams are driven in phase $F_I=F_2=F_0$ (through a 0° power splitter) and out of phase $F_I=-F_2=-F_0$ (through a 180° power splitter) provide enough information to determine all the coupling parameters, because among the among four seemingly independent quantities ($e_{I,1}$; $e_{I,2}$) and ($e_{II,1}$; $e_{II,2}$) there is only one free parameter $e=e_{I,1}$ due to vectors' orthonormality.

$$e_{I,1} = e, \quad e_{I,2} = \sqrt{1-e^2}, \quad e_{II,1} = -\sqrt{1-e^2}, \quad e_{II,2} = e. \tag{6.14}$$

If the optical efficiencies for the two beams are defined as 1 for the first and η for the second beam, then the ratios of the heights of the two resonances when the beams are excited in and out phase are given by:

$$\frac{A_I}{A_{II}} \Big|_{0^\circ} = \frac{e_{I,1} + e_{I,2}}{e_{II,1} + e_{II,2}} \frac{e_{I,1} + \eta e_{I,2}}{e_{II,1} + \eta e_{II,2}},$$

$$\frac{A_I}{A_{II}} \Big|_{180^\circ} = \frac{e_{I,1} - e_{I,2}}{e_{II,1} - e_{II,2}} \frac{e_{I,1} + \eta e_{I,2}}{e_{II,1} + \eta e_{II,2}}.$$
(6.15)

The experimental plots for these two configurations are shown in figure 6.2. The real component of the amplitude, plotted in orange, indicates that in the first case for in-phase drive the amplitudes are of the same sign, while when driven out of phase the signs are different, as predicted by equation (6.15), where negative ratio means opposite signs and positive the same signs. After measuring the corresponding ratios the system of equations (6.15) is numerically solved yielding the values for the coupled eigenvector parameter e and the optical efficiency η .

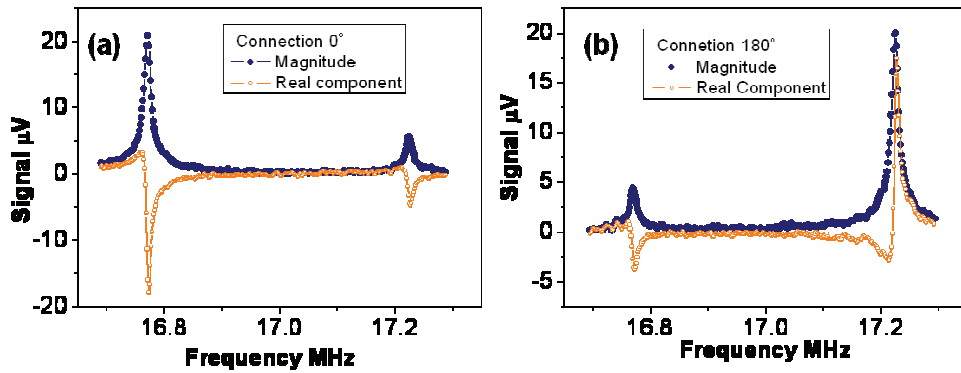


Figure 6.2 The spectral responses of the two modes of the system of two strongly coupled D-NEMS doubly clamped beams, when the resonators are driven in phase (a) and out of phase (b).

For the experimentally determined values $A_I/A_{II}|_{0^\circ}=3.73$ and $A_I/A_{II}|_{180^\circ}=0.218$ measured for the device shown in figure 6.1 the model parameters are $e=0.854$ and $\eta=5.3$. The mode frequencies are $\omega/2\pi=16.79$ MHz, $\omega/2\pi=17.25$ MHz, and therefore the coupling strength expressed in the

units of frequency is $D^{1/2}/2\pi=2.63$ MHz. This value corresponds to the stiffness constant of the elastic support of $\zeta=1.22$ N/m, which is comparable to the coupling strength of the ledges on both ends described in the previous chapter.

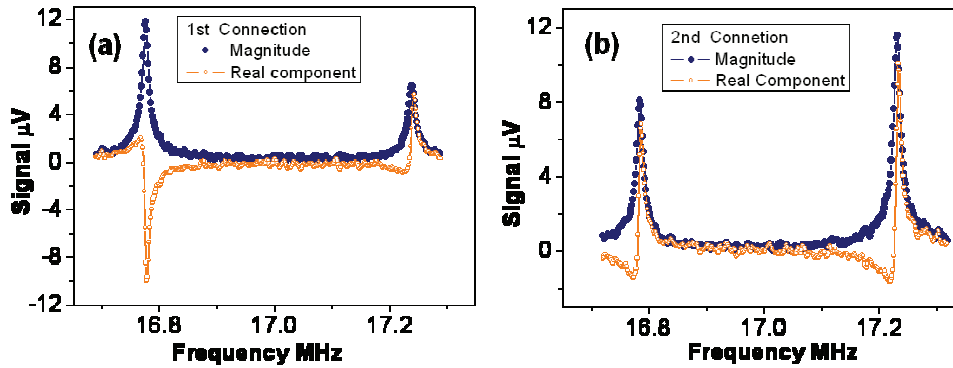


Figure 6.3 The spectral responses for the two modes of the system of two strongly coupled D-NEMS doubly clamped beams, when the excitation voltage is applied first (a) and the second (b) beam's actuation electrode.

The frequencies of the individual resonators are determined from the equations (5.5) and (5.6); their values are $\omega_1/2\pi=16.71$ MHz and $\omega_2/2\pi=16.92$ MHz. The resonance frequency separation of 200 kHz is a reasonable fabrication uncertainty. The eigenvectors are $(0.854; 0.52)$ and $(-0.52; 0.854)$. Using these deduced parameters we predict the ratios of the amplitudes when each beam is excited while the other one stays open. For the first beam ($F_1=F_0$ and $F_2=0$) the predicted ratio is $A_I/A_{II}|_{1st}=1.48$ while the measured is $A_I/A_{II}|_{1st}=1.81$, and for the second beam ($F_1=0$ and $F_2=F_0$) the ratios are even closer: the predicted $A_I/A_{II}|_{2nd}=0.55$ and the measured $A_I/A_{II}|_{2nd}=0.61$. The spectral responses of the last two configurations are shown in figure 6.3.

In addition to this sample, two more were fabricated with similar geometry, and their coupling parameters were reliably determined using the described method. The parameters of the samples are given in table 6.1.

Device #	f_I, f_{II} MHz	Q_I, Q_{II}	$e, \sqrt{1-e^2}$	$\sqrt{D}/2\pi$ MHz
1	16.79, 17.25	2100, 2020	0.854, 0.521	2.63
2	14.69, 15.51	1480, 1530	0.740, 0.672	3.49
3	17.37, 17.64	1620, 1720	0.972, 0.233	1.46

Table 6.1 The parameters of the three coupled devices used in the experiments

The experimentally determined values are used as input parameters to the computer program we developed for the numerical solution of the EOM (6.9). In order to investigate the coupling Duffing phenomena, two beams are connected to two different sources, so that both modes are actuated simultaneously. As a result the system of equations has four free input parameters: the first beam drive amplitude and frequency and the second beam drive amplitude and frequency. The monitored output parameters are the first and the second beam's mechanical motion amplitudes and phases.

6.3 NONDEMOLITION MEASUREMENTS AND LINEARIZATION

Mapping the response in four-dimensional space is not only challenging but also ambiguous, because even though the system of equations (6.9) appears simple, the final vibration state depends on the path the input variables were changed. Multiple solutions exist in large regions of input parameter space. The program we developed solves the time dependent equations (6.9), although some insight on the behavior of the system can be made analyzing equations (6.11). They are the spectral responses of the two coupled resonators similar to equation (2.3) with added levels of

complexity. After rescaling to regular experimental parameters the system of equation assumes the form

$$\begin{aligned} |x_I|^2 &= \left(\frac{F_I Q}{m \omega_I^2} \right)^2 \frac{\omega_I^2}{Q^2 \left(\omega_{DI} - \omega_I - \alpha_I |x_I|^2 - \beta_I |x_{II}|^2 \right)^2 + \omega_I^2}, \\ |x_{II}|^2 &= \left(\frac{F_{II} Q}{m \omega_{II}^2} \right)^2 \frac{\omega_{II}^2}{Q^2 \left(\omega_{DII} - \omega_{II} - \alpha_{II} |x_{II}|^2 - \beta_{II} |x_I|^2 \right)^2 + \omega_{II}^2}. \end{aligned} \quad (6.16)$$

These expressions represent regular Duffing curves if terms proportional to β_{II} are neglected ($\beta_{II}=0$) [19]. The first immediate observation, assuming nontrivial β_{II} , is obvious after simple analysis of this system of equations: when the first mode is driven in the linear regime its resonance frequency is tuned proportionally to the square of the amplitude of the second mode. Indeed at low excitation levels its own nonlinear term $\alpha_I |x_I|^2$ is negligible, while $\beta_I |x_{II}|^2$ considerably alters the frequency. Since the coefficient β_I is positive the tuning is in upward direction. The frequency tuning due to coupled Duffing resonator excitation is shown in figure 6.4. The plot shows the results of the measurements for the first sample in table 6.1, all the strong coupled devices exhibit similar behavior.

The resonance curves in plot (a) are the network analyzer scans of the left peak while the frequency of the drive of the second peak is increased along the blue arrow. The amplitude of the second peak follows the regular Duffing curve since the driving level of the first mode is small, and so at 17.39 MHz the amplitude of second mode vibration drops, as shown by red arrow, and the first mode resonance frequency drops, approximately to its initial value. The inset in plot (b) shows the dependence of the frequency shift on the displacement amplitude of the second mode. The red curve shows the theoretical parabolic curve from equation (6.16). The experimental frequency tuning is of the same magnitude as theoretically predicted, although some deviations are

visible. They are probably consequence of next-order nonlinearities as well as the deviations from the simplest approximation, equations (6.16).

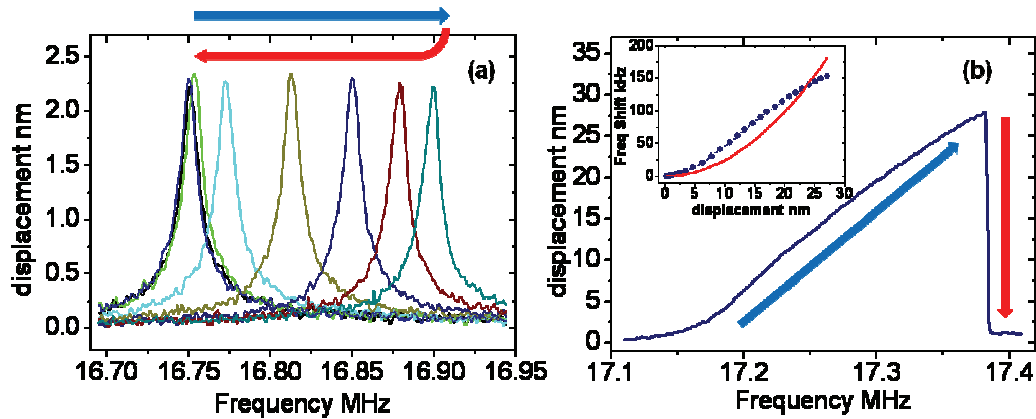


Figure 6.4 Tuning of the first mode by strong nonlinear drive of the coupled second mode. (a) The resonance frequency of the left peak increases as the amplitude of the second peak grows along the blue arrow (b). Then the frequency drops with the amplitude of the second peak, shown by red arrow. The inset shows the dependence of the frequency shift on the amplitude of the second peak.

The important conclusion drawn from this phenomenon is that the presence of two coupled Duffing resonators provides an opportunity to measure the squared displacement of one beam by monitoring the frequency of the other one. This is very promising for quantum nondemolition measurement [46, 47, 48]. A huge effort is being spent on detection of quantum phenomena in macroscopic objects such as nanoelectromechanical systems [6, 49]. Direct measurement of the amplitude of mechanical motion perturbs the system because the displacement operator does not commute with the Hamiltonian of the simple harmonic oscillator. On the other hand the square of

the displacement does commute with Hamiltonian, and therefore measurement without altering the system's quantum state is possible.

If the actuation level of the first mode is further increased, then not only is the resonance frequency tuned, but also the effective nonlinear coefficient α_I is decreased. We assume the effect of the first mode on the second mode is small, when the second beam is driven at much higher level than the first one, even if both modes are driven above the onset of nonlinearity. Hence the second mode squared amplitude S_{II} (here we define $S_{II} = |A_{II}|^2$) is a sum of unperturbed motion $S_{II}^{(0)}$ at the absence of first mode, and the correction due to nonzero A_I :

$$S_{II} \cong S_{II}^{(0)} + \chi_{II,I} S_I + \dots \quad (6.17)$$

where the newly defined parameter $\chi_{II,I} = \partial S_{II} / \partial S_I |_{S_I=0}$ is a susceptibility that corresponds to change in A_{II} due to A_I . $S_{II}^{(0)}$ is the solution for the equation of motion in the absence of the first mode:

$$S_{II}^{(0)} = \frac{|G_{II}|^2}{(\Omega_{II} - \alpha_{II} S_{II}^{(0)})^2 + \Gamma_{II}^2}. \quad (6.18)$$

The expression for susceptibility is calculated from the equation (6.11) via partial differentiation:

$$\chi_{II,I} = -\beta_{II} \frac{\partial S_{II}^{(0)}}{\partial \Omega_{II}}. \quad (6.19)$$

As a result the susceptibility is $-\beta_{II}$ multiplied by the slope of the regular Duffing spectral response curve. Therefore the modified Duffing response of the first mode assumes the form:

$$S_I = \frac{|G_I|^2}{(\Omega_I - \beta_I S_{II}^{(0)} - \alpha_{I,eff} S_I)^2 + \Gamma_I^2}. \quad (6.20)$$

Here we introduced effective nonlinear coefficient $\alpha_{I,eff}$:

$$\alpha_{I,eff} = \alpha_I + \beta_I \chi_{II,I} \quad (6.21)$$

Since the sign of susceptibility is negative in most of the parameter space, the effective Duffing coefficient is decreased. The typical dependence of $\chi_{II,I}$ on the drive frequency of the second mode for the coupling parameters device #1 from Table 6.1 and force at 3.9 times the onset of nonlinearity $F_{II}=3.9F_{CII}$ is shown in figure 6.5(a).

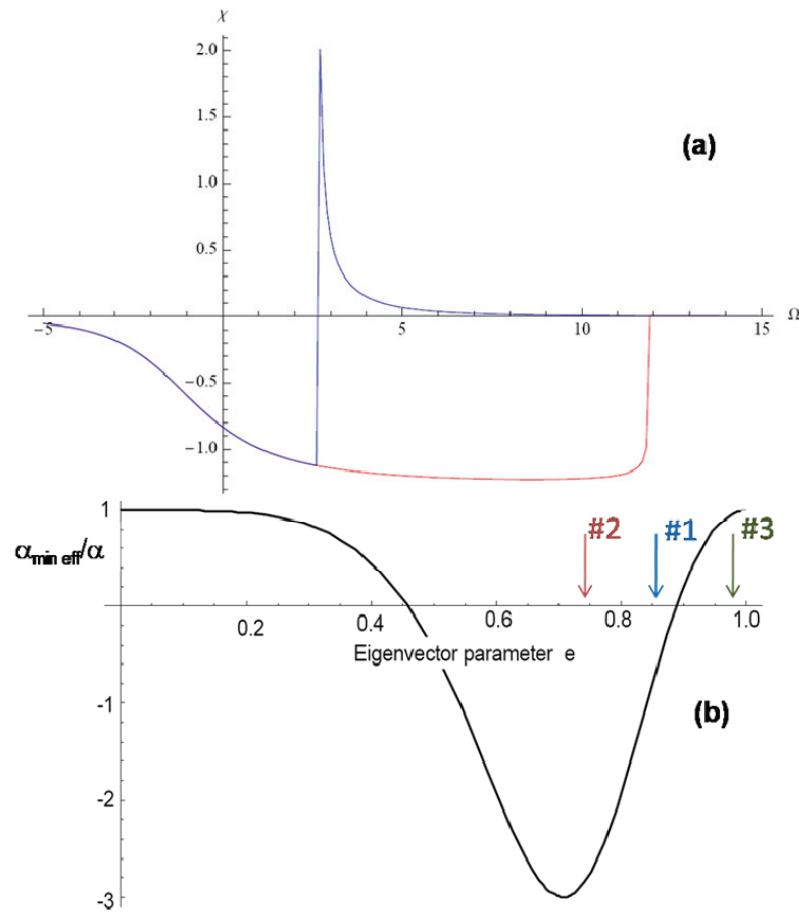


Figure 6.5 (a) Behavior of the susceptibility $\chi_{I,II}$ over a frequency sweep for the coupling parameters of the first device. The red curve is a sweep up and blue a sweep down. (b) Minimum value of the effective Duffing coefficient obtainable with given coupling parameters. The fabricated devices from table 6.1 are shown with arrows.

On the sweep up (red curve) the slope of the Duffing curve is always positive therefore the susceptibility decreases until it saturates at a finite negative value. When the Duffing slope reaches saturation the nonlinear coefficient is at its minimum value, which is given by:

$$\alpha_{I,eff \min} = \alpha_I \left(1 - \frac{\beta_I \beta_{II}}{\alpha_I \alpha_{II}} \right). \quad (6.22)$$

The term in the brackets is fixed for given coupling parameters, hence for the fabricated device. The dependence of this term on eigenvector parameter e is shown in figure 6.5(b). Since the vectors $(e, \sqrt{1-e^2})$ and $(\sqrt{1-e^2}, e)$ are equivalent, the maximum coupling is achieved when $e = \sqrt{1-e^2}$ at $e = 1/\sqrt{2} = 0.707$. As a result the plot is symmetric relative to the line $e = 0.707$. On the sweep down the slope is initially negative, which causes the Duffing coefficient to increase before the solution jumps to its upper state.

If the coupling is strong enough so that the larger eigenvector parameter e is smaller than 0.89, then the minimum value of the Duffing coefficient is negative. In this case the resonance curve tilts to the left, as opposed to the usual case when the peak leans to the right. It also means that the nonlinear coefficient vanishes for a particular region in the input force and frequency of the second mode. The first two samples in Table 6.1 are strongly coupled so that the described behavior can be observed experimentally, while the coupling of the third device is not sufficient to observe significant nonlinearity tuning.

Figure 6.6 shows the theoretical calculations as well as corresponding experimental measurements for the described behavior. A network analyzer is used to monitor the spectral response of the first mode while a separate function generator is driving the second mode. The top eight plots show the theoretical calculation of the evolution of the shape of the resonance peak

while the frequency of the second mode drive is increased, in similar way as in the previous measurements, while bottom eight plots are the corresponding experimental measurements.

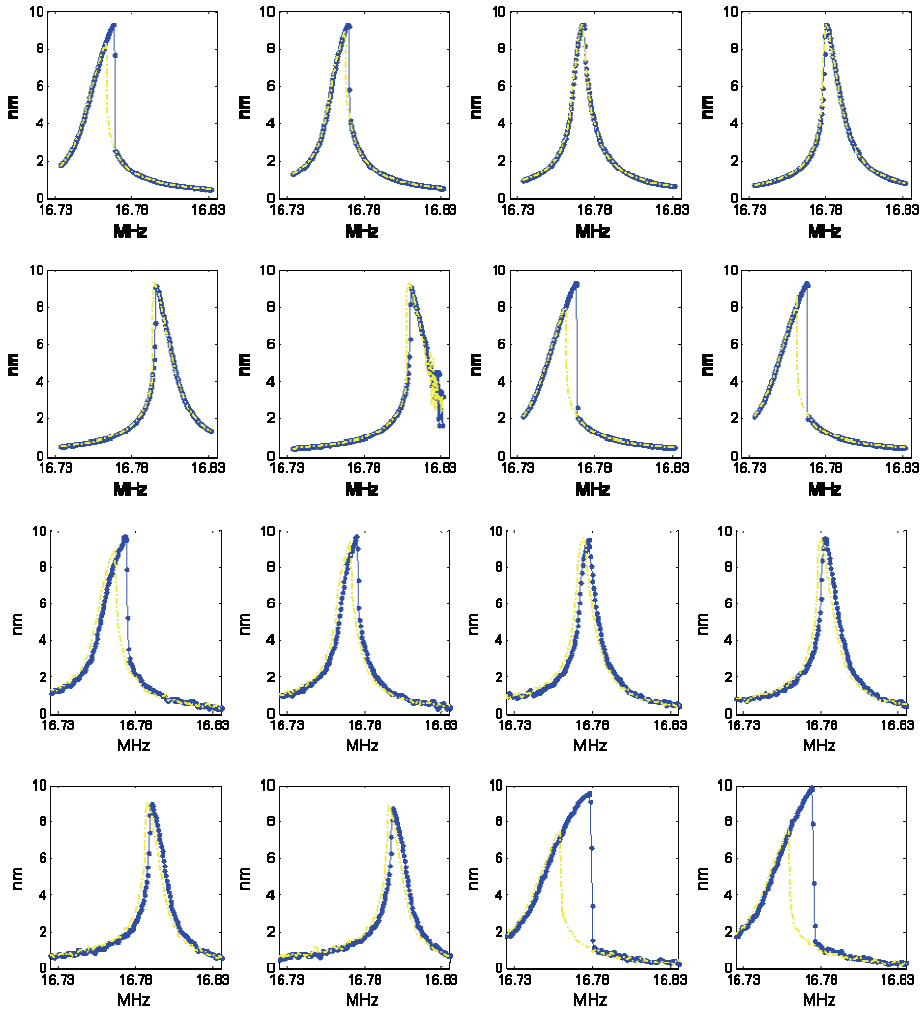


Figure 6.6 Top eight plots show the theoretical calculation of the evolution of the shape of the first mode resonance peak driven above nonlinearity as the frequency of the second mode is swept up. Bottom eight plots are corresponding experimental measurements. The Duffing coefficient flips the sign as the sweep progresses. Blue and yellow curves are up and down sweeps respectively.

At the beginning of the sweep the amplitude of the second mode is low, and therefore the first mode spectral response has the regular nonlinear Duffing shape. As A_{II} increases the first mode resonance frequency is tuned upward and the peak shape is less nonlinear. Then the peak assumes a form very close to a regular Lorentzian with no nonlinearities, and afterward the sign of effective Duffing coefficient becomes negative, causing the spectral response peak to lean to the left in contrast to usual bending to the right. At even higher second mode amplitudes the peak shape stays the same while its position shifts upward until the Duffing resonator switches to a lower state causing the peak shape and position to jump back to its initial state. The theoretical predictions and experimental measurements agree both qualitatively and quantitatively to a high level of precision.

6.4 SPECTRAL RESPONSES

If the drive level of the first mode is increased to an extent comparable to the one of the second mode, then all sorts of different effects are predicted and measured. In addition to such simple effects as linearization and frequency tuning, spontaneous transitions from the lower to the upper state and back occur as the input parameters are swept. As a result the spectral responses acquire peculiar nontrivial shapes. Nevertheless the theoretical analysis is able to make predictions about most of the phenomena to a great precision. Figure 6.7 shows an example analogous to previous plot but when both modes are driven at approximately four times the onset of nonlinearity. The top eight plots are the theoretical simulations and bottom ones are the experimental measurements.

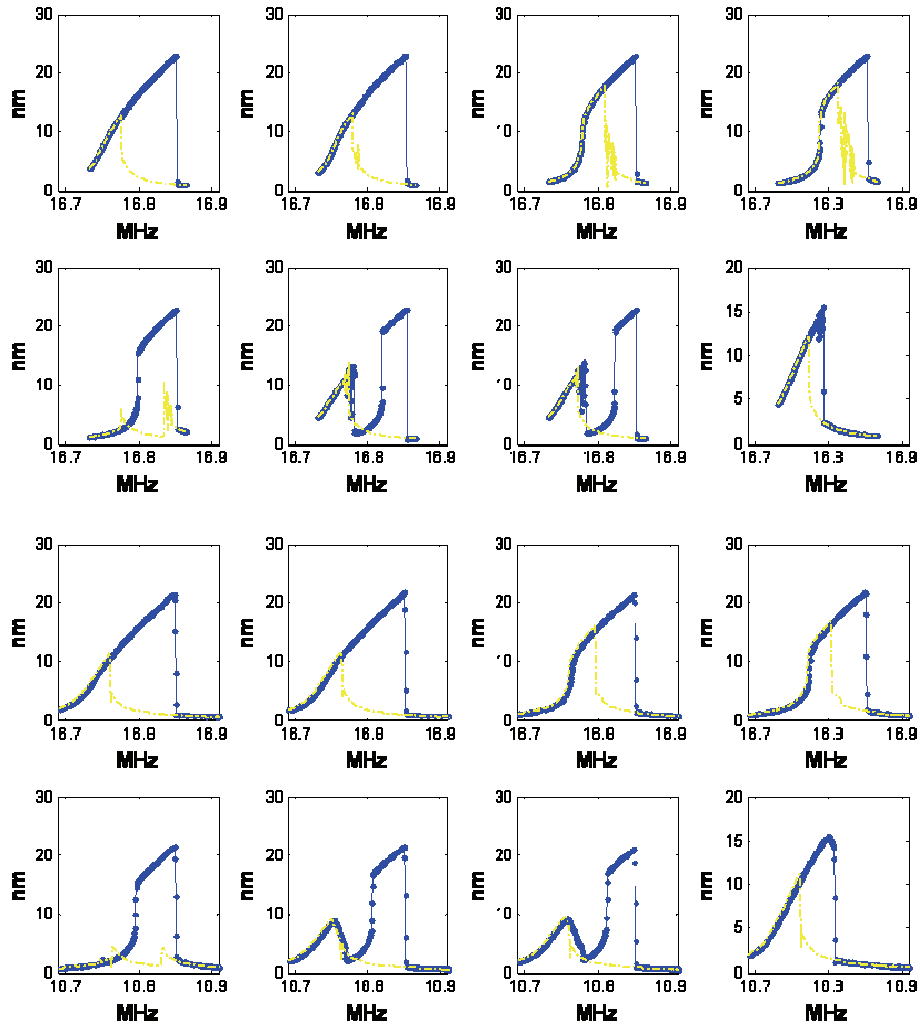


Figure 6.7 The evolution of the shape of the first mode when the frequency of the second mode is swept upward, while both peaks are driven at approximately four times the onset of nonlinearity

Initially, the wide Duffing response shrinks and an abrupt upward jump on the left side starts to appear. This phenomenon is caused by the fact that when the amplitude of the first mode is small, its effective nonlinearity is negative, so that it jumps to the upper state as the frequency is swept up. This transition shifts upward due to the frequency tuning discussed earlier. Since the amplitude

of the motion in the upper state is comparable to the amplitude of the second mode the transition causes the second mode, amplitude to drop to the lower state. As a result, the spectral response continues along the unperturbed Duffing curve. For the last three plots the vibration state of the second mode is unstable, hence it undergoes upward and downward transitions during the sweeps. And the very last plot is similar to unperturbed Duffing because the second mode is always in lower state. It is easy to notice that theoretical curves have noisy parts which correspond to sharp decreases in amplitude in experimental plots. These features are real physical phenomena of considerable importance, which are discussed in detail below. Despite seemingly complex behavior of the coupled system, a simple nonlinear model precisely explains the dynamics both qualitatively and quantitatively with a precision of lower than 5%.

In order to further illustrate dynamics of the system, another type of sweep was performed. In these measurements the drive level of the first mode was steadily increased while its peak shape was monitored by a network analyzer. In the absence of the second coupled mode the response is a regular Duffing curve, but when the second mode is excited at high level the spectral responses assume more complicated shapes, which are shown in figure 6.8. The top plots are the theoretical calculations while the bottom ones are the experimental measurements. The plots on the right are the sweeps upward and the ones on the left are the sweeps downward. Multiple transitions between upper and lower state of the vibration of both modes cause the complex spectral response behavior. During the upward sweeps the initial effective nonlinearity is negative, and therefore the resonance peak leans leftward. Above some amplitude the transition to the upper state causes the second vibration to drop to lower state and the frequency sweeps continue along the unperturbed Duffing curve.

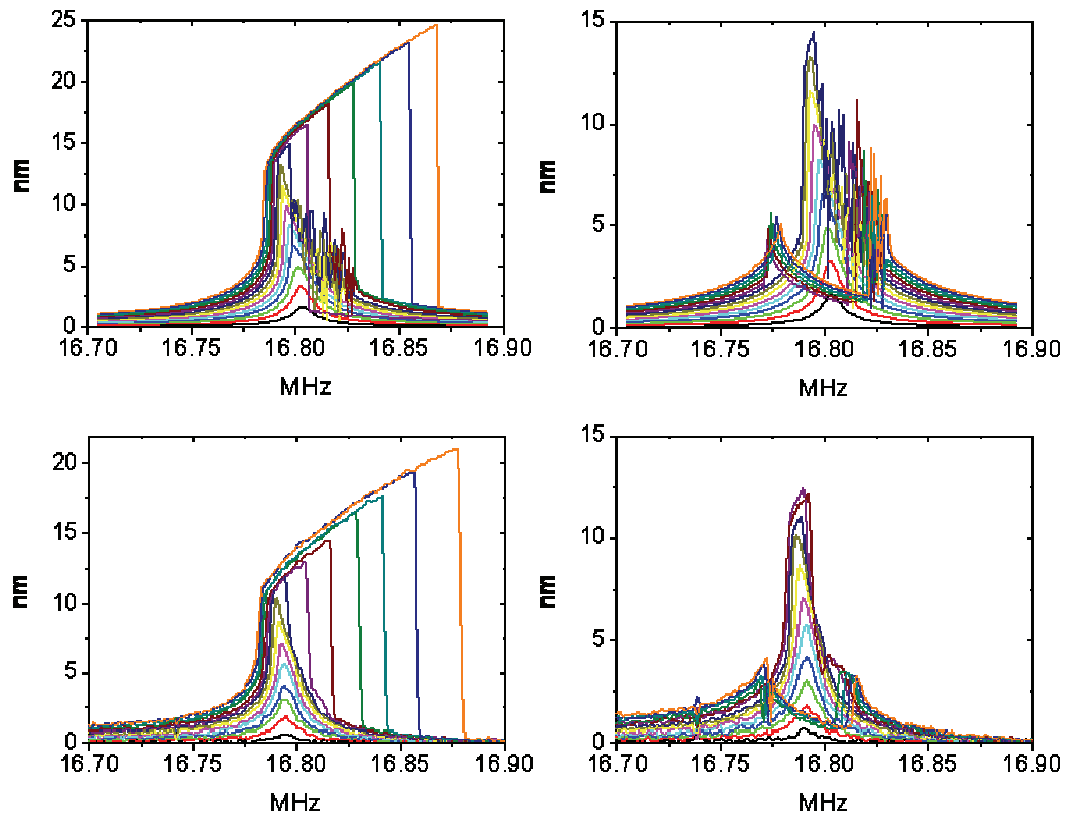


Figure 6.8 Frequency sweeps of coupled Duffing resonators: The response of the first mode is shown as its driving frequency is swept for various drive amplitudes. Theoretical simulations are shown in the top row and experimental measurements in the bottom row. The drive strength and frequency of the second mode is fixed.

On the other hand during the down sweep for low amplitudes the response is consistent with a regular down frequency sweep with negative Duffing coefficient. But when the excitation level increases, the preceding up sweep causes the second mode to be in the lower state at the beginning of corresponding down sweep, causing it to go along a different unperturbed Duffing curve with positive nonlinearity. When there is the expected transition to the upper state, the second mode also switches to the upper state, and as a result there are instabilities in the steady state of mechanical

vibration causing wiggles to appear in the plots. For even higher driving strengths the curve continues along lower state of another Duffing curve without transitioning to upper state.

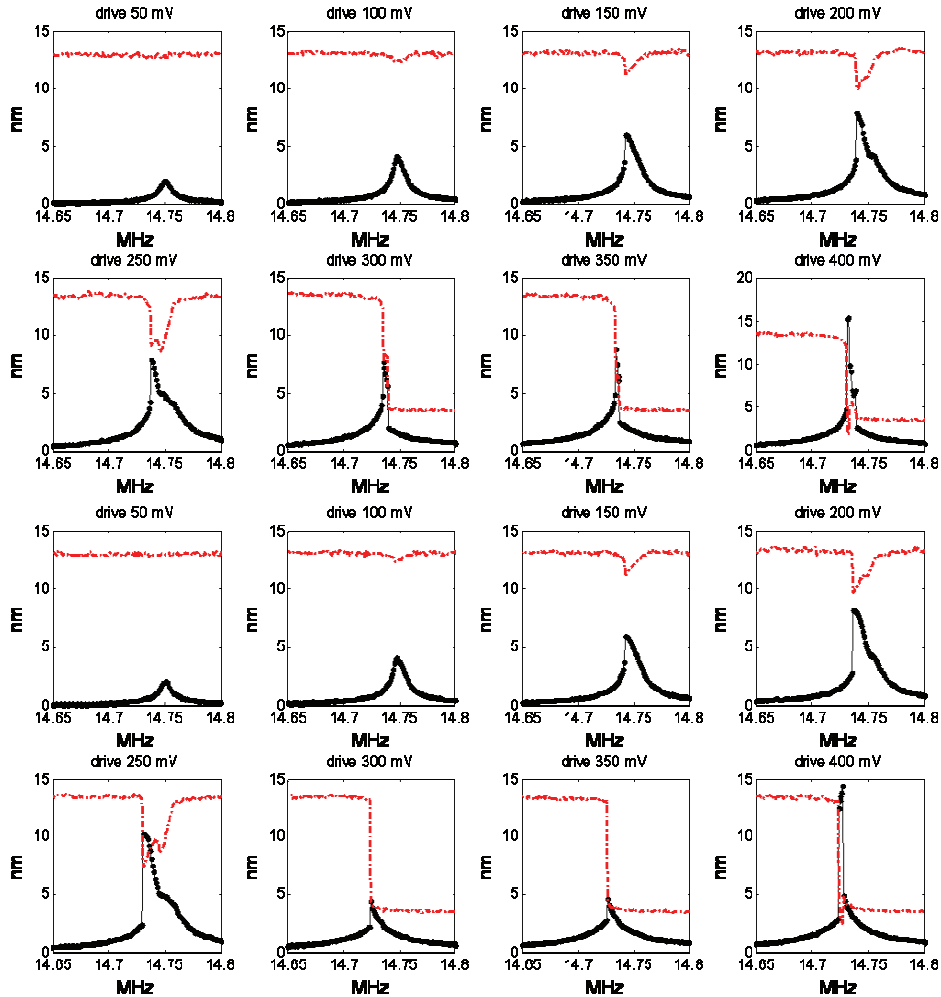


Figure 6.9 The first mode amplitude sweep of the stronger coupled system of Duffing resonators. the first mode (black) and the second mode (red) are measured. Top plots are the frequency sweeps in upward direction, while bottom ones are the sweeps in downward direction.

In order to verify the expected transition for second peak, measurements where the amplitudes of both modes are monitored via a spectrum analyzer were performed. The results of the

measurements for the second (stronger coupled) device from Table 6.1 are shown in figure 6.9.

The spectral response of the first mode is shown in black while the corresponding second mode amplitude is shown as the red curve. (Its frequency is higher close to its own resonance; the response is shown in the same plot for convenience). The top plots are the upward sweeps while the bottom ones are the downward sweeps. The second mode is driven at 350 mV, which is about twice the onset of nonlinearity. The drive level for the first mode is shown for each plot. Complicated dynamics near the transition points are apparent on the plots.

6.5 MECHANICAL STATE INSTABILITIES AND CHAOS

In most of the theoretical plots above noisy structures appear between solution branches in regions near the up or down transitions. They often correspond to decreases in the experimental mechanical amplitudes, although not sharp jumps from state to state. In the theoretical analysis, the algorithm numerically solves time-dependent differential equations (6.9). This usually results in steady state solutions for A_I and A_{II} , which represent the amplitudes of sinusoidal mechanical motion at the frequencies of the corresponding driving forces. The procedure has to be computed for sufficient number of time steps for amplitudes to stabilize. It turns out that at some initial parameter settings it is impossible to get to the steady state, because the mechanical vibrations are unstable. The fast ~ 15 MHz oscillating sinusoidal signal becomes amplitude modulated, with its mechanical displacement amplitude changing periodically at a rate of about 10 to 20 kHz. Consequently wiggling noisy structures appear in theoretical plots.

On the other hand in the way the experimental measurements are performed, it is not possible to see the wiggles, because in the network analyzer only a narrow frequency band around the drive is analyzed. The modulation seen in the theoretical analysis would lead to a drop in the measured

amplitude, because part of the RF power is transferred into amplitude modulation satellite peaks, outside measured band.

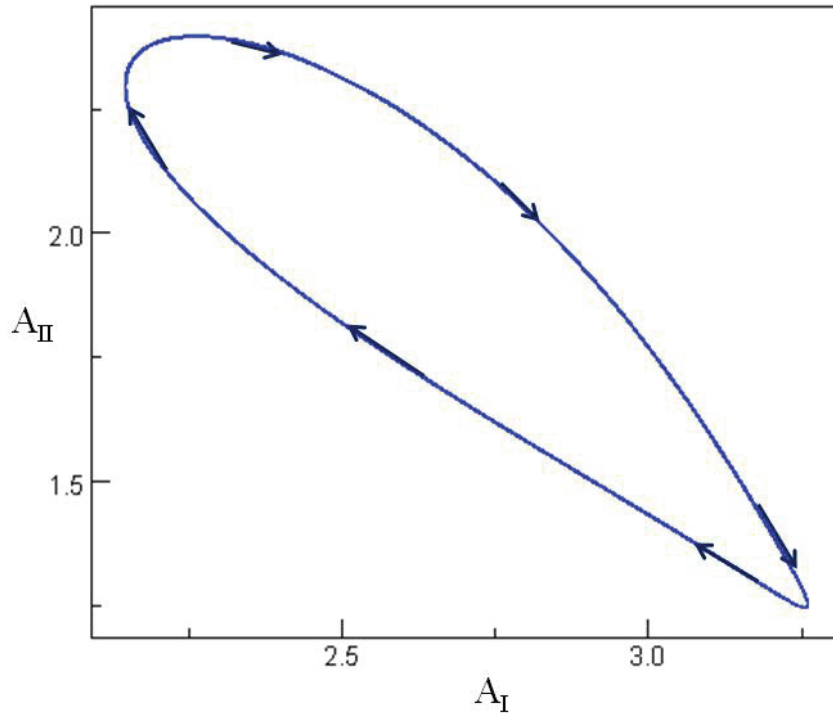


Figure 6.10 A simple example of the phase plot of the second mode amplitude versus the first mode amplitude. The vibration state of the system travels along the arrows and completes the cycle at a rate slightly faster than the ringdown time.

The detailed analysis of the system of equations (6.9) reveals that the modulations of the two modes are anticorrelated. An example of a simple case of a phase trajectory of A_{II} versus A_I is shown in figure 6.10. The vibration state travels around the elliptic shape along the arrows shown in the figure. The dynamics can be roughly understood as follows, when the first mode is in its lower state and the second mode is in its upper state (top-left corner) the first mode switches to the upper state causing the second mode to drop to the lower one (bottom-right corner). In this

condition the second mode is unstable in its lower solution branch and makes a jump to the upper state again, kicking the first mode down to its lower state, starting the cycle again. As a result the system reaches a dynamical equilibrium where the two modes periodically transfer energy between one another.

Although the modulations are impossible to observe with a lock-in-type network analyzer measurement, it is easy to study them with a spectrum analyzer with a wider frequency range. An example of an amplitude modulated spectral response is shown in figure 6.11(a).

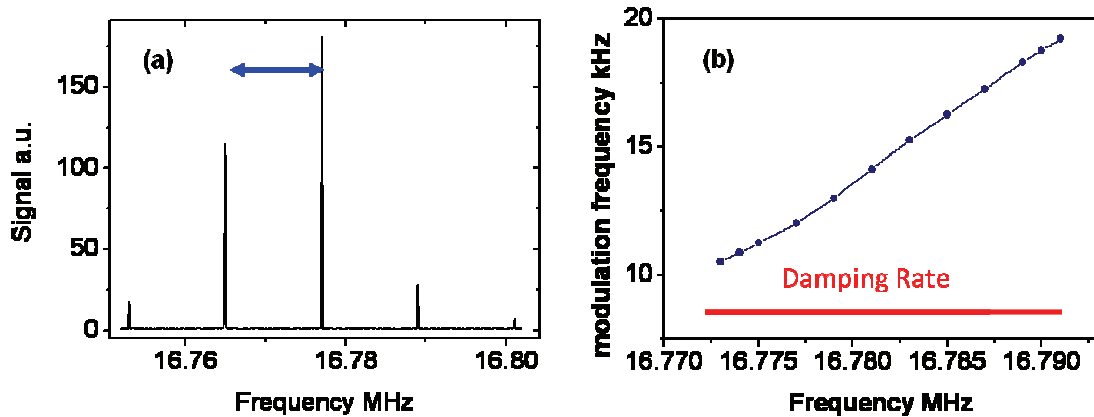


Figure 6.11 (a) Typical spectrum of an amplitude modulated mechanical motion of the first mode of the system, due to a dynamical equilibrium of the two modes transferring energy between one another. (b) Measurement of the modulation rate over a 20kHz wide transition range. The damping rate is shown as a red line on the plot.

According to theoretical predictions, a reasonable time for a solution to settle onto a new state is a ring down time. But in the case of two coupled modes during the transition from state to state another dissipative channel emerges. The results of the measurements of the modulation frequency performed on the first device in Table 6.1 are plotted in figure 6.11(b). When the first and second

modes are driven at 2.24 and 2.8 above the onset of nonlinearity respectively, a region of modulated vibrations as wide as 20kHz appears during the first mode frequency sweep. The plot shows the dependence of the modulation frequency on the first mode drive frequency. The expected damping rate given by ω_l/Q is shown as a red line on the plot.

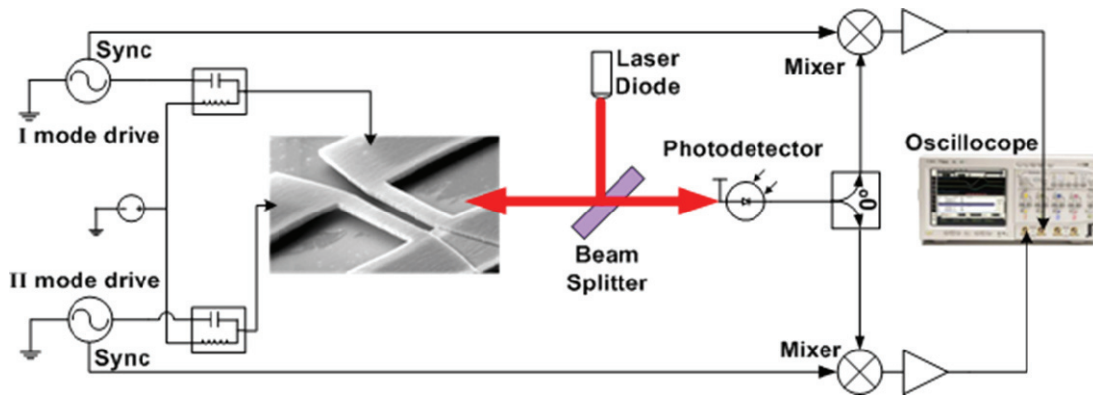


Figure 6.12 Measurement setup for A_{II} versus A_I phase plots measurements. Homodyne downconversion is used in order to obtain quasi-dc envelope signal.

In order to experimentally observe the expected shapes the measurement setup shown in figure 6.12 is employed. A transduced mechanical signal is subjected to a homodyne downconversion using a “sync” output from function generator. Then the quasi-dc signals from the two modes, which are the envelopes of the corresponding RF carriers, are read by independent oscilloscope channels. As a result only the real component of the amplitudes is measured.

In addition to relatively simply shaped phase plots similar to the one in figure 6.10, more complicated ones occur under specific conditions. Examples of different types of simulated and measured phase plots are shown in figure 6.13. The strongly coupled second device from Table 6.1 is used in these measurements. The top row shows an example where A_{II} versus A_I plot forms a small loop. The first plot is the theoretical simulations, which are performed using the same

algorithm as described earlier. The second plot is a corresponding oscilloscope Lissajous-figures type measurement. The third plot is the spectrum of the measured mechanical signal: it includes the amplitude modulation satellite peaks. The peaks are not symmetric, which is consistent with the anharmonic shape of the modulation. The middle row is another example of a simple phase plot. Good agreement between theoretical predictions and experimental measurements is obvious from the figure. Under specific conditions the phase plot may experience a period doubling phenomenon, where a complex phase trajectory takes two periods in order to complete the cycle. An example of period quadrupling is shown in the bottom row of figure 6.13. The phase diagram forms a closed loop pattern only after four revolutions. The corresponding complicated loop structures are visible in both theoretical and experimental plots. The full spectrum of mechanical motion reveals amplitude modulation peaks at frequencies that correspond to double and quadruple periods.

This phenomenon was previously theoretically predicted [50, 51] and observed in coupled microwave circuits [52]. One of the interesting effects studied in previous research is the fact that period doubling, quadrupling and so on eventually leads to chaotic behavior under particular experimental conditions.

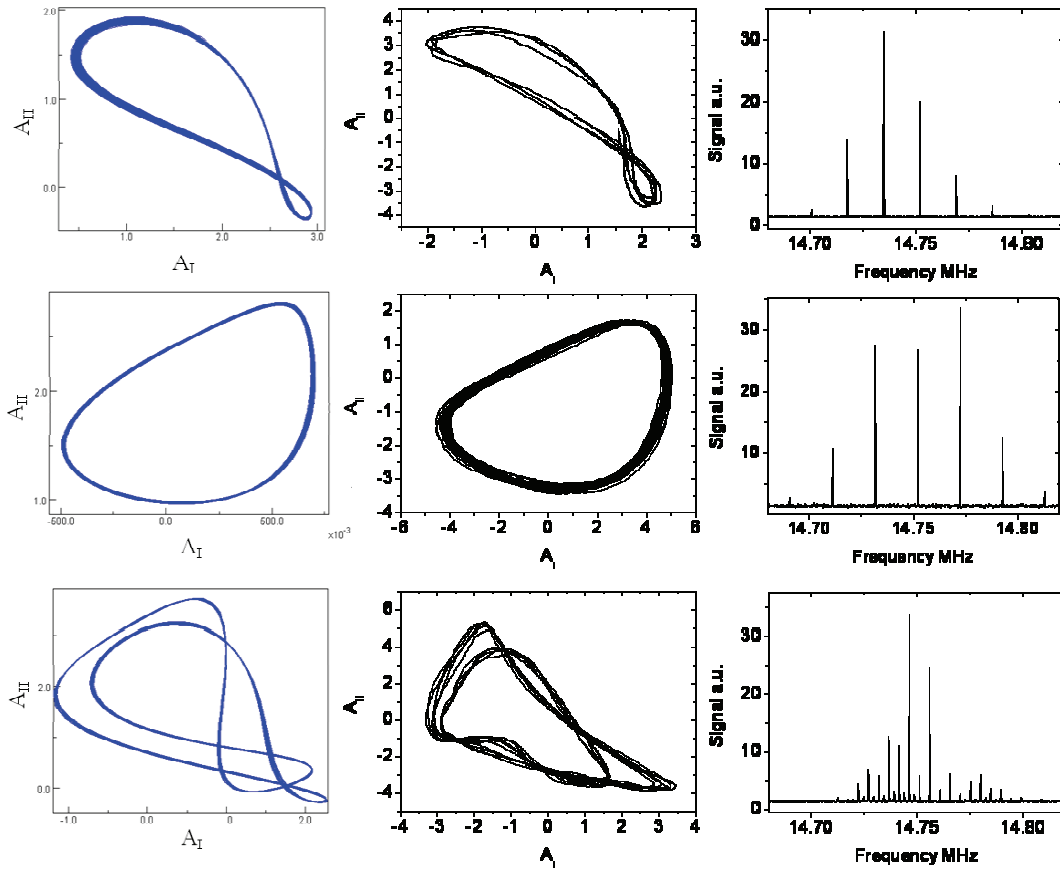


Figure 6.13 Example of the A_{II} versus A_I phase plots along with corresponding Lissajous and spectrum analyzer measurements for three different sets of input parameters.

For the stronger coupled second device the simulation predicts chaotic behavior, which was tested using the described measurement procedure. Figure 6.14 shows theoretical and experimental plots of the chaos in coupled nanoelectromechanical systems. In the simulations it turns out that the closed pattern never forms and the trajectory continues to travel covering limited region in A_{II} vs A_I phase space. In the experiment though, the measurement is limited to only a finite number of periods, and hence the second column plots appear as noisy Lissajous figures. Comparing them to

the plots of Figure 6.13 it is apparent that in figure 6.14 the closed pattern does not form and the phase plot is chaotic. The spectrum analyzer measurements confirm the hypothesis: the amplitude modulation features appear as wide continuous spectrum peaks, contrary to the sharp delta functions in the previous plot.

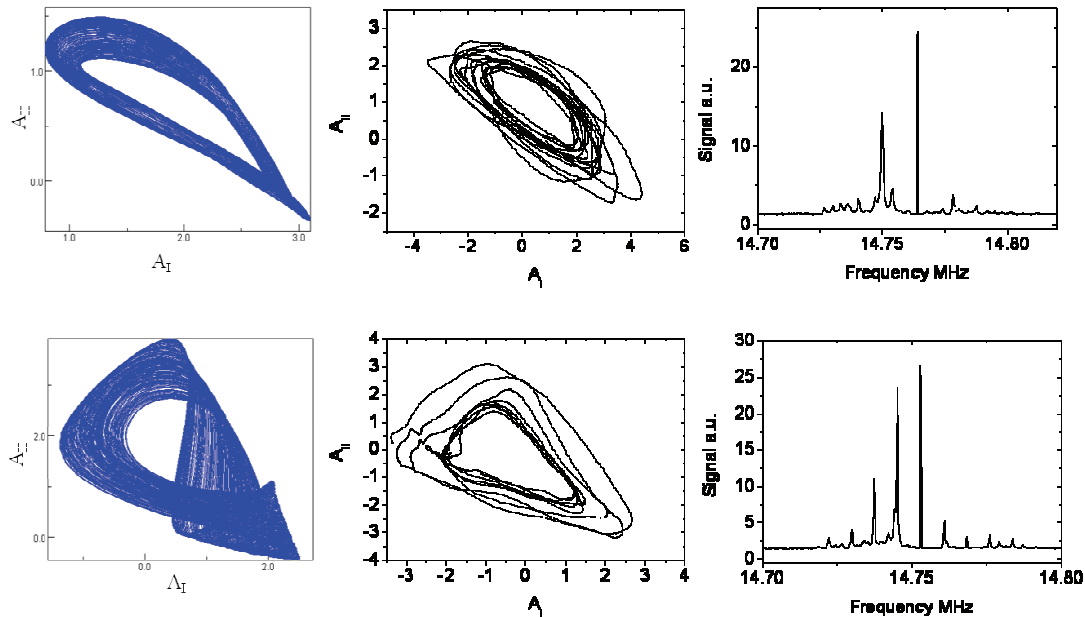


Figure 6.14 The observation of the chaotic behavior in coupled nanoelectromechanical systems. The plots in the first column are obtained by theoretical simulations. The second and the third columns consist of oscilloscope and spectrum analyzer measurements respectively.

To the author's knowledge this experiment is a first demonstration of chaotic behavior in nanoelectromechanical systems.

SUMMARY

This chapter presented the detailed study of two strongly coupled nonlinear resonators. The understanding of the underlying physical phenomena is crucial for integration of the devices into

large arrays and utilizing all the available dynamic range. A formalism for characterization of the coupled nonlinear system was developed for the theoretical analysis. Seemingly simple system provided remarkably rich dynamical behavior.

Strongly coupled Duffing resonators allow significant increase in dynamic range by quenching the effective nonlinearities. In the first approximation the motion of one of the beams couples quadratically to the resonance frequency of the other beam providing a very promising scheme for quantum nondemolition measurements in nanoelectromechanical systems. Surprisingly complex behavior is observed where the energy of mechanical motion is transferred to and from the modes near the solution state transition regions. Under specific experimental conditions this effect gives rise to a chaotic behavior in the two modes of the nanoelectromechanical system. All the incredible variety of described physical phenomena was measured experimentally, and the results agree well with theoretically predictions.

Chapter 7

BIFURCATION-TOPOLOGY AMPLIFIER

This chapter describes an increased complexity where two coupled resonators are excited parametrically. Considering a weak coupling case a novel amplification mechanism is discovered. It is based on the dynamical changes that an input signal induces in the topology of a simple bifurcation diagram, rather than employing an existing bifurcation [53,54]. Theoretical background for such a bifurcation-topology amplifier as well as detailed experimental implementation and characterization are described in this chapter.

7.1 PARAMETRIC ACTUATION OF TWO WEAKLY COUPLED RESONATORS

Earlier in chapter 2 we described the behavior of a single parametric resonator. We now consider two weakly coupled nonlinear resonators with slightly different normal frequencies. Their dynamics are governed by a pair of equations of motion (EOM), which is a combination of equations (2.8) and (6.1)

$$\ddot{x}_i + \gamma \dot{x}_i + (\omega_i^2 + 2h_p \cos \omega_p t)x_i + \alpha x_i^3 + D(x_i - x_j) = 0 \quad i, j = 1, 2, \quad i \neq j, \quad (7.1)$$

where x_1 denotes the displacement of the lower-frequency resonator with frequency ω_1 from its equilibrium, and x_2 denotes the displacement of the higher-frequency resonator with frequency ω_2 . Duffing parameter α and linear damping rate γ are assumed to be approximately the same for both resonators, and the coupling strength between the resonators is denoted by D . The parameters h_p and ω_p are the parametric driving amplitude and driving frequency. The responses of these coupled resonators are calculated using similar secular perturbation theory methods.

A small dimensionless parameter ε is introduced and the parameters in the above equation are rescaled in the similar fashion as in equation (2.9) and (6.2). In addition to that the coupling

between resonators is weak, therefore we introduced scaled coupling constant $D_s = \varepsilon D$. The resonance frequencies are assumed to be very closely separated, hence we define another parameter $\varepsilon\delta = (\omega_2^2 - \omega_1^2)/2$ (which is slightly different definition compared to equation (5.5)),

$$\ddot{x}_i + \varepsilon\Gamma \dot{x}_i + (\omega_m^2 \pm \varepsilon\delta + 2\varepsilon h \cos[2\omega_m + \varepsilon\Omega]t)x_i + \alpha x_i^3 + \varepsilon D_s (x_i - x_j) = 0. \quad (7.2)$$

We search for the solution in the form proportional to $\sqrt{\varepsilon}$ as in equation (2.10). After making a substitution the terms proportional to $\varepsilon^{1/2}$ cancel because they are the part of linear equation for simple harmonic oscillator. Therefore keep $O(\varepsilon^{3/2})$ terms we obtain an equation for the first-order corrections, where the resonance drive is required to vanish for the solution to exist. Hence the equation for slower amplitudes $A_i(T)$ assumes the form:

$$2i\omega_m \frac{dA_i}{dT} + D_s (A_i - A_j) \pm \delta A_i + hA_i^* e^{i\Omega T} + i\Gamma \omega_m A_i + 3\alpha |A_i|^2 A_i = 0. \quad (7.3)$$

We ignore initial transients and search for steady solution vibrating at half the pumping frequency:

$$A_i(T) = a_i e^{i\frac{\Omega}{2}T}. \quad (7.4)$$

Substitution of this expression into (7.3) yields a system of two algebraic equations, by solving which amplitudes a_i are obtained.

$$\begin{aligned} (D_s - \delta - \omega_m \Omega + 3\alpha |a_1|^2) a_1 - D_s a_1 + i\omega_m \Gamma a_1 &= -h a_1^* \\ (D_s + \delta - \omega_m \Omega + 3\alpha |a_2|^2) a_2 - D_s a_2 + i\omega_m \Gamma a_2 &= -h a_2^* \end{aligned} \quad (7.5)$$

Setting $D=0$ decouples the equations, giving two independent equations that were solved in closed form in chapter 2. The solution to a single equation gives the response curve, shown in figure 7.1(a), with stable solutions given by red solid curves, and unstable solutions by blue dotted curves. The phase of the response, which is not plotted, is determined only to within a π phase

shift, due to the fact that the drive completes two periods whenever the resonator completes only a single period at half the frequency. Our BTA consists of two such resonators, with slightly different resonance frequencies, which are excited simultaneously using the same drive source, but are otherwise uncoupled. Because of the π phase freedom in the response of each resonator, when both are excited there is a 50% chance that they will respond in phase, and a 50% chance that they will respond with opposite phase. Consequently, the summed response of the two resonators $|a_1+a_2|$ – shown in figure 7.1(b) – forms a pitchfork bifurcation. Sweeping up the pump frequency ω_p , while keeping all other parameters fixed, first excites the lower-frequency resonator while the higher-frequency resonator is still dormant, following the curve labeled $\uparrow 0$. When the second resonator begins oscillating, the summed response of the two resonators follows the upper branch $\uparrow\uparrow$ if both resonators are in phase, and follows the lower branch $\uparrow\downarrow$ if they respond out of phase. This behavior is confirmed experimentally in figure 7.2(a), as described below.

The situation changes when nonzero coupling is introduced between the resonators, then the roots of the coupled equations (7.5) are calculated numerically. The results are shown in Figs. 7.1(c) and (d) for positive and negative coupling respectively.

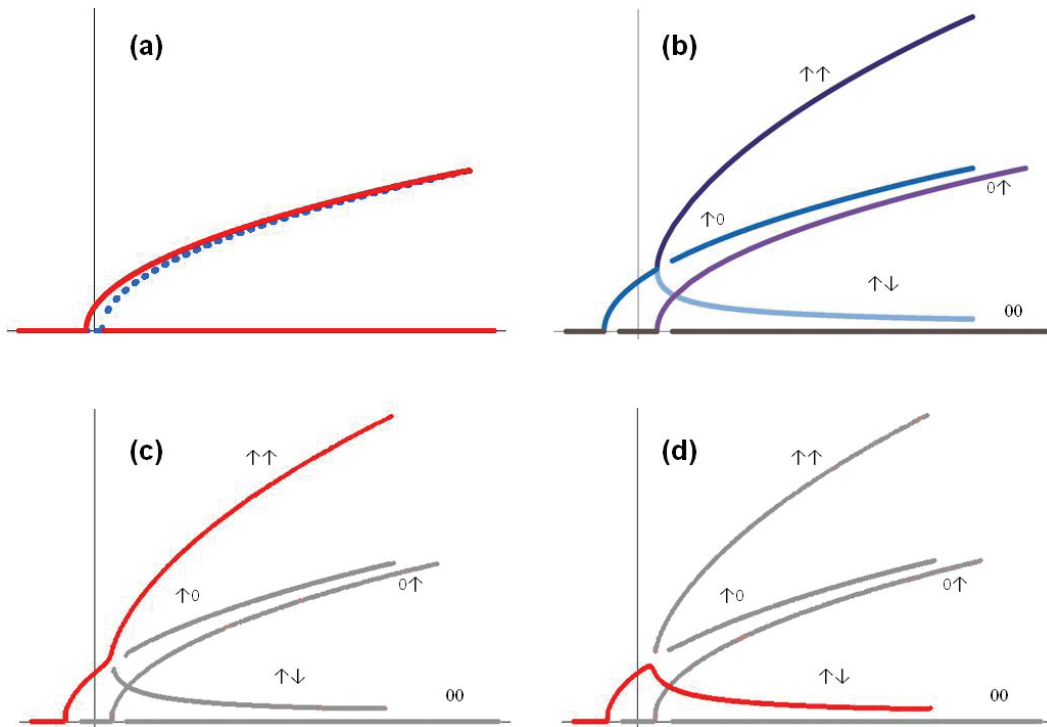


Figure 7.1(a) Response amplitude of a single nonlinear resonator. Stable solutions are in solid red; unstable in dotted blue. (b) Summed response of two uncoupled resonators to a single drive. Only stable branches are shown: Purple: zero-state (00); Green: only the first resonator is oscillating ($\uparrow 0$); Red: only the second resonator is oscillating ($0 \uparrow$); Blue: both resonators oscillating in phase ($\uparrow \uparrow$); Orange: both resonators oscillating in antiphase ($\uparrow \downarrow$). (c) Summed response with attractive coupling. Only stable branches are shown and are labeled as in plate (b). (d) Summed response with repulsive coupling. Only stable branches are shown and are labeled as in plate (b).

Finite coupling $D \neq 0$ changes the topology of the bifurcation diagram, causing a distortion of the perfect pitchfork (the bifurcation is said to be imperfect). With attractive coupling ($D > 0$), as shown in figure 7.1(c), the incoming $\uparrow 0$ branch is connected only to the in-phase $\uparrow \uparrow$ branch. With repulsive coupling ($D < 0$), as shown in figure 7.1(d), the opposite happens, and the incoming $\uparrow 0$ branch is connected only to the antiphase $\uparrow \downarrow$ branch. A quasi-static upsweep of the pump

frequency that starts to the left of the bifurcation easily distinguishes between attractive and repulsive coupling. It follows the upper branch if the coupling is attractive – with the second resonator oscillating in phase with the first – and follows the lower branch if the coupling is repulsive – with the second resonator oscillating in antiphase with the first. This dependence of the bifurcation topology on the effective coupling D between the resonators can be used as an amplification scheme by setting D to be proportional to the input signal V_{in} that we wish to amplify.

7.2 VOLTAGE-DEPENDENT BIFURCATION DIAGRAM

We have implemented such a BTA using a pair of $6\mu\text{m}$ long, 500nm wide, and 200nm thick D-NEMS beams, separated from each other by 400nm , as shown in the inset of Figure 7.2(a). Their fundamental out of plane resonance frequencies are around 13.1 MHz , differing by about 30 kHz as a result of fabrication imperfections. Their quality factors in vacuum at room temperature are about 1700 . The details on measurement technique and parametric actuation are given earlier in chapter 4. Parametric oscillations are effectively excited by modulating the applied V_{bias} with amplitude of 0.2V at twice the resonance frequency – around 27.2 MHz . The summed response of the amplitudes of the two beams $|a_1+a_2|$ is measured because the spot size of the laser beam covers the area of both nanomechanical resonators. The interference signal is stronger when the beams oscillate in phase and weaker when they oscillate out of phase.

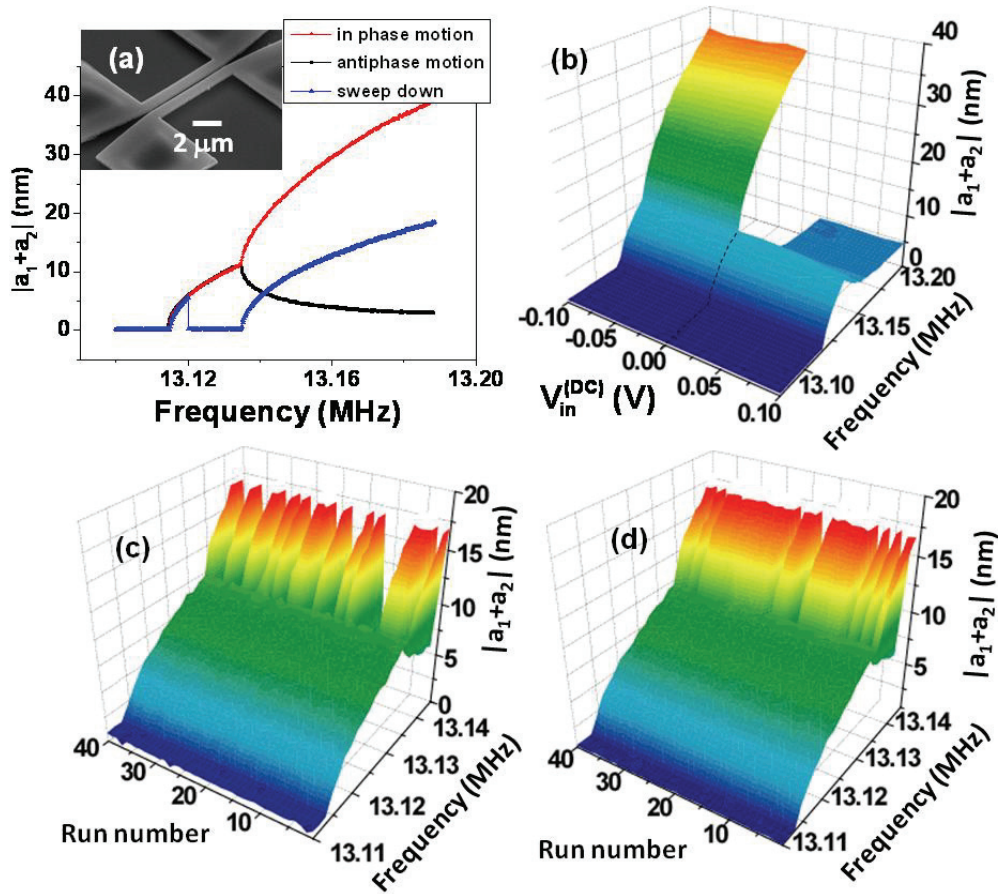


Figure 7.2 (a) Experimental confirmation of the pitchfork bifurcation, shown in figure 7.1(b). (b) With a constant input signal $V_{in}^{(DC)}$ larger than the noise floor, the response to upward frequency sweeps deterministically follows the upper or lower curves depending on the sign of $V_{in}^{(DC)}$. (c) Repeated upward frequency scans with no coupling, $V_{in}^{(DC)} = 0$, show that about half follow each of the two possible branches. (d) Repeated upward frequency scans with a negative input signal, $V_{in}^{(DC)} = -3\text{ mV}$, show that more than half of the scans follow the upper in-phase response curve, yet because the noise amplitude is greater than 3mV some scans still follow the lower antiphase response curve.

The optical response was calibrated using the intrinsic Duffing nonlinear properties of the nanoresonators, by measuring the onset of nonlinearities [19]. Direct frequency response measurements made by vector network analyzer (HP3577A) are shown in figure 7.3. The drive here is changed from 50mV_{rms} to 1.2V_{rms} . The onset of nonlinearity occurs at $\sim 600\text{mV}_{\text{rms}}$ drive level with the optical signal of approximately $\sim 70\mu\text{V}_{\text{rms}}$. The estimated accuracy of the calibration is of the order of $\sim 10\%$. The parametric sweeps are measured by Agilent 4395A spectrum analyzer.

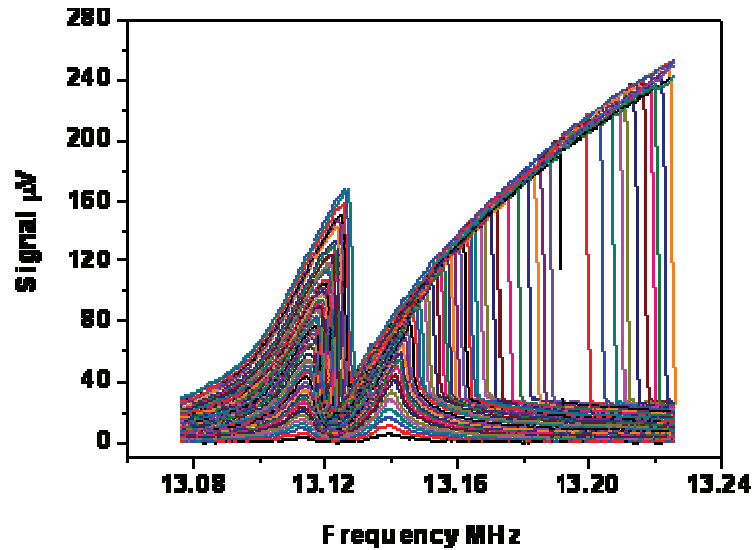


Figure 7.3 Duffing nonlinearities dominate at high excitation levels. The onset of nonlinear behavior depends only on quality factor and geometry of the beam, hence it is a good way of calibrating the optical interferometer responsivity.

The applied V_{bias} applied between top and bottom electrodes of the resonators also induces electric dipoles within the layers of the beams, shown in figure 5.2 causing the beams to repel each other, as it is described earlier in section 5.1. Thus the electrostatic coupling reduces the coefficient D . Using the geometry of the D-NEMS resonators used in the experiment the electrostatic force is

approximately $\sim -1\text{pN}$ for a displacements difference of the order of 1 nm. Without any applied voltage there is residual attraction between the beams due to elastic coupling through their shared elastic support, even though no ledge is shared by the beams. Finite element simulations (see Figure 7.4) are used for elastic coupling estimation, for experimental devices' geometry the effective interaction force was calculated to be $\sim 1\text{pN}$ at experimental conditions.

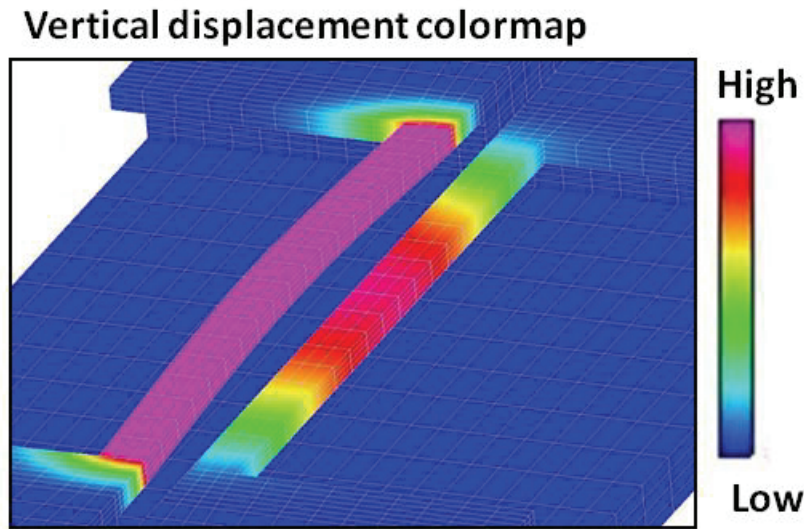


Figure 7.4 Finite element simulation is used to estimate positive residual coupling between beams, which share the elastic support, although the coupling is minimal due to the lack common ledge.

Geometry of the system was designed so that positive offset bias V_{offset} , within the experimental range is required to compensate for this elastic attraction and to null this intrinsic geometric coupling between the beams. This voltage is about $V_{offset}=1.1\text{V}$ in our implementation, thus the effective coupling between the beams, which we use as our input signal, is given by $V_{in}(t)=V_{bias}(t)-V_{offset}$, which is proportional to $-D(t)$.

Figure 7.2(a) shows the measured summed response of the two beams for zero effective coupling, when $V_{in}(t)=0$, confirming the existence of the pitchfork bifurcation, as described earlier

and shown in figure 7.1(b). Figure 7.2(b) shows a sequence of upward frequency sweeps for a constant input signal $V_{in}(t)=V_{in}^{(DC)}$, clearly showing that for negative constant signals ($V_{in}^{(DC)}<0$) corresponding to attractive coupling ($D>0$), the summed response follows the upper curve; for positive constant signals ($V_{in}^{(DC)}>0$) yielding repulsive coupling ($D<0$), the summed response follows the lower curve. The device thus operates as a very sensitive discriminator between positive and negative signals V_{in} , whose resolution is limited only by the amplitude of the background noise. This background consists of the noise accompanying the input signal itself, as well as that of the mechanical motion of the beams. In the presence of such noise there is a delicate balance between following the upper or lower branches for $V_{in}=0$, as shown in figure 7.2(c). This balance is modified in favor of the lower branch for $V_{in}^{(DC)}>0$ and in favor of the upper branch for $V_{in}^{(DC)}<0$, as shown in figure 7.2(d) for $V_{in}^{(DC)}=-3\text{mV}$. Note, however, that there is still some chance of following the wrong branch if the noise amplitude is greater than $V_{in}^{(DC)}$. Only when $V_{in}^{(DC)}$ significantly exceeds the noise do the quasi-static frequency sweeps become deterministic. In fact, as explained below, adding noise can be used to increase the operating range of the BTA.

7.3 BIFURCATION TOPOLOGY AMPLIFIER MEASUREMENTS

The actual measurement layout realizing the BTA is shown in figure 7.5. The RF source used for parametric pumping is frequency modulated (FM) with a triangular waveform, resulting in fast linear frequency sweeps that start below the bifurcation point in order to reset the BTA before sweeping upward to detect the sign of the input signal $V_{in}(t)$.

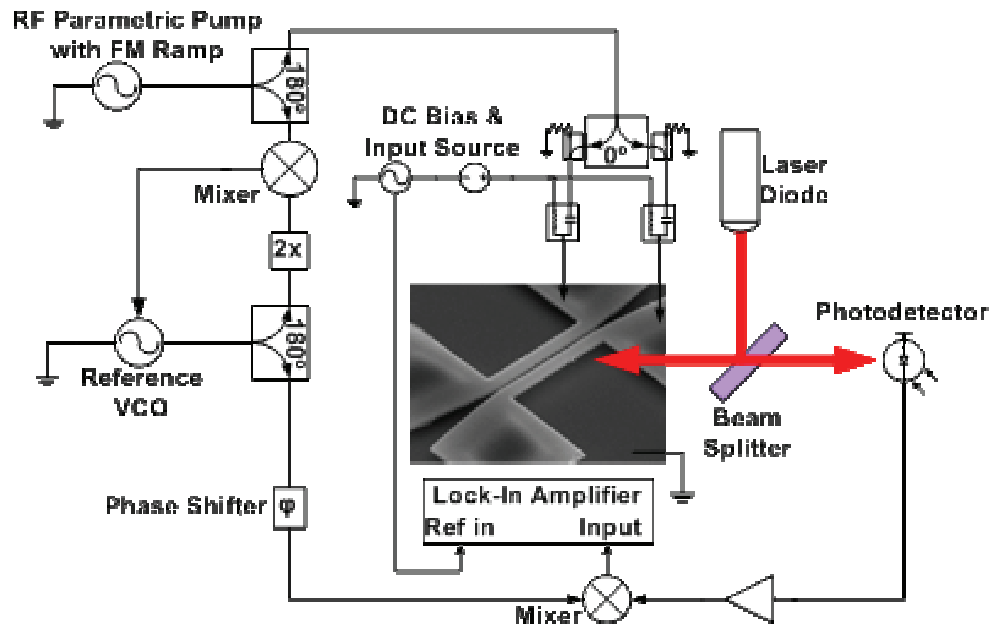


Figure 7.5 Full circuit diagram of bifurcation-topology amplifier realization. Half frequency reference is obtained by synchronizing additional RF source through phase locked loop. The amplitude demodulation of output signal is performed by mixing it to the reference. Oscilloscope is used instead of lock-in amplifier to obtain time-domain response.

There are several fundamental limitations on the sweep rate of the pump frequency that should be noted. On the one hand, the sweep rate has to be at least twice as fast as the input signal $V_{in}(t)$ to allow for proper sampling. On the other hand, if the sweep rate is too fast it may introduce timelags in the response of the resonators because unwanted transients do not have sufficient time to relax toward steady-state oscillations. This may cause the response to skip from one branch to another instead of following the topology of the bifurcation diagram, which is essential for the proper performance of the BTA. The typical relaxation time for transients is given by the inverse of the damping rate γ . For a resonance frequency of 13.1 MHz and a quality factor of 1700, the relaxation

time is on the order of 0.1 ms. In the experiment, we observe the output signal deteriorating at sweep rates of 2 kHz corresponding to relaxation times around 0.5 ms, in agreement with this rough estimate. Thus the bandwidth of our present realization of a BTA is limited to about 1 kHz.

During normal bifurcation-topology amplifier operation the DC bias is set to bifurcation point $V_{in}^{(DC)}=0$ and modulated by small square wave periodic voltage of the form $V_{in}^{(AC)}sqw(t)$, where $sqw(t)$ is a square wave function that changes from -1 to +1 with a period of T_{in} . Typical input frequency used in measurements is 167Hz, it was increased without significant change in output signal as long as it is factor of 2 slower than the FM rate. Agilent 33250A function generator was used as a source of constant DC offset and input voltage, which was applied to the device's electrode via DC/RF bias tee.

The output from photodetector consists of contributions from two beams due to the readout mechanism. The first beam's response is almost constant in amplitude frequency-modulated signal:

$$\begin{aligned} V_{first} &= V_1 \cos(\omega(t)t), \\ \omega(t) &= \omega_0 - \Delta\omega_{offset} + \Delta\omega_{FM} RMP(t), \end{aligned} \quad (7.6)$$

where V_1 is amplitude of the first beam's optical response, which does not change much in this approximation, ω_0 is frequency of the bifurcation, $\omega_0 - \Delta\omega_{offset}$ is a left edge of FM sweeps, $\Delta\omega_{FM}$ is a frequency modulation depth and $RMP(t)$ is a triangle function that changes from 0 to 1 and back at a period of T_{rmp} :

$$RMP(t) = \begin{cases} \left\{ \frac{2t}{T_{rmp}} - \left\lfloor \frac{2t}{T_{rmp}} \right\rfloor, \left\lfloor \frac{2t}{T_{rmp}} \right\rfloor \right. & \text{even,} \\ \left. -\frac{2t}{T_{rmp}} + \left\lceil \frac{2t}{T_{rmp}} \right\rceil, \left\lceil \frac{2t}{T_{rmp}} \right\rceil \right. & \text{odd.} \end{cases} \quad (7.7)$$

The RF parametric pump at $\sim 26\text{MHz}$ is performed by Agilent 33250A function generator with internal triangular frequency modulation. In most of the measurements FM rate of 557Hz was used. The rate was varied from 70Hz up to 3kHz in amplifier bandwidth study. 3dB decrease in gain was observed at 2kHz .

The second beam's response significantly changes in amplitude in addition to being frequency modulated.

$$V_{second} = V_2(t)sqw(t) \cos(\omega(t)t), \quad \text{where}$$

$$V_2(t) = \begin{cases} V_{2max} \sqrt{\frac{\omega(t) - \omega_0}{\Delta\omega_{FM}}}, & \omega(t) > \omega_0, \\ 0, & \omega(t) \leq \omega_0. \end{cases} \quad (7.8)$$

The expression for $V_2(t)$ here shows the behavior of the second beam's amplitude when pumping frequency is modulated. The nonzero amplitude increases as a square root with frequency only when it is above bifurcation $\omega(t) > \omega_0$ (see theoretical section above). We normalize the amplitude to the maximum value V_{2max} when the ω_0 corresponds to the left edge of frequency sweeps. Square wave function means that the sign of second beam's contribution changes with input voltage. Although the noise in the system distorts $sqw(t)$, canceling some high–low level transitions, we omit this effect in this simple explanation of measurement setup operation.

The total output signal is a sum of V_{first} and V_{second} from equations (7.6) and (7.8). RF reference signal at $\sim 13\text{MHz}$, phase locked to pump signal via frequency doubler and mixer (see Figure 7.5), is used for optical readout signal downconversion. After demodulation with the reference of the form $V_L \cos(\omega(t)t + \varphi_L)$, the expression for the downconverted signal assumes the form:

$$V_{DownConverted} = \xi_1 V_L V_2(t) sqw(t) \cos(\varphi_L), \quad (7.9)$$

where constant and higher-order terms are dropped and preamplifier stage and other proportionality factors are summarized into ξ_i (i changes 1, 2, 3... from stage to stage).

The relative phase φ_L was set to 0° to maximize the output via phase shifter. The time-domain measurement of this signal made by oscilloscope (Agilent 54622D) is shown in the inset of Figure 7.6. The downconverted signal is then detected by lock-in amplifier (SR830) externally referenced to the $V_{in}(t)$.

$$V_{Lock-In} = \xi_2 V_L V_2(t), \quad (7.10)$$

where $V_2(t)$ is a complex and periodic function (7.8), so we can express it in the sum of harmonics,

$$V_2(t) = V_{2constant} + \sum_{n=1}^{\infty} V_{2ncos} \cos(n\omega_{FM}t) + V_{2nsin} \sin(n\omega_{FM}t), \quad (7.11)$$

where the $V_{2constant}$ is the only contributing term in the detection scheme employed. It is equal to the average of the $V_2(t)$ over the frequency sweep period with a proper numerical coefficient.

$$V_{2constant} = \frac{2}{T_{FM}} \int_0^{T_{FM}} V_2(t) dt. \quad (7.12)$$

Therefore the output signal detected by lock-in amplifier is given by:

$$V_{output} = \xi_3 V_{2constant}, \quad (7.13)$$

which is proportional to the difference between top (red) and bottom (black) curves in the bifurcation diagram shown in figure 7.6.

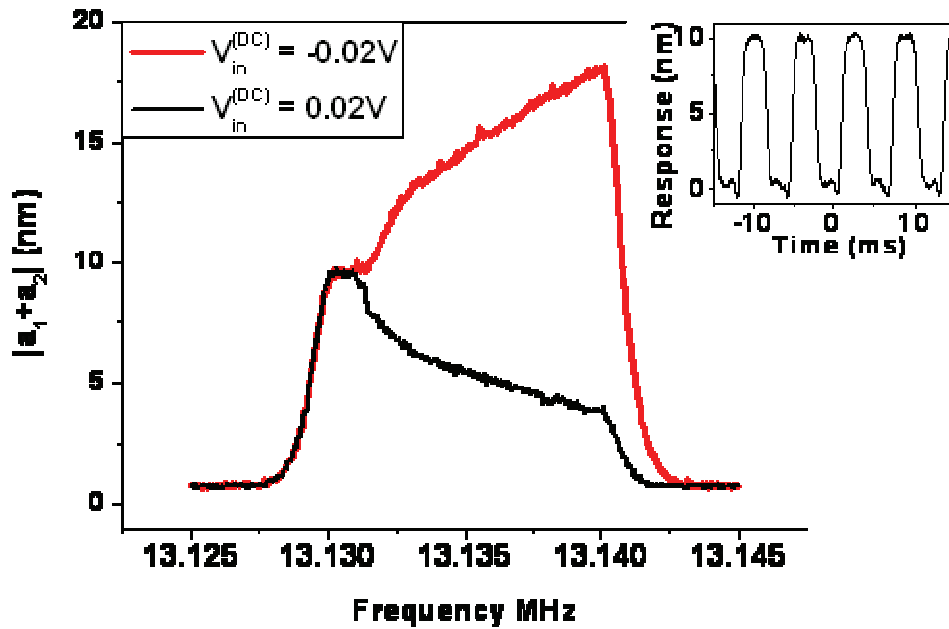


Figure 7.6 The output response as viewed on a spectrum analyzer. The frequency modulated RF pump gives rise to the red spectral response curve for a negative input signal and to the black spectral response curve for a positive input signal. The inset shows an oscilloscope trace of the demodulated output signal for a square-wave input signal $V_{in}(t)$. A lock-in amplifier is used to detect a signal proportional to the difference between the large-amplitude (red) and the small-amplitude (black) spectral response curves.

The total amplitude of the output signal, expressed in nanometres, is the displacement difference between the two spectral curves, averaged over the frequency sweep range.

7.4 BIFURCATION TOPOLOGY AMPLIFIER CHARACTERIZATION

We have performed measurements to characterize our BTA using a sweep rate of 557Hz and an input signal in the form of a sinusoidal or a square wave of frequency 167 Hz, with amplitude $V_{in}^{(AC)}$, offset from zero by $V_{in}^{(DC)}$. Figure 7.7(a) shows the measured response – corresponding to

the maximum-to-minimum difference of the output signal – as a function of $V_{in}^{(DC)}$ for different values of the amplitude $V_{in}^{(AC)}$. Until the input signal crosses zero the BTA does not sense any variation in it. This gives rise to the widths at half-maximum of the observed peaks in figure 7.7(a), while the sharpness of the rise and fall of the curves depends on the noise amplitude. The maximum heights of the peaks (at $V_{in}^{(DC)}=0$) depend on the signal amplitude $V_{in}^{(AC)}$. For input amplitudes that exceed the noise ($V_{in}^{(AC)} > 20$ mV) the maximum peak heights reach saturation and no longer increase because the BTA reliably switches between the two branches in every period of the input signal. For smaller input amplitudes, due to noise, the average output signal is proportional to the probability of the BTA to follow particular solution. Figure 7.7(b) shows the peak response at $V_{in}^{(DC)}=0$ a function of $V_{in}^{(AC)}$ for different values of artificially-added noise. Increasing the noise allows us to delay the saturation of the response beyond the original 20 mV and obtain a threefold increase in the operating range of the BTA, while trading in gain due to the constant saturation value. Note that for moderate noise levels the response of the BTA is linear. A more detailed study of the noise sources in the BTA will be necessary to explain the precise dependence of the response on the signal amplitude for strong levels of noise.

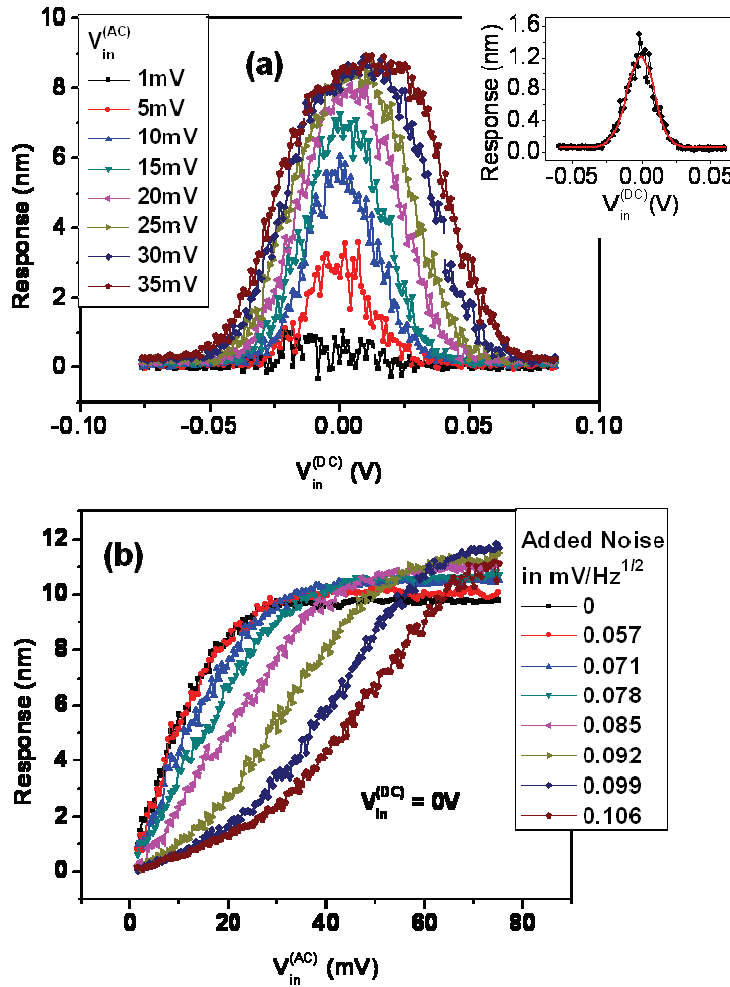


Figure 7.7 Measurements of the BTA, (a), for different values of the signal amplitude $V_{in}^{(AC)}$, as a function of its offset $V_{in}^{(DC)}$ from zero. The inset shows the smallest measured signal, with $V_{in}^{(AC)}=1$ mV, corresponding to about 70 fundamental charges in each resonator's conducting layer. (b) Same as (a), but as a function of the amplitude $V_{in}^{(AC)}$ with zero offset for different levels of added noise demonstrating a threefold increase in dynamic range.

The inset of Figure 7.7(a) shows the smallest input signal we have measured, $V_{in}^{(AC)}=1$ mV, corresponding to about 70 fundamental electron charges in each resonator's conducting layer, with each point averaged for about 23 s. After performing gaussian fit we determine that the magnitude

of a signal is 1.22 nm, thus displacement to charge responsivity of presented bifurcation topology amplifier is 17 pm/e. Intrinsic noise measurement with no input signal yield the displacement noise of 11.7 pm which corresponds to electronic charge noise of 0.68 electrons. The equivalent noise bandwidth in this measurement is 0.056 Hz, therefore the demonstrated charge sensitivity is 2.9 e/ $\sqrt{\text{Hz}}$. This makes our BTA one of the most sensitive mechanical room-temperature charge detectors demonstrated to date. In this implementation the noise in the system is not limited by thermally induced motion of the mechanical resonators, rather the noise is introduced by electronic parametric actuation sources as well as by optical readout system. Further optimization of the actuation and detection schemes will result in thermomechanical noise limited measurements with corresponding displacement noise floor [22] of $S_x^{1/2} = \sqrt{\frac{4k_B T Q}{m \omega_0^3}} = 0.116$ pm/ $\sqrt{\text{Hz}}$. Consequently the corresponding ultimate charge sensitivity possible with bifurcation topology amplifier is 0.0069e/ $\sqrt{\text{Hz}}$ at room temperature.

The concept of BTA can potentially be realized in a variety of physical systems including low temperature superconducting resonators, thus the ultimate sensitivity can further be reduced by several more orders of magnitude. Considering already demonstrated microwave frequencies mechanical resonators [27] as well as recent progress in efficient cooling of mechanical systems [49], we predict the thermomechanical noise floor reduction by four orders of magnitude based on modest estimate of 300mK temperature and geometrical parameters of 1GHz resonator. Hence mechanical BTA electrometer will reach sensitivities of the order of $1.5 \cdot 10^{-6}$ e/ $\sqrt{\text{Hz}}$, comparable with single electron transistor based charge detectors [5].

Although the bandwidth of the demonstrated bifurcation topology amplifier is limited by ~ 1 kHz, one could increase this bandwidth by using resonators with higher resonance frequencies

and smaller quality factors, the latter requiring stronger piezoelectric frequency tuning to excite parametric oscillations. This should allow an increase of up to three orders of magnitude by optimizing previously demonstrated microwave NEMS resonators [27].

SUMMARY

This chapter describes very interesting phenomenon where extraordinary level of control of complex diagram of mechanical vibration state for two weakly coupled parametric resonators leads to a novel amplification mechanism. The input voltage perturbs the bifurcation diagram causing large changes in output mechanical signal. The scheme holds enormous advantage including low noise, high sensitivity and absence of internal dissipation. We believe that BTAs can be implemented in a wide variety of physical systems, such as laser cavities, superconducting resonators, and coupled Josephson junctions, and possibly also in chemical and biological oscillating systems, which may lead to novel devices and applications.

Chapter 8

NONDEGENERATE PARAMETRIC EFFECT

This chapter considers the case of parametric actuation of two strongly coupled resonators. The conversion from individual beams to vibrational modes in this case leads to off-diagonal parametric terms, which are responsible for an interesting phenomenon called nondegenerate parametric amplifier. This chapter carefully describes the theoretical model as well as the experimental system characterization and conclusions.

8.1 PARAMETRIC ACTUATION OF TWO STRONGLY COUPLED RESONATORS

In this experiment we consider two strongly coupled individually accessible D-NEMS nanoresonators shown in figure 6.1. Two doubly clamped beams shown in the figure share a mechanical ledge, which is partially etched down to an insulating layer so that both devices are independently accessible while still maintaining strong interaction. A similar system was investigated in chapter 6.

The coupled equation of motion has the form of equation (5.3) with an addition of parametric term and assumes the form:

$$M\ddot{\vec{x}} + \Gamma\dot{\vec{x}} + V\vec{x} + P\vec{x} = F. \quad (8.1)$$

The mechanism of parametric tuning was discussed earlier in chapter 4. The voltage applied between top and bottom electrodes tunes the resonance frequency of the resonator. For periodically changing voltages $V_{p1}\cos(\omega_p t)$ and $V_{p2}\cos(\omega_p t)$ applied to the first and second beams respectively, the parametric matrix P is given by:

$$P = \begin{pmatrix} H_1 V_{p1}(t) & 0 \\ 0 & H_2 V_{p2}(t) \end{pmatrix}, \quad (8.2)$$

where new parameters H_1 and H_2 are introduced: they are the effective tunabilities of the stiffness constant measured in units of (N/m)/V. Since these values are referred to the individual beams, we have $H_i V_{pi}/m = h_p$, where h_p is a parametric pump amplitude from equations (2.8) and (7.1).

In the coupled system, dediagonalization procedure similar to equation (5.8) has to be performed in order to obtain the correct parametric terms for the modes of vibration. As a result, in the mode basis the parametric matrix assumes the form:

$$P' = \begin{pmatrix} e^2 H_1 V_{p1} + (1 - e^2) H_2 V_{p2} & e\sqrt{1 - e^2} (H_2 V_{p2} - H_1 V_{p1}) \\ e\sqrt{1 - e^2} (H_2 V_{p2} - H_1 V_{p1}) & (1 - e^2) H_1 V_{p1} + e^2 H_2 V_{p2} \end{pmatrix}. \quad (8.3)$$

The diagonal terms here are responsible for the regular DC tuning effect as well as the degenerate parametric actuation and amplification of individual modes (at twice the resonance frequency). It is easy to observe that a DC voltage applied to the first beam ($V_{p1}=V$ and $V_{p2}=0$) tunes both modes although at different rates, as does the reverse ($V_{p1}=0$ and $V_{p2}=V$) configuration, because both diagonal terms include V_{p1} and V_{p2} . The ratio of the slopes is determined by the strength of the coupling. Hence the results obtained in section 6.2 predict DC tuning measurements. The experimental DC tunability measurements for the first device in Table 6.1 are shown in figure 8.1, using $V_{p1}=V$ and $V_{p2}=0$ for (a) and $V_{p1}=0$ and $V_{p2}=V$ for (b). The ratio of the two slopes in each plot should be the squared ratio of the eigenvector components which is $(0.854/0.52)^2=2.7$. The slopes in figure 8.1 are 19.5 versus 7.9 kHz/V for (a)(19.4 and 7.5 kHz/V for (b)) with the ratio of 2.83(2.59), which is an excellent agreement with the prediction, although the overall expected slope is about 20% lower than predicted from the individual beam measurements in chapter 4. The possible reasons are that the additional etching steps and the

ledges configuration damages the beams as well as alters boundary conditions for the piezoelectric tuning problem. Nevertheless the tunability is significant enough to provide parametric pumping above the threshold for instability.

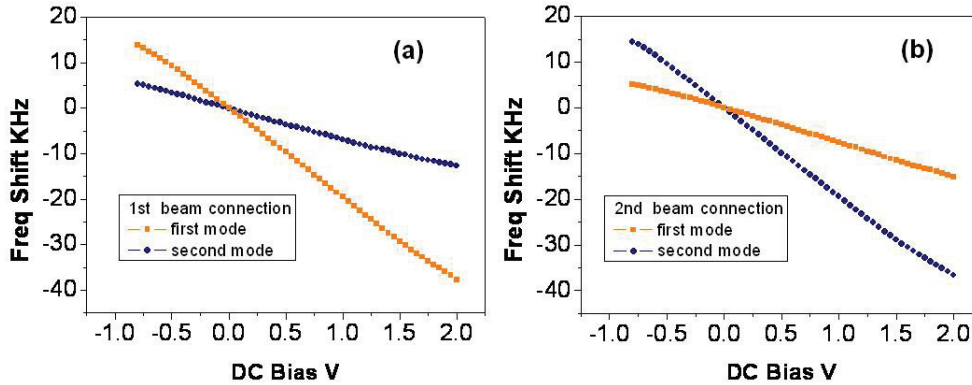


Figure 8.1 Dependence of the resonance frequency for the modes of strongly coupled resonators on the DC voltage applied to the individual beam's electrodes: (a) the first beam is biased, hence the first mode is tuned stronger than the second; (b) the second beam is biased, and therefore the situation is reversed.

The modified system of coupled Mathieu equations assumes the form:

$$\begin{aligned} \ddot{x}_I + \frac{\omega_I}{Q_I} \dot{x}_I + (\omega_I^2 + h_{p11} \cos(\omega_p t))x_I + h_{p12}x_{II} \cos(\omega_p t) + \alpha_I x_I^3 + \beta_I x_I x_{II}^2 &= 0, \\ \ddot{x}_{II} + \frac{\omega_{II}}{Q_{II}} \dot{x}_{II} + (\omega_{II}^2 + h_{p22} \cos(\omega_p t))x_{II} + h_{p21}x_I \cos(\omega_p t) + \alpha_{II} x_{II}^3 + \beta_{II} x_I^2 x_{II} &= 0. \end{aligned} \quad (8.4)$$

The Duffing coupling terms in this equation are based on calculation in section 6.1. The effects of the regular parametric terms h_{p11} and h_{p22} for two independent resonators were discussed in detail in earlier chapters. On the other hand new off-diagonal terms h_{p12} and h_{p21} lead to a very interesting novel physical phenomenon called nondegenerate parametric resonance. The theoretical analysis is performed using secular perturbation theory, similar to the method used in previous

chapters. We begin with rescaling the values similar to the procedure performed in equations (2.9) and (6.2). Interesting solutions caused by the off-diagonal terms occur when the pump frequency is near the sum of the resonance frequencies of the modes $\omega_p = \omega_I + \omega_{II} + \varepsilon \Omega_p$, while the motion of the modes is sought near their respective resonance frequencies

$$x_{[I]} = \frac{1}{2} \varepsilon^2 \left(A_{[I]}(T) e^{i\omega_I t} + c.c. \right) + \varepsilon^3 x_{[I]}^{(1)}(t) + \dots \quad [I] = I, II. \quad (8.5)$$

After the substitution the terms proportional to $O(\varepsilon^{1/2})$ cancel. Hence keeping $O(\varepsilon^{3/2})$ term we obtain the equation for the corrections $x_I^{(1)}$ and $x_{II}^{(1)}$.

$$\begin{aligned} \ddot{x}_I^{(1)} + \omega_I^2 x_I^{(1)} &= - \left[i\omega_I \frac{dA_I}{dT} + i\omega_I \Gamma_I A_I + D.N.T. + \frac{h_{12}}{4} A_{II}^* e^{i\Omega_p T} \right] e^{i\omega_I t} + \dots \\ \ddot{x}_{II}^{(1)} + \omega_{II}^2 x_{II}^{(1)} &= - \left[i\omega_{II} \frac{dA_{II}}{dT} + i\omega_{II} \Gamma_{II} A_{II} + D.N.T. - \frac{h_{21}}{4} A_I^* e^{i\Omega_p T} \right] e^{i\omega_{II} t} + \dots \end{aligned} \quad (8.6)$$

Here the abbreviation *D.N.T.* represents Duffing nonlinear terms similar to the ones in equations (6.7)-(6.9). The spontaneous parametric motion is then described by:

$$A_I = a_I e^{i(\Omega_p + \Omega)T/2}, \quad A_{II} = a_{II} e^{i(\Omega_p - \Omega)T/2}. \quad (8.7)$$

Here amplitude $a_{[I]}$ and detuning frequency Ω are determined by solving the system of algebraic equations analogous to (2.29):

$$\begin{aligned} \left\{ i \left[\omega_I \frac{\Omega_p + \Omega}{2} - \alpha_I |a_I|^2 - \beta_I |a_{II}|^2 \right] + \omega_I \Gamma_I \right\} a_I - i \frac{h_{12}}{4} a_{II}^* &= 0, \\ \left\{ i \left[\omega_{II} \frac{\Omega_p - \Omega}{2} - \alpha_{II} |a_{II}|^2 - \beta_{II} |a_I|^2 \right] + \omega_{II} \Gamma_{II} \right\} a_{II} + i \frac{h_{21}}{4} a_I^* &= 0. \end{aligned} \quad (8.8)$$

These equations are invariant under the transformation $a_I \rightarrow a_I e^{i\varphi}$, $a_{II} \rightarrow a_{II} e^{-i\varphi}$, so that only the sum of the phases $\varphi_I + \varphi_{II}$ is determined. Thus for 4 real unknowns there is a sufficient number of 4 real equations.

The threshold condition for nondegenerate parametric actuation is given by:

$$\left[i\omega_I \frac{\Omega_p + \Omega}{2} + \omega_I \Gamma_I \right] \left[-i\omega_{II} \frac{\Omega_p - \Omega}{2} + \omega_{II} \Gamma_{II} \right] = h_{12} h_{21}. \quad (8.9)$$

The imaginary part of this equation determines the detuning frequency Ω for the amplitudes near the onset of vibrations:

$$\Omega = \Omega_p \frac{\Gamma_I - \Gamma_{II}}{\Gamma_I + \Gamma_{II}}. \quad (8.10)$$

The real part of the equation then gives the tongue curve for the onset of spontaneous parametric oscillation:

$$h_{12} h_{21} = \omega_I \Gamma_I \omega_{II} \Gamma_{II} + \omega_I \omega_{II} \frac{\Omega_p^2 - \Omega^2}{4} = \omega_I \Gamma_I \omega_{II} \Gamma_{II} \left[1 + \frac{\Omega_p^2}{(\Gamma_I + \Gamma_{II})^2} \right], \quad (8.11)$$

which is very similar to the condition for individual parametric threshold derived in equation (2.32). In our experiment $h_{12}=h_{21}$, $\Gamma_I \approx \Gamma_{II}$ and $\omega_I \approx \omega_{II}$, and therefore at the lowest point of the tongue ($\Omega_p=0$) the off-diagonal term has to be at least $h_{12} \approx (\Gamma_I \omega_I \Gamma_{II} \omega_{II})^{1/2}$. For larger excitation levels the detuning frequency and the amplitudes of mechanical motion are determined by numerical solution of equation (8.8). The behavior of the amplitudes resembles the one for single parametric resonator in degenerate mode. The amplitude rises as approximately square root dependence on the sweep frequency [55].

8.2 NONDEGENERATE PARAMETRIC RESONANCE MEASUREMENTS

The existence of the solution to equations (8.8) and (8.9) implies that when a strongly coupled system of mechanical resonators is driven parametrically at frequency close to the sum of the resonance frequencies, the modes start vibrating simultaneously at their own resonance frequencies. This phenomenon is called nondegenerate parametric resonance. Previously

degenerate parametric pumping was performed at exactly twice the fundamental frequency of one mode, therefore the excitation phonon sent to the system was split into two identical ones with frequencies exactly one half of the initial frequency. In the nondegenerate case the excitation phonon is divided into two different unequal parts. This phenomenon is intensively studied and utilized in quantum optics for quantum state teleportation [56] and Bell inequality measurements [57]. In the mechanical domain this effect was observed for MEMS [58] and smaller NEMS [59] devices, although it was not studied in detail, and its origin was not explained to the extent done in this chapter.

Straightforward analysis of equation (8.11) combined with equation (8.3) yields an estimation of the threshold for both degenerate and nondegenerate parametric responses. The ratios of experimentally measured threshold values match predicted ones very well for all the three devices used in the measurements. Considering the original piezoelectric tunability measurements, the predicted and measured threshold voltages for the first device are given in table 8.1. The first device is chosen because the largest number of parametric resonances is visible. The second one has too strong coupling while the third has too weak coupling for many resonances to be visible.

Connection	Theoretical, mV_{rms}			Experimental, mV_{rms}		
	I	II	Nondeg	I	II	Nondeg
Left	193	557	339	219	NA	380
Right	519	206	339	537	235	345
180°	306	328	163	345	350	169
0°	140	151	∞	147	156	NA

Table 8.1 Theoretically predicted and experimentally measured threshold voltages for the first device for different connection configurations. NA (not available) means that the parametric resonance is not visible up to $700mV_{rms}$.

Different connection configurations in the table imply that the system is parametrically pumped either from left ($V_{p1}=V, V_{p2} = 0$), right ($V_{p1}=0, V_{p2} = V$), through 180° splitter ($V_{p1}=V, V_{p2} = -V$), or through 0° splitter ($V_{p1}=V, V_{p2} = V$). Most of the nondegenerate parametric resonator characterization measurements are performed with 180° splitter configuration, since the lowest threshold is achieved with this arrangement.

The simultaneous motion of two modes is detected by spectral analysis of the output of the photodetector. Figure 8.2 shows the result of the measurement. Two sharp peaks indicate sinusoidal mechanical motion of the beams. When a single resonator is actuated parametrically in degenerate mode as in chapters 4 or 7, the width of the peak is determined by the frequency linewidth of the RF source used for parametric drive, because the frequency of the mechanical response is constrained to be exactly one-half of the source frequency. As a result in those cases the peaks widths were limited by the spectrum analyzer resolution bandwidth, because the smallest RBW available for the instrument (Agilent 4395A) is 1Hz while most of the measurements were performed at RBW of 10-100Hz. The RF sources (Agilent 33250A and HP8648B) used in the experiments have a linewidth much narrower than that. Hence in all the previous experiments with degenerate parametric actuation, the measured spectrum had one sharp peak consisted of only one data point.

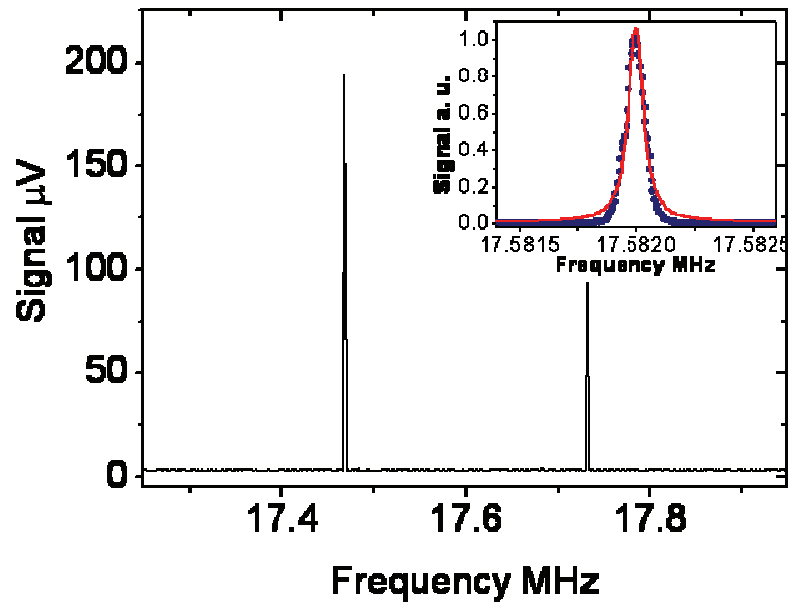


Figure 8.2 Spectrum analyzer measurement of the simultaneous motion of the two coupled modes. The inset shows the spectrum analyzer measurement of the width of the nondegenerate parametric peak.

This is no longer the case for nondegenerate parametric actuation. Earlier in this chapter it was shown that only the sum of frequencies of the mechanical motion of the two modes is constrained to equate to pump frequency. Therefore the individual frequencies are determined by mechanical properties of the system and are free to wander around, much like oscillators with a positive feedback loop. Treating nondegenerate parametric resonator motion as an independent oscillator we perform a measurement of its linewidth, which is plotted in the inset of Figure 8.2. The peak has a shape close to Lorentzian, the fit is shown as a red line in the plot. This suggests that white noise is responsible for widening the spectral response. The measured full width at half maximum is 79Hz, which corresponds to a factor of 140 linewidth reduction [60] assuming resonance frequency and quality factor of 17.4MHz and 1560 respectively (device #3 from Table 6.1).

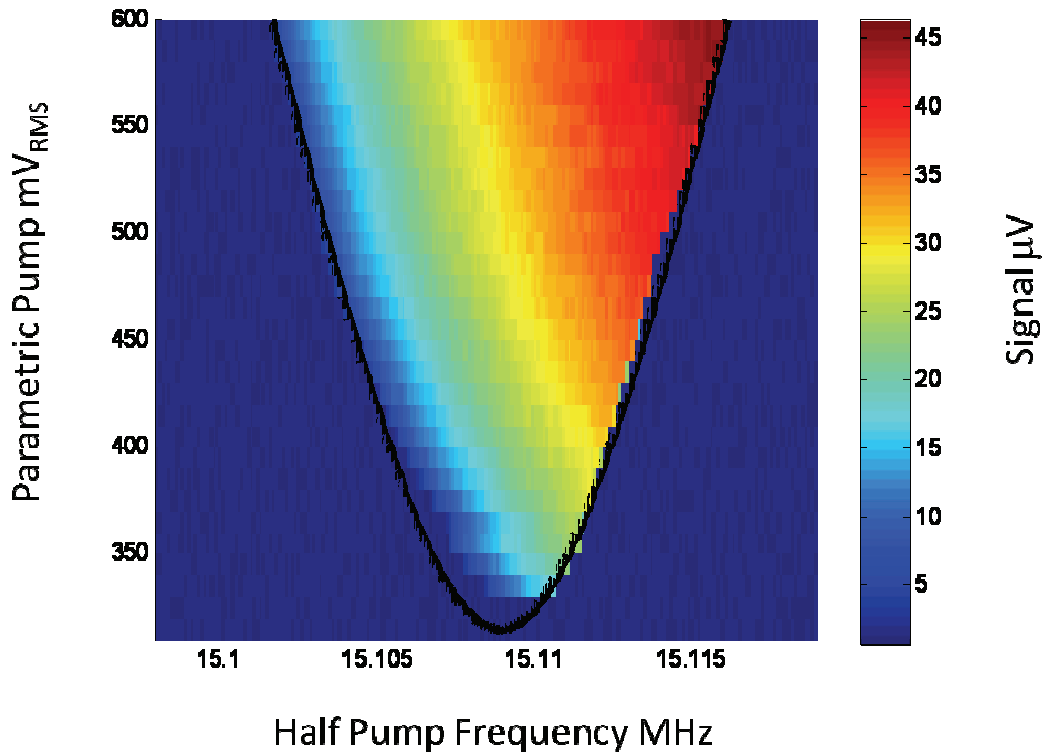


Figure 8.3 Measurement of the tongue boundary performed by repeated downward parametric sweeps. Color scale represents the amplitude of mechanical vibration of the first (left) peak, and half the pump frequency is chosen as the x-axis. The measurement well agrees with the theoretical prediction, shown as a black line (equation (8.11) for the parameters of device #3).

Spectrum analyzer measurements are used to characterize the nondegenerate parametric resonators. The expression (8.11) is verified by repeated downward frequency sweep measurements where only the first peak is monitored at different parametric drives. The result, for the second stronger coupled device from Table 6.1, is shown in figure 8.3. Black parabolic line represents theoretically calculated tongue boundary, derived from expression (8.11).

8.3 HARMONICS IN NONDEGENERATE PARAMETRIC RESONANCE

Going back to equation (8.6), a few more terms have to be taken into account in order to fully explain the experimental measurements. Assuming (8.8) is satisfied, so that the expression inside square brackets vanishes, we rewrite equation (8.6) taking (8.7) into account and including higher order terms that appear after the ellipses:

$$\begin{aligned}\ddot{x}_I^{(1)} + \omega_I^2 x_I^{(1)} &= -\frac{\beta_I}{2} a_{II}^2 a_I^* e^{i(2\omega_{II}-\omega_I+\varepsilon(\Omega_p-3\Omega)/2)t} - \frac{h_{11}}{4} a_I^* e^{i(\omega_{II}+\varepsilon(\Omega_p-\Omega)/2)t} + c.c., \\ \ddot{x}_{II}^{(1)} + \omega_{II}^2 x_{II}^{(1)} &= -\frac{\beta_{II}}{2} a_I^2 a_{II}^* e^{i(2\omega_I-\omega_{II}+\varepsilon(\Omega_p+3\Omega)/2)t} - \frac{h_{22}}{4} a_{II}^* e^{i(\omega_I+\varepsilon(\Omega_p+\Omega)/2)t} + c.c.\end{aligned}\quad (8.12)$$

On the left-hand side there is an expression for dissipationless simple harmonic resonator while on the right-hand side there are two terms, which are both representing off-resonance drive. The analytical solution to these equations assumes the form:

$$\begin{aligned}x_I^{(1)} &= \frac{\beta_I a_{II}^2 a_I^*}{8\omega_{II}(\omega_{II}-\omega_I)} e^{i(2\omega_{II}-\omega_I+\varepsilon(\Omega_p-3\Omega)/2)t} + \frac{h_{11}}{4(\omega_{II}^2-\omega_I^2)} a_I^* e^{i(\omega_{II}+\varepsilon(\Omega_p-\Omega)/2)t} + c.c., \\ x_{II}^{(1)} &= -\frac{\beta_{II} a_I^2 a_{II}^*}{8\omega_I(\omega_{II}-\omega_I)} e^{i(2\omega_I-\omega_{II}+\varepsilon(\Omega_p+3\Omega)/2)t} - \frac{h_{22}}{4(\omega_{II}^2-\omega_I^2)} a_{II}^* e^{i(\omega_I+\varepsilon(\Omega_p+\Omega)/2)t} + c.c.\end{aligned}\quad (8.13)$$

The second terms on the left- hand side of equation (8.13) insignificantly alter the amplitudes of the main peaks, because coefficients h_{11} and h_{22} are minimized due to the connection configuration employed. The first terms, on the other hand, imply that in addition to simultaneous motion of the two modes at their respective resonance frequencies, harmonics of these vibrations are generated at frequencies near $2\omega_{II}-\omega_I$ and $2\omega_I-\omega_{II}$. The harmonics are smaller in amplitude and are predicted to rise as the power of 3/2 with a sweep frequency, measured from threshold. Figure 8.4(a) shows the experimental evidence for harmonic generation using spectrum analyzer measurements described

earlier. Since the harmonics are slower to grow, the sweep has to be performed over a large frequency range for the peaks to rise above noise floor.

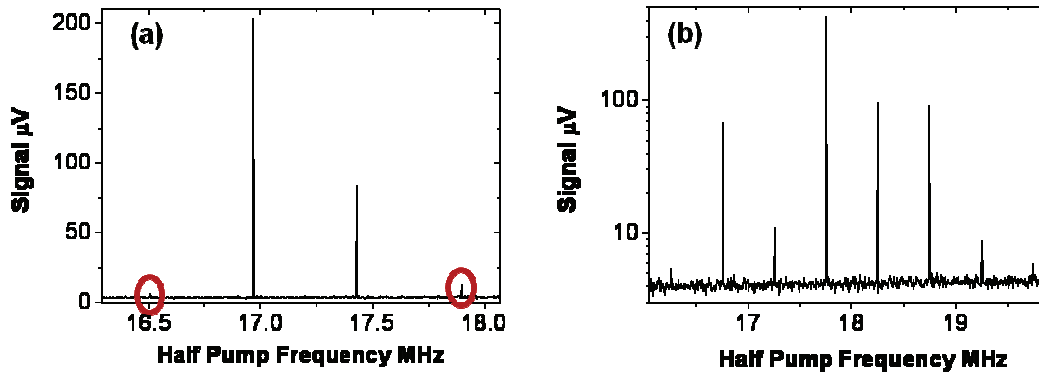


Figure 8.4 Experimental measurements of the harmonics generated due to the presence of nonlinear coupling terms: (a) evidence of the first pair of harmonics; (b) up to 3 pairs of harmonics were observed in long sweeps.

Similar consideration can be continued further with the possibility of second and third order harmonics generated when higher order terms are taken into account. In the experiment, for sufficiently long sweeps, up to three pairs of harmonics were observed; the plot in figure 8.4(b) shows the spectral response of the system on a semilog scale do display the sharp peaks with significantly different magnitudes.

Several long frequency sweeps were performed while the vibration amplitudes of the main and harmonic peaks were monitored. Figure 8.5(a) shows an experimental measurement of a long nondegenerate parametric sweep where the main peak amplitudes are plotted versus half the pumping frequency. The dependence is close to the predicted square-root function observed earlier in chapters 4 and 7. Two more pairs of harmonic peaks along with the main vibration modes are plotted versus sweep frequency on a log-log scale in figure 8.5(b).

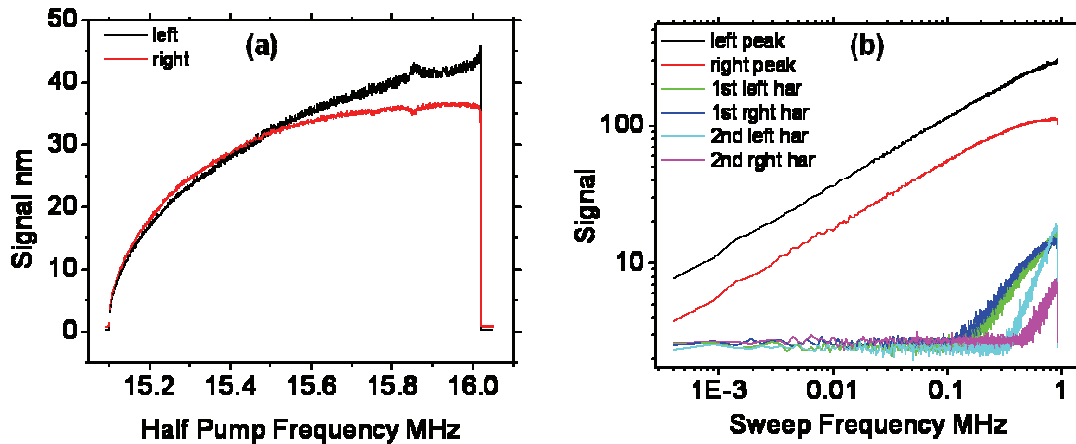


Figure 8.5(a) The dependence of the amplitudes of the two main peaks on a half pump frequency during long nondegenerate parametric sweep. (b) Log-log plot of main peaks and 2 more pairs of harmonics.

Power law fits to the curves on the second plot yield values close to the ones expected from theoretical analysis. The main peaks rise with a power 0.45, while the expected value is $\frac{1}{2}$; the first pair of harmonics grow with power of 1.3, while $\frac{3}{2}$ is expected; and the blue plot for second the second harmonic on the left increases with a power at 2.3, with $\frac{5}{2}$ being the expected value.

A few important observations have to be pointed out after analyzing the data. It is obvious from the second plot that that the power-law fit is only valid in a limited range close to the onset of vibrations: for the main-mode peaks the range is up to about 15.5 MHz. After this frequency the growth of the amplitudes slows down. This phenomenon may be caused by the increasing dissipation rate when generated harmonics grow significantly large. Frequency offset measurements described in the next section suggest a similar explanation. Another observation is that the amplitudes of the two peaks within one harmonic pair do not necessarily behave similarly. In the above example it is obvious from the second pair of harmonics. Other parametric sweeps

show behaviors that significantly deviate from the predicted ones. This effect may be caused by a variety of different mechanisms, such as quasi static asymmetric changes in mode shapes, or dissipation rates. Additional work has to be performed in order to fully understand the nature of the behavior of the harmonic amplitudes.

Even though theoretical analysis of the nonlinear mechanical motion predicts the generation of harmonics, there are intrinsic nonlinearities in the readout procedure that are also responsible for the production of harmonic peaks in the spectral response. In particular the conversion from mechanical displacement to optical intensity becomes nonlinear for large displacements [37]. The measurements for the uncoupled device used in the previous chapter, when driven both directly and parametrically, showed that the satellite harmonic peaks are indeed generated, but their magnitude never goes above $4 \mu\text{V}$, even for a displacement signal as high as $500 \mu\text{V}$. In the nondegenerate parametric case, the magnitudes of the harmonic peaks can grow as high as the height of one of the modes (Figure 8.4(b)), up to $100 \mu\text{V}$. No external nonlinearity can account for this. Therefore the observed harmonic peaks are due to the mechanical motion of the beams, perhaps slightly altered by external readout nonlinearities.

8.4 FREQUENCY SHIFTS AND SATELLITES

Another interesting observation is the small peak shaped structures in the amplitude dependence plot around 15.85MHz . This phenomenon has to be considered along with a study of the relative frequency shift between the two modes.

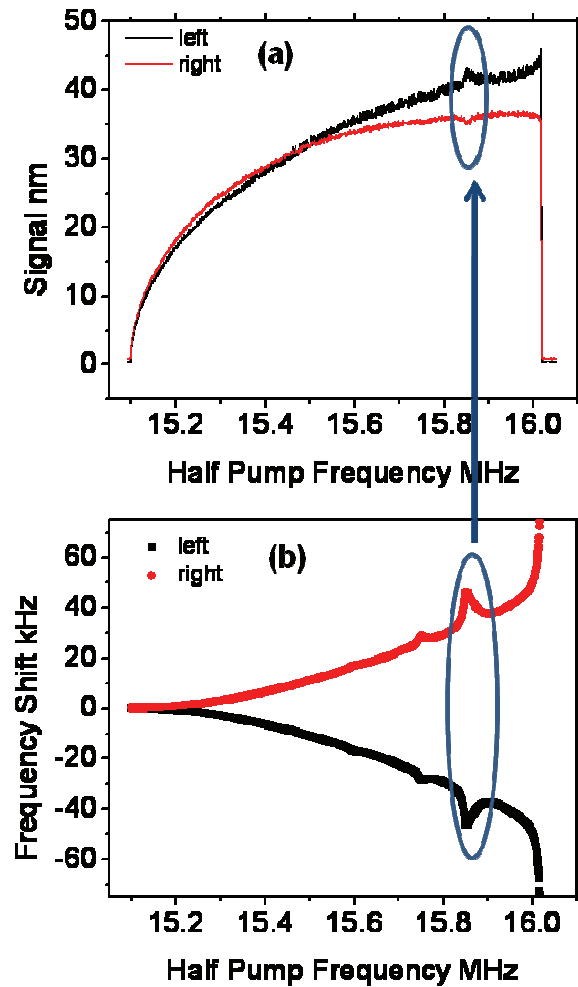


Figure 8.6 (a) Amplitude dependence during parametric frequency sweeps similar to figure 8.5(a); and (b) the relative frequency offset. Note that the small deviations in the amplitudes correspond to large deviations in the frequencies.

Figure 8.6(b) shows the plot of the change in relative frequency shifts of the modes. The value plotted is the frequency detuning Ω for left peak (black) and $-\Omega$ for right peak (red) from equations (8.7)-(8.11), converted to Hertz. It is a change in the offset of between frequency of the vibration and half pumping frequency relative to its initial offset at the onset of vibrations (the value is zero at the beginning of the scan near 15.1 MHz). The frequency shifts are equal in absolute magnitude

and opposite in sign, which is consistent with the theoretical expectations: Ω for the left peak and $-\Omega$ for the right peak. The previous amplitude dependence plot is shown in figure 8.6(a) with the same x-axis scale for comparison.

The experimental measurement shows that small peak shaped deviations in amplitude dependence plots correspond to large deviations in the frequency shift behavior. Equation (8.10) suggests possible explanations of the observed phenomenon. It implies that asymmetry in dissipation rate gives rise to offset in frequency shifts. Even though additional terms proportional to amplitudes will appear in this equation as the vibration grows, those terms are also proportional to asymmetries in the physical characteristics of the modes. Therefore we conclude that around 15.8 MHz in the long parametric frequency sweep the quality factor of the first mode increases relative to that one of the second mode. According to equation (8.10), this deviation causes the frequency of the left peak to drop, and the frequency of the right peak to increase. This observation is consistent with a sign of change in the growth of the amplitudes of the modes, with the height of the first mode peak increasing while the second one decreasing.

This suggests an explanation for the outcome, but not for the origin of the underlying physical phenomenon. Moreover, careful analysis of the plot in figure 8.6(b) reveals a few more peak shaped structures occurring during the sweep, although unnoticed in the amplitude dependence plot. Similar measurements are performed with the other two samples (#1 and #3) from Table 6.1. The results are shown in figure 8.7. The first device shows multiple peaks even with different signs. On the other hand the third device which has only minor coupling strength does not have peak shaped structures at all, and moreover the behavior of the relative frequency shift is different from the other two devices.

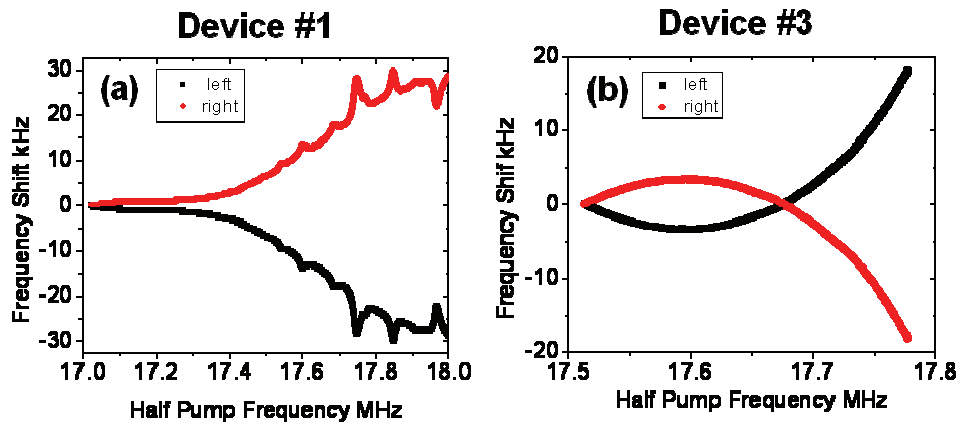


Figure 8.7 Relative frequency shift plots performed for other devices (#1(a) and #3(b)) in Table 6.1. Multiple peak-shaped structures are consistently observed in parametric sweeps of strongly coupled systems. The frequencies behavior of weaker-coupled device is smooth and changes sign during the sweep.

Careful measurement of the spectral composition of the mechanical motion around the region of the peaks yields a hint on the nature of the physical phenomenon for only the largest peak in figure 8.7(a) around 17.75 MHz. Figure 8.8(b) shows the corresponding spectrum analyzer plot on a semilog scale, while the relative frequency shift dependence for the second device is included in figure 8.8(a). The spectral response reveals that besides the higher order harmonics peaks, small, closer spaced satellite peaks appear near all the large peaks. Furthermore, a closer look at the largest peak shows even smaller satellites, evenly spaced with the first ones. Frequency measurement of the separation between the carrier and its satellites yields a value of exactly a factor of six smaller than the original mode peak separation. The generation of these satellite peaks may perhaps be caused by excitation of another parametric resonance, or by the instability of the amplitude of the main mode due to the presence of strong coupling, similar to well understood phenomenon described in chapter 6 for interacting Duffing resonators.

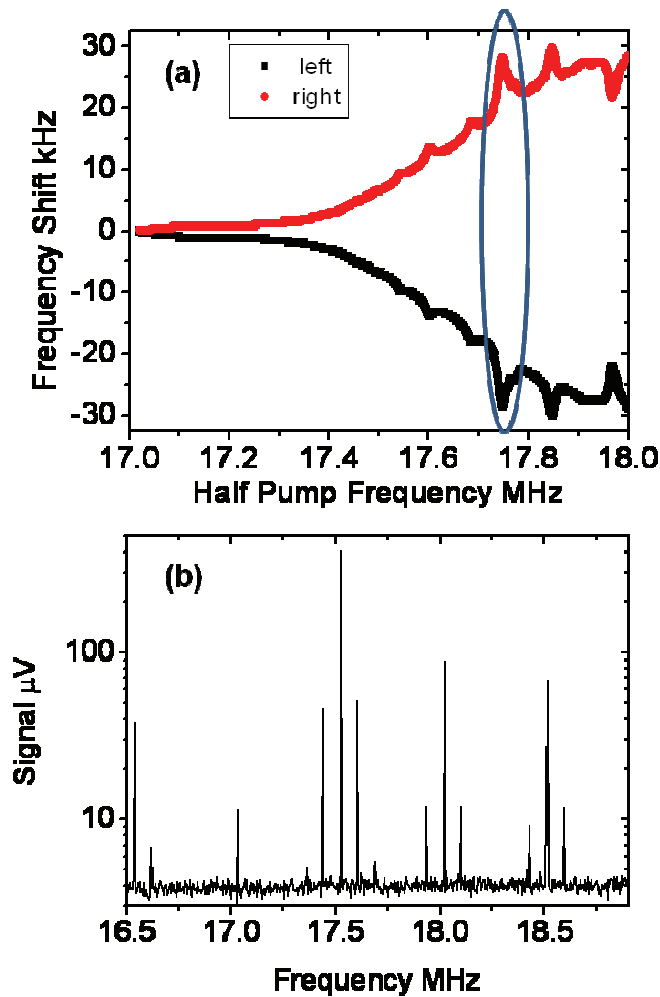


Figure 8.8 (a) Relative frequency shift behavior with multiple deviations, (b) spectrum analyzer plot showing satellite peaks.

The generation of satellite peaks opens another dissipative channel in the dynamics of the motion of an individual mode. When the resulting dissipation is asymmetric for the two different modes, a difference in damping rates develops. As a result, the steady frequency offset growth changes, and if this phenomenon is only present in a narrow frequency range during the sweep, a peak-shaped structure will occur. Therefore we suggest that similar satellite peaks generation may

take place in other cases, but their magnitudes are not sufficient to observe with the available experimental equipment.

Additional evidence to support the presented hypothesis is that in all the measurements the relative frequencies start to deviate at about the sweep frequency where the harmonic peaks start to appear. This may imply that the generation of harmonics itself is an asymmetric dissipative process, which causes a steady change in the relative frequency offset.

SUMMARY

This chapter provides a theoretical analysis and detailed experimental investigation of an interesting coupled parametric phenomenon, namely nondegenerate parametric resonance. Interesting phenomena such as harmonics and satellites peak generation were experimentally observed and partially understood theoretically.

This phenomenon is very promising for low-noise mechanical resonance sensing because it not only provides a fundamentally noiseless amplification mechanism but also it decouples pump and signal frequencies which is very important for rf background minimization [9].

Chapter 9

CONCLUSIONS AND FUTURE DIRECTIONS

In this chapter I will summarize the work done over the course of four years. And I will give my thoughts on future directions

8.1 FINAL THOUGHTS

The discussion about a future of the work performed here has to be done along with projections about the direction where all NEMS research is headed. The performance of nanoelectromechanical systems has already proved their potential for an amazing improvement in resonance frequency shift based sensing applications. Indeed extremely low mass, superb power efficiency and exceptional quality factor provide an excellent platform for realizing unsurpassed mass, charge, energy and force sensors. Albeit there is yet an appreciable gap between research games we play in the laboratory and reliable commercial applications, the chasm is closing at an incredible speed. This initial application is largely regarded as low-hanging fruit; in addition there is a vast field of imaginable appliances that are likely to be possible when the field of nanotechnology in general and NEMS in particular matures. Such novel nanoenabled applications include mechanical signal processing elements in integrated circuits, power switches for CMOS transistors, multifunctional wireless antitheft and RFID devices, fast and portable medical diagnostic equipment, efficient vibration power harvesters as well as small-scale mirror focusing actuators for solar panels. This list can be continued to embrace application that we cannot yet imagine.

Nonetheless in the meantime NEMS nanoresonators appear to be magnificent tools for fundamental research in multidisciplinary subjects ranging from quantum limited measurements [6,

49], to spintronics and magnetic domain study [61], to detailed study of nonlinear dynamics [23]. The research described here is valuable for both providing extra steps towards realizable real-world applications and expanding a platform for fundamental research.

The enormous advantages for employing parametric amplifiers in nanoelectromechanical systems, including intrinsically noiseless amplification and efficient compensation for dissipations, are extremely useful for promising commercial applications. On the other hand, a new type of dynamical system described by class of partial differential equations provides an opportunity to observe such interesting physical phenomena as multiple mechanical states and Hopf bifurcation.

Another important topic thoroughly investigated in this thesis is the behavior of the interacting systems of nanomechanical resonators. Detailed understanding of all the underlying physics is of paramount importance for reliable, practical NEMS-based gadgets, because it enables large-scale integration of the devices. At the same time, fundamental research benefits from this study because such interesting phenomena as voltage-dependent bifurcation topology and spontaneous state transitions originate during these investigations.

The most important point about future work is the one I learned from my advisor soon after joining the group: “No research project is ever complete.” One interpretation applicable here is that the systems we investigated holds an enormous potential for a number of research projects that can account for more than just another PhD thesis. What has been studied here is just a tip of the iceberg. There is plenty of room for improving the already invented tools to outperform analogs and old version, and most excitingly invent new ones.

BIBLIOGRAPHY

1. R. Feynman, Plenty of room at the bottom, (1959) available at <http://www.its.caltech.edu/~feynman/plenty.html> .
2. M. L. Roukes, *Phys. World* **14**, 25 (2001).
3. Y. T. Yang, C. Calegari, X. L. Feng, K. L. Ekinci, M. L. Roukes, *Nano Lett.* **6**, 583 (2006).
4. D. Rugar, R. Budakian, H. J. Mamin, B. W. Chui, *Nature* **430**, 329 (2004).
5. A. N. Cleland, M. L. Roukes, *Nature* **392**, 160 (1998).
6. M. D. LaHaye et al., *Science* **304**, 74-77 (2004).
7. X. L. Feng, R. B. Karabalin, J. S. Aldridge, M. L. Roukes, Pending US Patent **60/901,566**
8. L. Wu, H. J. Kimble, J. L. Hall, H. Wu, *Phys. Rev. Lett.* **57**, 20 (1986).
9. R. Movshovich, et. al., *Phys. Rev. Lett.* **65**, 1419-1422 (1990).
10. E. Esarey, P. Sprangle, J. Krall, A. Ting, *IEEE Trans. on Plasma Science* **24**, 252(1996)
11. D. Rugar, P. Grütter, *Phys. Rev. Lett.* **67**, 699 (1991).
12. K. L. Turner et al., *Nature* **396**, 149-152 (1998).
13. D. W. Carr et al., *Appl. Phys. Lett.* **77**, 1545-1547 (2000).
14. R. Lifshitz, M. Cross, *Phys. Rev. B* **67** (2003).
15. A. Dana, F. Ho, Y. Yamamoto, *Appl. Phys. Lett.* **72**, 1152 (1998).
16. M. Moreno-Moreno, A. Raman, J. Gomez-Herrero, R. Reifengerger *Appl. Phys. Lett.* **88**, 193108 (2006).
17. K. L. Ekinci, Y. T. Tang, M. L. Roukes, *Jour. of Appl. Phys.* **95**, 2682 (2004).
18. S. Timoshenko, D. H. Young, W. Weaver, *Vibration Problems in Engineering*, 4 ed., New York: Wiley (1974).
19. I. Kozinsky, PhD dissertation, Caltech (2007).
20. S. S. Verbridge, D. F. Shapiro, H. G. Craighead, J. M. Parpia, *Nano Lett.* **7** 1728 (2007).

21. A. H. Nayfeh, D. T. Mook, *Nonlinear Oscillations*, New York: Wiley (1979).
22. A. N. Cleland, M. L. Roukes, *Jour. of Appl. Phys.* **92**, 2758-2769 (2002).
23. Ron Lifshitz, M. C. Cross, Nonlinear Mechanics Review (to be published).
24. W. Zhang, R. Baskaran, K. L. Turner, *Sensors and Actuators A* **102**, 139-150 (2002).
25. D. A. Harrington, PhD dissertation, Caltech (2002).
26. R. B. Karabalin et al., in preparation.
27. X. M. H. Huang, C. Zorman, M. Mehregany, M. L. Roukes, *Nature* **421**, 496 (2003).
28. A. N. Cleland, M. L. Roukes, *Sensors and Actuators* **72**, 256-261 (1999).
29. E. T. Swartz, R. O. Pohl, *Rev. Mod. Phys.* **61**, 31 (1989).
30. O. W. Kading, H. Skurk, K. E. Goodson, *Appl. Phys. Lett.* **65**, 13 (1994).
31. N. W. Ashcroft, N. D. Mermin, *Solid State Physics*, Sanders College Publishing (1976).
32. V. F. Gantmakher, *Rep. Prog. Phys.* **37**, 317-362 (1974).
33. W. Fon, K. C. Schwab, J. M. Worlock, M. L. Roukes, *Phys Rev B* **66**, 045302 (2002).
34. X. L. Feng, C. A. Zorman, M. Mehregany, M. L. Roukes, *Hilton Head* (2006 in press).
35. P. Mohanty et al., *Phys. Rev. B*, **66**, 085416 (2002).
36. S. C. Masmanidis, et. al., *Science* **317**, 780 (2007).
37. Sotiris Masmanidis, PhD dissertation, Caltech (2006).
38. D. W. Carr, H. G. Craighead, *J. Vac. Sci. Technol.* **15**, 2760-2763 (1997).
39. M. Li, H. Tang, M. L. Roukes, *Nature Nanotechnology* **2**, 114-120 (2007).
40. The definition of commonly used term “Allan deviation” (or Allan variance) is available here http://en.wikipedia.org/wiki/Allan_variance .
41. A. N. Cleland, *New J. of Phys.* **7**, 235 (2005).
42. P. Curie, J. Curie, *Bulletin de la Société minéralogique de France*, 90-93 (1880).
43. H. Goldstein, *Classical Mechanics*, 2 ed., Addison-Wesley Publishing Company (1980).

44. I. Bargatin, I. Kozinsky, M. L. Roukes, *Appl. Phys. Lett.* **90**, 093116 (2007).
45. W. D. Bowers, R. L. Chuan, T. M. Duong, *Rev. Sci. Instrum.* **62**(6), 1624-1629 (1991).
46. V. B. Braginsky, F. Y. Khalili, *Quantum Measurement*, Cambridge University Press (1995).
47. D. H. Santamore, A. C. Doherty, M. C. Cross, *Phys. Rev. B* **70**, 144301 (2004).
48. X. M. H. Huang, PhD dissertation, Caltech (2003).
49. A. Naik et al, *Nature* **443** 193–196 (2006).
50. J. Kozlowski, U. Parlitz, W. Lauterborn, *Phys. Rev. E* **51**, 1861 (1995).
51. S. Paul Raj, S. Rajasekar, K. Murali, *Phys. Lett. A* **264**, 283-288 (1999).
52. T. Endo, Y. Aruga, K. Yamauchi, *Proceedings to ISCAS* **3**, III-96 – III-99 (2003).
53. I. Siddiqi et al., *Phys. Rev. Lett.* **93** 207002 (2004).
54. R. Almog, S. Zaitsev, O. Shtempluck, E. Buks, *Appl. Phys. Lett.* **88**, 213509 (2006).
55. E. Kenig and Ron Lifshitz, private correspondence.
56. S. L. Braunstein, H. J. Kimble, *Phys. Rev. Lett.* **80**, 4 869-872 (1998).
57. Z. Y. Ou, S. F. Pereira, H. J. Kimble, *Appl. Phys. B* **55**, 265-278 (1992).
58. R. Baskaran, K. Turner, *J. Micromech. Microeng.* **13**, 701-707 (2003).
59. A. Olkhovets, D. W. Carr, J. M. Parpia, H. G. Craighead, *Proceedings to IEEE Conference on MEMS* **14**, 298-300 (2001).
60. D. Ham, A. Hajimiri, *IEEE Journal of Solid-State Circuits* **38**, 3, 407-418 (2003).
61. H. Tang, S. C. Masmanidis, R. K. Kawakami, D. D. Awschalom, M. L. Roukes, *Nature* **431**, 52-56 (2004).